OPTIMIZATION OF SnS BASED HETEROJUNCTION TO IMPROVE ITS PHOTOVOLTAIC PERFORMANCE

Thesis submitted to the University of Calicut for the partial fulfillment of the requirements for the award of the degree of

Doctor of Philosophy

in Physics under the faculty of sciences

By

SMIYA JOHN

Under the guidance of

Dr. V. GEETHA

&

Co-guidance of

Dr. REENA MARY A. P.

Research and Post Graduate Department of Physics
Government Victoria College, Palakkad
Kerala

June - 2023

CERTIFICATE

This is to certify that the work presented in this thesis entitled **"OPTIMIZATION OF SnS BASED HETEROJUNCTION TO IMPROVE ITS PHOTOVOLTAIC PERFORMANCE"** is based on the authentic record of research carried out by Ms. Smiya John under my guidance in the Department of Physics, Government Victoria College, Palakkad. This work has not been included in any other thesis submitted previously for the award of any degree and has undergone plagiarism check using OURIGINAL (Urkund) Software at CHMK Library, University of Calicut.

Government Victoria College, Palakkad
20th June 2023

Dr. V. Geetha
Research Guide
Department of Physics
Government Victoria College
Palakkad.

CERTIFICATE

This is to certify that the work presented in this thesis entitled **"OPTIMIZATION OF SnS BASED HETEROJUNCTION TO IMPROVE ITS PHOTOVOLTAIC PERFORMANCE"** is based on the authentic record of research carried out by Ms. Smiya John under my co-guidance in the Department of Physics, Government Victoria College, Palakkad. This work has not been included in any other thesis submitted previously for the award of any degree.

Government Victoria College, Palakkad
20th June 2023

Dr. Reena Mary A. P.
Associate Professor
Department of Physics
Government Victoria College
Palakkad.

DECLARATION

I hereby declare that the work presented in this thesis entitled **"OPTIMIZATION OF SnS BASED HETEROJUNCTION TO IMPROVE ITS PHOTOVOLTAIC PERFORMANCE"** is based on the original research work done by me under the guidance of Dr. V. Geetha, Research guide, Department of Physics, Government Victoria College, Palakkad, Kerala and the co-guidance of Dr. Reena Mary A P, Associate Professor, Department of Physics, Government Victoria College, Palakkad, Kerala has not been included in any other thesis submitted previously for the award of any degree or diploma of the university or other institute of higher learning, except where due acknowledgment has been made in the text.

Government Victoria College, Palakkad
20th June 2023

Smiya John
Research Scholar
Department of Physics
Government Victoria College
Palakkad.

ACKNOWLEDGEMENTS

My Ph. D tenure was fascinating, challenging and extremely rewarding. I wish to thank all the people whose assistance were milestones in shaping the final form of my thesis.

To commence with, I pay my obeisance to GOD, the Almighty for paving me the right path, leading me to success and also for having bestowed upon me good health, courage, inspiration, zeal and the light.

I express my sincere and deepest gratitude to my supervisor, Dr. V Geetha (Research guide, Department of Physics, Government Victoria College, Palakkad) for making critical suggestions and posing challenging questions. Her expertise, affectionate attitude, valuable guidance, understanding, patience, constant encouragement, and healthy criticism added considerably to my experience. Without her continual inspiration, it would have not been possible to complete this study.

I owe special thanks to Dr. Reena Mary A. P. (Associate Professor, Govt. Victoria College, Palakkad) who was my co-guide, for the assistance provided throughout the tenure. I gratefully acknowledge Dr. Maya C Nair (Principal, Govt. Victoria College, Palakkad), and the former principals for their encouragement and support. I also thank Dr. Ambily Krishnan (Head of Physics Department, Govt. Victoria College) all the faculty members and the research group of Govt. Victoria College for providing necessary support in all the official matters and also for extending library facilities at the research centre. Special thanks to Dr. Pradeesh K, for the untiring help, timely support and selfless favours rendered during my Ph.D work.

Being a part time research scholar, the support from Mercy College, Palakkad needs a special mention. At the outset, I take this opportunity to express my deep sense of gratitude and respectful regards to Dr. Lakshmi M (Head of Physics Department, Mercy College, Palakkad) who gave me untiring help by extending liberal support, timely motivation and official work relaxations during the course of the entire study. I express my deep sense of gratitude and respectful regards to

Ms. Mariyama John (Rtd: Associate Professor and Head of Physics Department, Mercy College, Palakkad) who gave me diligent support by extending substantial support, timely inspiration and official work moderations during the course of the entire study.

I am highly thankful to my colleague and mentor Dr. Sr. Jessy Mathew N for the motivation, moral support and prayers throughout my career. I sincerely admire the contributions of my lab mates and colleagues Dr. Anlin Lazar K, Dr. Melda Francis and Dr. Anu Kuruvilla (Assistant Professors, Department of Physics, Mercy College, Palakkad) through their valuable suggestions, motivation, understanding and the untiring help which made me capable of facing all the challenges throughout the journey.

I am grateful to Dr. Sr. Jorry T F (Principal, Mercy College, Palakkad) and the former principals Dr. Sr. Gisala George, Dr. Sr. Lilly P V and Dr. Sr. Alice Thomas of Mercy College, Palakkad for their prayerful inspirations and support. I extend my gratitude to Government Victoria College, Palakkad and all the administrative staff for providing research lab facility and infrastructure for my entire work.

I gratefully acknowledge the financial assistance of UGC, MHRD, India through a minor project. My sincere thanks to DST - FIST for the financial support provided for procuring RF Sputtering System. I also acknowledge SAIF-STIC, CUSAT, IIT, Palakkad and St. Thomas College, Thrissur for the services rendered for various analysis techniques like XRD, SEM, EDS etc.

Last, but not least, I would like to dedicate this thesis to my family because their love, patience, and understanding gave me strength in the pursuit of my doctoral degree.

I owe my deepest gratitude towards my better half, Paul K Joseph for his eternal support and understanding of my goals and aspirations. His faithful motivation during each stage of my Ph. D is so appreciated. I thank my kids Maria Paul and Joseph John Paul for being patient during the busy final days of my research work without giving any trouble in my PhD journey.

I would like to thank my parents, P. K John and Teresa Joseph, from the bottom of my heart for all their love and encouragement. Their patience and sacrifice will remain my inspiration throughout my life. I am also grateful to my younger sister, Snigdha John, for her constant love, motivation, criticism and affection. I feel a deep sense of gratitude for my father-in-law (Joseph V L), mother-in-law (Mary K P) and all my siblings-in-law who has always been my strength. I am also very much grateful to all my family members and friends for their constant inspiration, prayers and encouragement.

As always, it is impossible to mention everybody who had an impact in this whole process. Therefore, I extend my token of love and gratitude to all those who played their own roles in the completion of my work.

20th June 2023 *Smiya John*

Dedicated to

My Loving Family.....

CONTENTS

PREFACE

Recent developments in energy generation highlights the role of thin film solar cells as effective technology to provide clean, renewable and cost-effective energy. Thin film solar cells made from earth-abundant, non-toxic materials with adequate physical properties such as band-gap energy, large absorption coefficient and p-type conductivity are needed in order to replace the current technology based on scarce, expensive and toxic elements. Here we have chosen tin sulphide as it has high theoretical photoelectron conversion efficiency (>20%), less toxicity, good chemical stability and its constituent elements are abundant in earth's crust. However, SnS-based solar cells' claimed power conversion efficiency (η) remained below 4%. Making high-quality SnS thin films and choosing the right n-type semiconductor are two possible obstacles for enhancing the efficiency of SnS based solar cells. This was tried in this work.

The creation of photon management techniques to maximize light absorption for applications like solar cells, photo electrochemistry, and sensing has received a lot of attention in recent years. Photonic crystals, which are considered the optical analogue of crystals, are capable of controlling the flow of light. In this work, 1D photonic crystals were simulated using MEEP software, which is free and open software. The effect of dielectric contrast and the number of layers on the photonic band gap was investigated. ZnO/SiO_2 1D photonic crystals were fabricated by sputtering. The experimental results matched the simulations. It is always better to have simulation as a pre-laboratory, as it saves time and money.

Organization of the thesis

This thesis reports on possibility of modification of the properties and photovoltaic performance of chemically prepared SnS thin film by changing the pH of the bath solution and annealing temperature. A further enhancement of efficiency was obtained using the SiO_2/ZnO 1D Photonic crystals for light trapping. Simulation work was done as the pre laboratory.

A basic introduction to thin films and tin chalcogenides is provided in Chapter 1. Tin sulphides are a group of IV-VI semiconductors that come in SnS, SnS_2, and Sn_2S_3 as their three major forms. The tin sulphides SnS, SnS_2, and Sn_2S_3 have bulk band gaps of 1.4 eV, 2.3 eV, and 1.1 eV, respectively. All tin sulphide forms are semiconducting, but as previously stated, SnS has garnered the most attention due to its direct electronic band gap of 1.4 eV, which is comparable to the current industry standard conventional semiconductors gallium arsenide and silicon. The conversion efficiency of a solar cell is determined by various parameters and they are discussed. Various light trapping techniques were discussed.

Chapter 2 provides an overview of the primary thin film deposition and characterization methods employed in this research. Here Chemical bath deposition method and magnetron sputtering methods were utilized for the thin film production. RF magnetron sputtering is used here to deposit 1D photonic crystals. By characterizing the films using a range of investigative approaches, the growth mechanism and characteristics of the films can be explored in great detail. This section includes concise description of the techniques that have used to characterize the thin films. X-ray diffraction, Raman spectroscopy, a field emission scanning electron microscope (FESEM), Energy dispersive X ray spectroscopy, UV- visible spectroscopy and Keithley source meter to conduct structural, morphological, compositional, optical and I-V studies.

SnS and CdS thin films were synthesized chemically for different pH values of bath solutions. The optimal pH values for SnS film formation were 9.8, 9.9, and 10, while the pH values for CdS were 11.3, 11.4, and 11.5. Film formation did not take place outside this pH range at ambient conditions. The structural, morphological, optical, and chemical characterization revealed changes in the thin film properties with the pH variation. Structural analysis showed an increase in crystallite size for SnS and CdS as the pH of the solution increased. The optical band gap was found to decrease as the pH of the solution increased for both materials. Morphological studies showed that the film became more continuous and uniform as the pH of the bath solution increased. The atomic weight of metal increased as the pH increased, according to the EDS spectra of both films. Photovoltaic cells were fabricated with an ITO/CdS/SnS/Ag configuration, where the SnS thin film deposited at pH 10 and the CdS film deposited at pH 11.3 showed better performance. It was observed that the pH of the bath solution has an effect on the efficiency of the photovoltaic cell. Even

though, the cell performance of the fabricated heterojunction was poor, the successful formation of the p-n junction was confirmed. However, SnS thin films are potential candidates for solar cells, and trials can be made to improve the solar cell's performance by optimizing the cell configuration.

In Chapter 4 the effect of annealing on the properties of SnS thin films were investigated. The chemically created SnS thin films were subjected to various annealing temperatures. The ideal annealing temperature for SnS was determined to be 200°C. No peaks were visible in the films annealed at 250°C XRD or Raman spectra. The structural, morphological, optical, and chemical characterization demonstrated that variations in the annealing temperature led to modifications in the thin film properties. The films crystallite size grew as the annealing temperature rose, according to structural analyses. It was discovered that when the annealing solution's temperature rose, the optical band gap shrank. With annealing, morphological tests revealed that the film became denser and the needle-shaped morphology changed to a plate-shaped one, increasing the grain size. The atomic weight percentage of sulphur dropped as the annealing temperature rose, according to EDS spectra. ITO/SnS/CdS/Ag configuration were employed in the construction of photovoltaic cells, and a thin SnS film that had been annealed at 200°C served as the absorber layer. The efficiency of the solar cell was found to be impacted by the annealing of the film. An increase in efficiency was seen by annealing the SnS thin film. This technique is an inexpensive way to produce SnS thin films for the absorber layer of solar cells.

Modern advanced electronic, optoelectronic, and photonic devices are in demand for multilayer thin film structures, which are also considered as 1D photonic crystals (PC). It is preferable to optimize the PC's design on the computer before building it. They are favorable for computation because the length scales are not too small, and the Maxwell equations that govern the propagation of electromagnetic radiation through the PC are practically exact. The programs called MIT electromagnetic equation propagation (MEEP) were used for computing transmission spectra. This simulation is detailed in Chapter 5. Meep implements the finite-difference time-domain (FDTD) method. The 1D photonic crystals with different layers were simulated, and the transmission spectra were plotted using MEEP software. The effect of the dielectric contrast on the width and position of the photonic bandgap was investigated using the simulated transmission spectra. Transmission spectra with different

numbers of layers were plotted, and it was found that eleven layers are enough for creating a stop band.

Reactive sputtering has been thought of as a useful technique to deposit high-quality dielectric films of ZnO and SiO_2 and this is discussed in chapter 6. Despite its low deposition rate, the sputtering process is simple to control, and the deposited layers exhibit good adhesion and coating uniformity. The ZnO and SiO_2 films with acceptable optical and structural properties were coated using the RF magnetron sputtering technique. After the simulation work, ZnO/ SiO_2 PC with 11 layers was fabricated, and the transmission spectra was investigated. The results were comparable with the simulations.

Chapter 7 briefs the summary of the work done so far and details about the work expected to be performed in future. Further improvement of the efficiency is required to make the fabricated cell to put into the industry. The efficiency can be improved by decreasing the resistance of the layers. For that doping the layers with metals especially silver can be tried. Also, different possible applications of SnS thin films can be exploited such as photosensors. Over the past decade, a tremendous development has taken place within the area of optical components having a full or partly periodic structure incorporated. A small amount of disorder will not destroy the PBG but will allow localized modes to exist within the gap, which can be utilised for wave guiding. Such PC can be utilized as anti-reflective coatings that guide the solar radiation into the junction without any loss. This disorder can be incorporated either by changing the thickness or dielectric contrast of a single layer. Two-dimensional photonic crystals called photonic-crystal fibers are used for fiber-optic communication, among other applications. Three-dimensional crystals may one day be used in optical computers, and could lead to more efficient photovoltaic cells. This new class of optical waveguides is characterized by a carefully engineered cross-section of glass (or polymer) riddled with a pattern of miniature holes. The future work and recommendations provide work plan to support and sustain the research work with a sole aim to develop innovative and potentially efficient SnS based devices along with the fabrication of photonic crystals for light harvesting and optical communication application.

LIST OF FIGURES

LIST OF TABLES

LIST OF ABBREVIATIONS

CBD	-	Chemical Bath Deposition
CVD	-	Chemical Vapor deposition
SILAR	-	Successive Ionic Layer Adsorption and Reaction
PC	-	Photonic Crystals
PBG	-	Photonic Band Gap
MEEP	-	MIT Electromagnetic Equation Propagation
EDS/EDX/EDAX	-	Energy Dispersive X-Ray Spectroscopy
FF	-	Fill Factor
FWHM	-	Full Width at Half Maximum
ITO	-	Indium doped Tin Oxide
PVD	-	Physical Vapor Deposition
RF	-	Radio Frequency
SCCM	-	Standard Cubic Centimeters per Minute
FESEM	-	Field Emission Scanning Electron Microscopy
SEM		Scanning Electron Microscopy
SMU		Source Measuring Unit
UV-Vis NIR	-	Ultra Violet - Visible Near Infra-Red
W-H Plot	-	Williamson-Hall Plot
XRD	-	X-Ray Diffraction

LIST OF SYMBOLS

λ	-	Wavelength
β	-	Full Width at Half Maximum
d	-	Inter atomic distance
D	-	Crystallite size
α	-	Absorption coefficient
A	-	Absorbance
T	-	Transmittance
h	-	Plank's Constant
ν	-	Frequency
ω	-	Angular frequency
η	-	Power Conversion Efficiency
J_{sc}	-	Short circuit current density
V_{oc}	-	Open circuit voltage
ε	-	lattice strain

LIST OF PUBLICATIONS

Journal Publications

1. **Smiya John**, Melda Francis, Reena Mary A P and V Geetha "Influence of annealing on the properties of chemically prepared SnS thin films" *Chalcogenide letters* 20, May 2023, 315
2. **Smiya John**, Melda Francis, Reena Mary A P and V Geetha "Influence of pH on the properties of chemically prepared SnS and CdS thin films'' *Indian journal of pure and applied physics* 61, May 2023, 326
3. **Smiya John**, Anlin Lazar K, Reena Mary A P and V Geetha "Simulation and fabrication of ZnO/SiO2 based 1D Photonic crystals for light trapping application", *Journal of optics*, June 2023 DOI: 10.1007/s12596-023-01297-5
4. **Smiya John**, Melda Francis, V Geetha "Effect of pH on the optical and structural properties of SnS prepared by Chemical Bath Deposition method", *IOP Conference Series Materials Science and Engineering* 872, June 2020 012139
5. **Smiya John**, and V Geetha "Effect of deposition parameters on the properties of PbS/CdS thin film prepared using SILAR method" *AIP Conference Proceedings* 2162, October 2019, 020138
6. **Smiya John,** Reena Mary A P and V Geetha "Modelling the Tuning of Photonic Band Gap of 1 D Periodic Dielectric Structure using Frequency Domain" (provisionally accepted : AIP proceedings (ICAPSM 2022)

Paper/Poster presentation

1. "Modelling the Tuning of Photonic Band Gap of 1 D Periodic Dielectric Structure using Frequency Domain" in Third International Conference on Advances in Physical Sciences and Materials 2022 (ICAPSM 2022) organized by KPR Institute of Engineering and Technology, Coimbatore, Tamil Nadu on 19.08.2022
2. "Effect of pH on the optical and structural properties of SnS prepared by chemical bath deposition method" in the Second International Conference on Materials

Science and Manufacturing Technology 2020(ICMSMT 2020) held at Hotel Aloft, Coimbatore, Tamil Nadu on 9.10.2020.

3. “Effect of deposition parameters on the properties of PbS/CdS thin film prepared using SILAR method” in ISRO and KSCSTE sponsored international Conference on Advanced Materials organized by Nirmalagiri College, Kannur held on 14.6.2019
4. "Preparation and characterization of PbS thin film using SILAR method", Materials, Methods and Sensors for Electromagnetic Applications - emMET-II, KSCSTE Sponsored National Seminar held at Christ College (Autonomous), Irinjalakuda from 24 - 25 January 2019.

Chapter 1

Introduction

1.1 Thin films

The physical and chemical sciences are home to the relatively new and rapidly expanding discipline of thin-film technology. Its application is broadened when integrated with material science. The use of thin films in electrical, optoelectronic, and other devices will be considerably aided in the future by the ability to regulate the properties of the thin films. Thin films and coatings, which are essential to the development of contemporary science and technology, will continue to be heavily utilised in the next generation of computing and information technology, new energy devices, biology and life science, medical advancements, aerospace engineering and aeronautics, geology and ocean engineering, military science, as well as other fields. [1]–[4]. Figure 1.1 represents the different applications of thin films.

Condensation from atom to atom or molecule to molecule is the procedure utilised to produce the thin film on a substrate. They typically have a few microns or less in thickness. There are many benefits when comparing thin films to bulk materials. The microstructure of thin films and bulk materials can vary greatly in terms of grain size and other characteristics. [5]–[7].

The demands of a country's industrial sectors ultimately determine how effectively this field is applied, but it also intrinsically relies on the development of surface and interface research and the precision of the related mass manufacturing technologies. Thin films are fragile while being relatively rigid and having good thermal stability. Undoubtedly, the creation of high-performance devices for industrial usage requires the development of low-cost, large-scale thin-film fabrication processes. [8], [9].

Theoretical developments, compelling innovative notions in basic physics and chemistry, particularly condensed matter physics and interface chemistry, and the development of

characterization tools, in addition to improvements in fabrication and synthesis procedures, are the sources of each innovation in this sector. [1], [10].

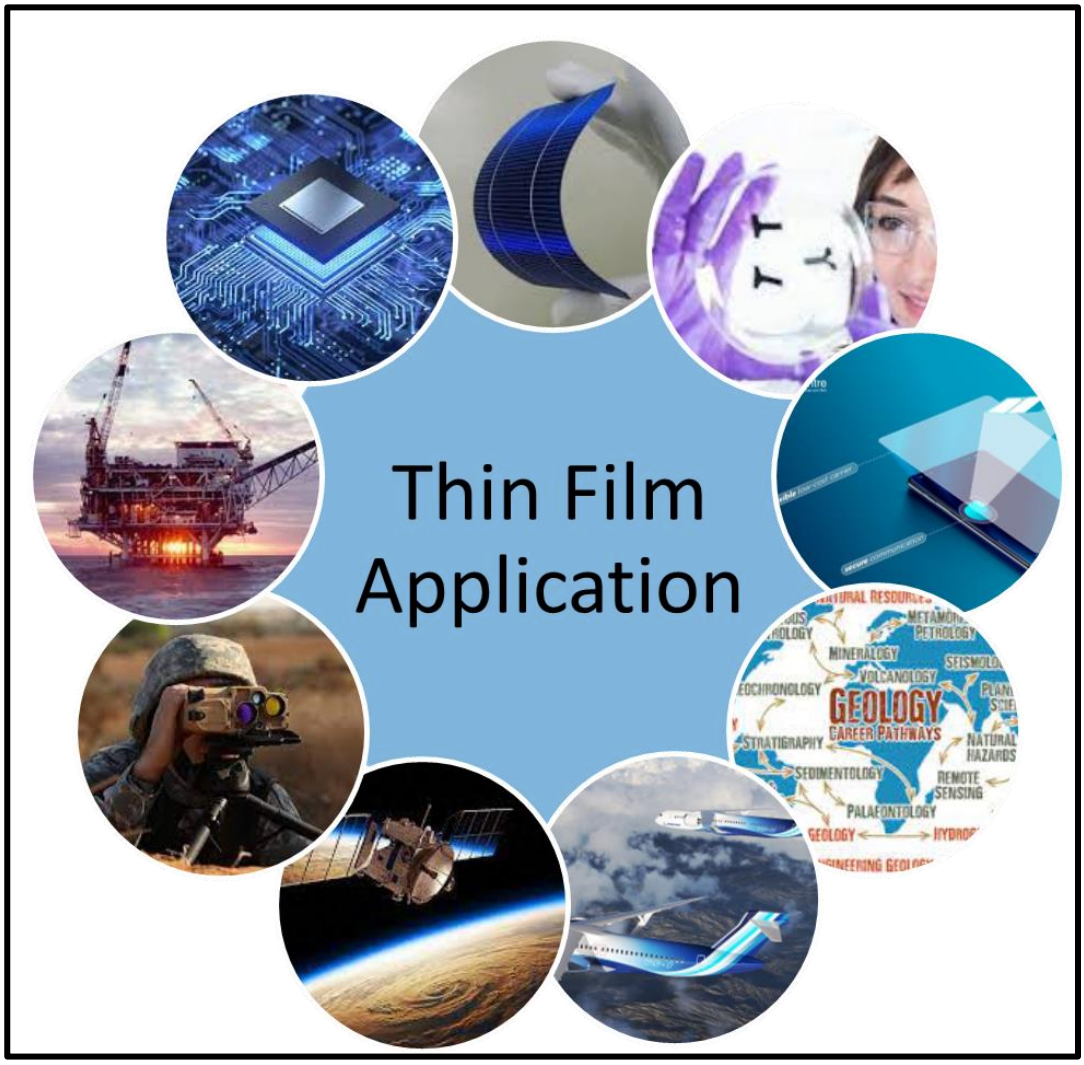

Figure 1.1 Applications of thin films

1.2 Solar cells

The most powerful energy source that the world receives is sunlight, which is produced by the sun. The total solar energy incidence on earth is significantly more than the world's current and future energy needs. [11], [12]. Because it would be expensive to expand the conventional electric power utility grid there, it is not always possible to install electric lighting, common household appliances, television receivers, and other communications equipment in remote locations. Installing necessary—yet perhaps little-noticed—electronic

equipment like remote automatic weather stations, microwave telephone repeaters on mountain tops, and earth-bound navigational aids for ships and commercial aircraft is also difficult due to the difficulty in supplying electric power. But in recent years, photovoltaic (i.e., crystalline silicon solar cell) construction has become a viable option for meeting some difficult electrical power requirements in both undeveloped and industrialized countries. [13].

The installed capacity for non-fossil fuel electricity, which includes significant hydro, nuclear, and renewable energy sources, is estimated by the Central Electricity Authority of India to be 37%, as shown in figure 1.3. India's Ministry of New and Renewable Energy has categorised renewable energy sources into four primary categories: wind, solar, small hydro, and bioenergy. 9% of them are solar energy. [14]–[16].

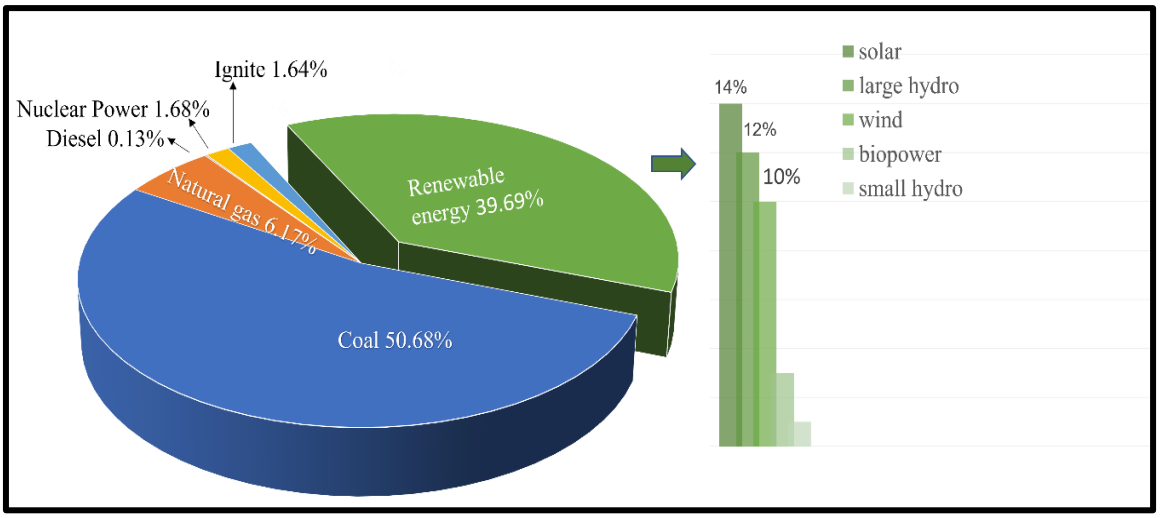

Figure 1.2 Cumulative power capacity of India (Data from Mercon solar tracker as on 30 June 2022)

Photovoltaic cell installations are increasing as a result of the increased demand for sustainable energy generation, but wider acceptability will probably depend on resolving the following problems: The main issues with the various solar cells are efficiency and cost. The crystallization process is highly costly in the case of a monocrystalline cell. Polycrystalline silicon cells go through comparable crystallization processes; however, these cells have structural issues. To maximize the solar cells' ability to convert sunlight into usable energy, researchers are putting a lot of effort into developing a silicon alternative. Due to this, the field of study into photovoltaic cells is intriguing and expanding. [17].

1.2.1 Construction and working principle of a solar cell

A solar cell, also known as a photovoltaic cell or PV cell, is a type of electrical device that converts light energy into electrical energy by using the photovoltaic effect. A solar cell is essentially a p-n junction diode. When exposed to light, a photoelectric cell changes its electrical characteristics, such as current, voltage, or resistance. This category includes solar cells.

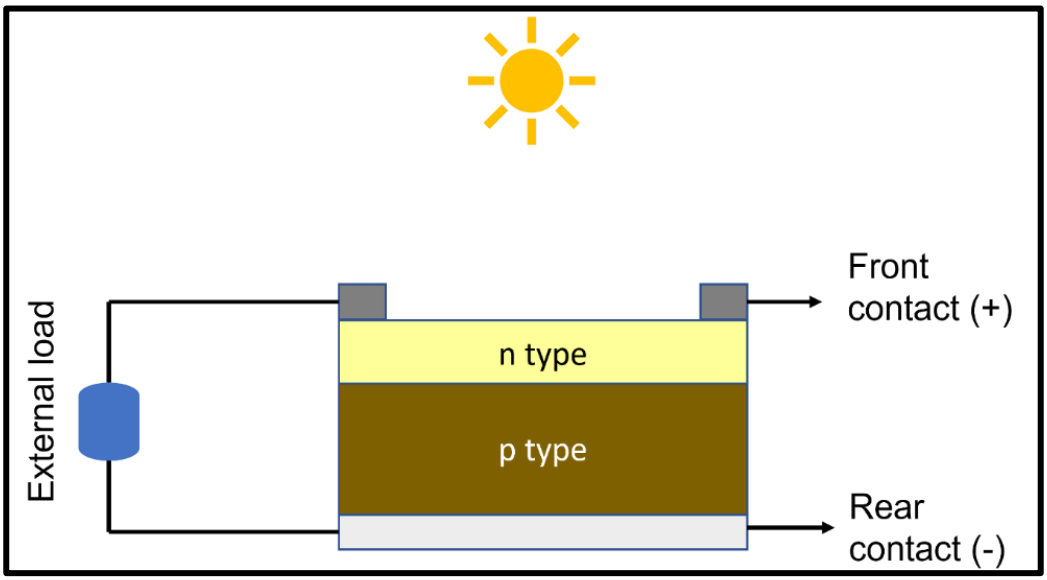

Figure 1.3 Schematic diagram of solar cell.

Figure 1.3 shows the schematic diagram of a solar cell. A junction diode is essentially what a solar cell is, although having a somewhat different design from typical p-n junction diodes. A very thin layer of n-type semiconductor is created on top of a slightly thicker layer of p-type semiconductor. The top of the n-type semiconductor layer is then populated with a few tiny electrodes. Light does not get blocked by these electrodes from reaching the n-type layer. Just below the n-type layer is where the p-n junction is located. At the base of the p-type layer, a current-collecting electrode is further provided.

The connection receives enough energy from the photons from the light source to create several electron-hole pairs. Free electrons in the depletion zone have a high mobility to the n-type side of the junction. The p-type side of the junction may be easily accessed by the holes, just as the depletion. Once they reach the n-type side of the junction, newly created free electrons cannot continue to cross it due to its barrier potential. Similar to this, the newly

produced holes are subject to the same barrier potential as the junction when they approach the p-type side of the junction. As one side of the junction, the n-type side, experiences higher electron concentrations and the other side, the p-type side, experiences higher hole concentrations, the p-n junction will behave like a small battery cell. If we connect a modest load to the junction, a current will flow across it once a voltage has been established. [11], [18], [19].

1.2.2 Generations of solar cells

Due to the development of several novel non-conventional manufacturing processes for producing functional solar cells, photovoltaic technologies can be divided into three main generations, as shown in Figure 1.4.

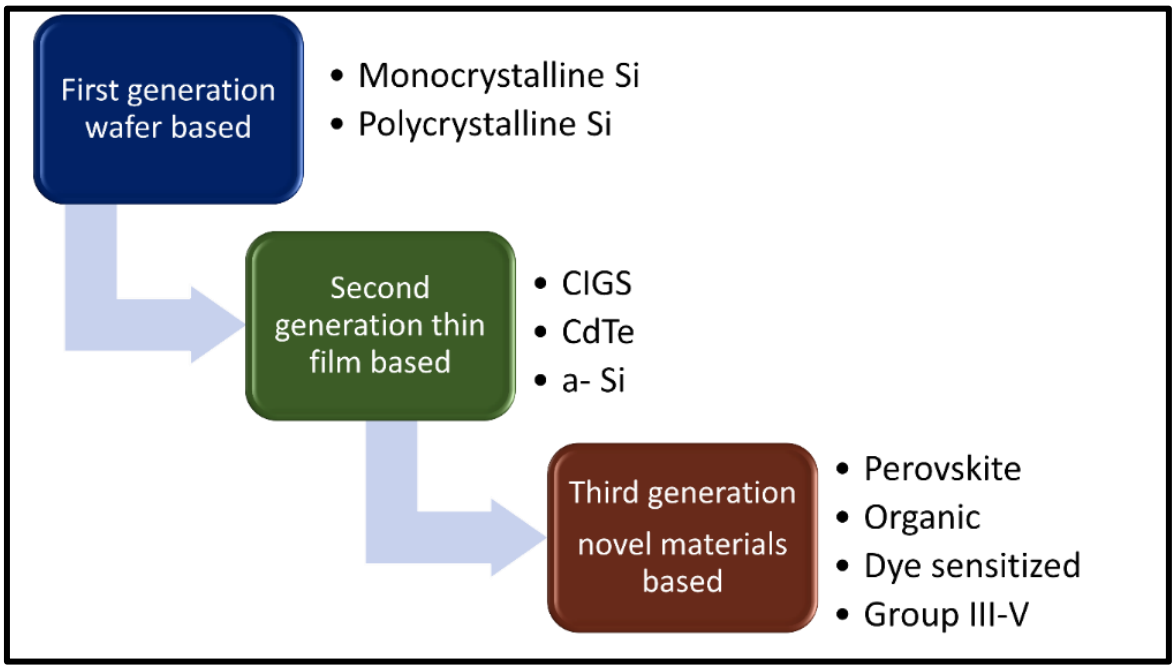

Figure 1.4 Generations of solar cells

Solar cells made of silicon, which can be categorized into single-crystal and polycrystalline varieties, dominate the market. Due to the extended payback period and the high energy requirements associated with silicon purification, the cost may be prohibitive. About 24.2% of monocrystalline crystals have efficiency, while 19% of polycrystalline crystals do. Second-generation solar cells are also known as thin-film solar cells. The main types that belong under this group (CIGS) include amorphous silicon and two types of solar cells made

of non-silicon materials, cadmium telluride (CdTe) and copper indium gallium diselenide. In addition to silicon, a variety of new materials are being employed to make this next generation of solar cells, including nanotubes, silicon wires, organic dyes, conductive polymers, and solar inks produced using traditional printing press technology. Of course, the goal is to improve the solar cells that are now on the market by increasing their efficiency over a wider range of solar energy, decreasing their cost so that more people can use them, and creating new inventive uses. [16], [20]–[23].

1.2.3 Parameters of a solar cell

A solar cell's conversion efficiency is influenced by a number of factors. Knowing the I V properties of a solar cell, which are depicted in figure 1.5, is necessary to comprehend these parameters. The working temperature of the cell is equal to 25 ^{o}C, and the corresponding solar radiation is 1000 W/m^2, according to the specifications provided by manufacturers under the STC (Standard Test Condition) [24]. The characteristics of the solar cell are as follows:

Short Circuit Current (I_{sc}):

The short circuit current, which is measured in amperes (A) or milliamperes (mA), is the greatest current a solar cell can produce. Figure 1.6 demonstrates that there is no voltage while the cell is providing the highest current. Short circuit values vary depending on the cell's area, the amount of solar energy it receives, its technology, and other things. The current density may occasionally be used in place of the current. J_{SC} stands for short-circuit current density, while J stands for current density. The short-circuit current density is derived by dividing the short circuit current by the surface area of the solar cells. [24]–[26].

Open Circuit Voltage (V_{oc})

The maximum voltage a cell may produce in an open circuit is known as the open circuit voltage. It is stated as a millivolt (mV) or volt (V). Figure 1.6 demonstrates that the current is equal to zero when the cell is producing its maximum voltage. The value of V_{OC} is influenced by both the technology and operating temperature of the cell. [24], [26], [27].

Maximum power point (P_{max})

The power that a solar cell can produce at the STC is represented by the maximum power point. The cell can operate at a range of voltages and current to voltage ratios. It can only produce its maximum power at a particular voltage to current ratio, though. According to figure 1.6, the maximum power point is located at the I-V curve's knee and is equal to the product of I_{mp} and V_{mp}. [27].

Fill factor (FF)

The area enclosed by the I_{mp}-V_{mp} rectangle and the Isc-Voc rectangle are shown in figure 1.5 as dotted lines. The fill factor is a measure of the squareness of the I-V curve. It is the ratio of the maximum power that a solar cell can really supply to the maximum power under ideal conditions. The better the cell, the higher the percentage fill factor, which is given as a percentage (%). The following equation can be used to calculate the fill factor. [27]:

$$FF(\%) = \frac{P_{max}}{I_{sc} \text{ x } V_{oc}} \times 100 \qquad (1.1)$$

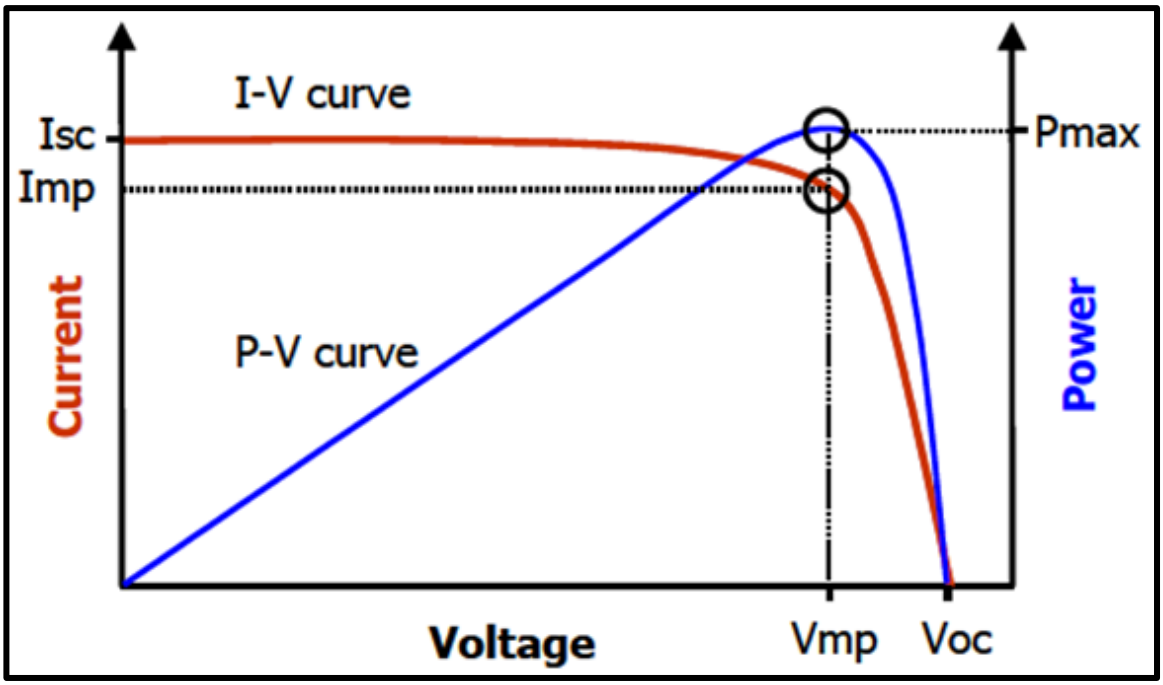

Figure 1.5 I-V characteristics of a solar cell [25].

Efficiency (η)

The ratio of the maximum output power (P_{max}) to the input power (P_{in}) represents the solar cell's efficiency. Its percentage (%) representation denotes the percentage of solar energy that is converted into electricity. [27].

$$\eta(\%) = \frac{P_{max}}{P_{in}} \times 100 = \frac{I_{sc} \text{ x } V_{oc}}{P_{in}} \text{x } FF \times 100 \quad (1.2)$$

The cost and sustainability of PV energy production are directly impacted by the solar energy conversion efficiency (η). A PV power plant needs less material and space the more valuable it is. A lot of attention has been paid to and will continue to be paid to the study of appropriate materials and material combinations for high values as well as the development of technologies enabling the realization of maximum in mass production with little resources.

1.3 Tin chalcogenides

Due to their semiconducting qualities, tin chalcogenides of the form SnE, where E = S, Se, or Te, have recently received a lot of interest. These materials have the potential to be used in optoelectronic and photovoltaic applications since they typically exhibit strong electromagnetic absorption and small band gaps. Tin is less poisonous than many other elements used in semiconductor materials and is, in fact, a fairly common metal on Earth. The controlled deposition of tin chalcogenide thin films and the production of tin chalcogenide nanocrystals with tunable band gaps have attracted a lot of attention. Tin chalcogenide thin films may be used in photovoltaic devices, and the photovoltaic, photonic, and optoelectronic potential of these materials' nanocrystals make them appealing [28]–[30].

1.4 Tin sulphides

Tin sulphides are a group of IV-VI semiconductors that come in SnS, SnS_2, and Sn_2S_3 as their three major forms. Tin has a range of bonding inclinations, most frequently tetrahedral, trigonal bipyramidal, and octahedral, and can adopt coordination numbers between 2 and 9. Herzenbergite, a distorted NaCl structure with firmly bound double layers of Sn and S atoms, is where SnS crystallizes. Van der Waals forces serve as a tenuous bond between the layers. Each Sn^{2+} ion is linked to six sulphur atoms in an octahedral geometry with three short and three long links. The PbI_2 layered structure, in which the Sn^{4+} centers are coupled to six sulphur atoms, is where tin disulfide (SnS_2) is most frequently found. A detailed

coordination chemistry of tin sulphides has been constructed and explored by Ozin et al. [31] Over seventy distinct forms with hexagonal close package layers but differing c parameters in the unit cell result from the polytypes seen in SnS_2. Sn_2S_3 is a mixed valence compound with a structure resembling a ribbon. Sulfur is coordinated with the Sn^{2+} ion through two Sn-S distances of approximately 2.6 and 2.7 in a trigonal bipyramidal shape. Attention has been drawn to tin sulphides as affordable, sustainable materials for photovoltaic solar energy absorbers. The tin sulphides SnS, SnS_2, and Sn_2S_3 have bulk band gaps of 1.3 eV, 2.3 eV, and 1.1 eV, respectively. All tin sulphide forms are semiconducting, but as previously stated, SnS has garnered the most attention due to its direct electronic band gap of 1.3 eV, which is comparable to the current industry standard conventional semiconductors, gallium arsenide and silicon [28], [32], [33].

1.5 SnS thin films

Orthorhombic tin monosulfide (SnS), which is abundant on Earth and has ideal electronic properties such as an ideal bandgap (~1.3 eV), a high optical absorption coefficient of 10^4 cm^{-1} which means an absorption length of 4μm , and intrinsic p-type conductivity, has attracted a lot of interest [34]–[36]. Due to its amphoteric nature, this molecule is chemically stable in both acidic and alkaline conditions [37]. Additionally, SnS compound has a surface that is inert and has minimal surface states. By doing so, the carrier recombination losses caused by flaws at p-n junctions and grain boundaries might be reduced. The orthorhombic structure of SnS is displayed in Figure 1.6. The p-type electrical conductivity arises due to the dominance of Sn-vacancies over S-vacancies [38]. Even in the presence of oxygen and moisture in the atmosphere, SnS is stable. Furthermore, SnS is non-toxic [3], [39]. Most often, the orthorhombic crystalline form of tin monosulfide (SnS) forms, cubic structures also exist [40].

Vacuum evaporation [41]–[43], sputtering [44]–[46], CVD [47], [48], electrodeposition [3], [49], pulsed-laser deposition [50], spray pyrolysis [51]–[53], SILAR [54], [55], and chemical bath deposition (CBD) [40], [56], [57] are some of the techniques used for the preparation of SnS thin films.

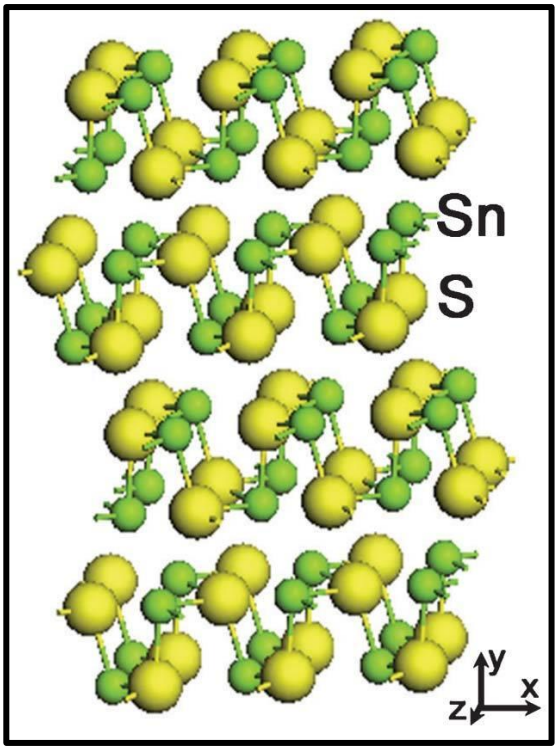

Figure 1.6 Orthorhombic SnS crystal structure [24]

1.6 Photovoltaic property of SnS thin films

The consumption of energy has risen gradually along with civilization. The need for clean, renewable energy has grown as a result of the energy crisis associated to global warming caused by depleting fossil fuel supplies and rising carbon dioxide emissions. [12]. One of the numerous ways that solar energy may be used to produce renewable energy is through the usage of photovoltaic systems, which has been growing tremendously quickly over the past few decades. As a renewable energy source that is both environmentally beneficial and commercially viable, solar cells have a lot of potential. [1]. Silicon-based solar cell technology dominates the solar cell industry [58]. Despite these ongoing advances, a crystalline silicon-based solar cell's best yield to date is just about 25%.

As a potential absorber material for solar cells, orthorhombic tin monosulfide (SnS), which is abundant on Earth and has ideal electronic properties such as an ideal bandgap (~1.3 eV), a high optical absorption coefficient of 10^4 cm^{-1}, and intrinsic p-type conductivity, has attracted a lot of interest [2-4]. Charge transmission between SnS thin layers is supposedly

resistant to flaws and impurities, unlike in silicon, which needs high purity and crystal perfection to generate efficient but expensive solar cells. Even in the presence of oxygen and moisture in the atmosphere, SnS is stable. These characteristics make it the ideal absorber material for thin-film solar cells. It is anticipated that its energy conversion efficiency will be close to 32% [35], [61], on par with that of crystalline silicon. However, the maximum reported power conversion efficiency (η) of SnS-based solar cells is 4.8% [13], [34]. Numerous studies have been done to improve the efficiency of SnS based solar cells so that they can replace the costly and scarce materials used in current solar cells.

1.6.1 Review on SnS based solar cells

Low efficiency values have been reported despite recent efforts to improve SnS-based solar cells, with the best value of 4.36% obtained in 2021. Naguchi et al. [62] reported in 1994 a photovoltaic structure made of SnO_2: F/CdS/SnS (ZB)/SnS (OR) with an evaporated Ag-electrode with V_{OC} = 120 mV, J_{SC} = 7 mA/cm^2, FF = 0.35, and η = 0.29% under 1 kW/m^2 (1 Sun) of light. Bashkirov et al. [46] described the preparation process and the Mo/p-SnS/n-CdS/ZnO heterojunctions' chemical, structural, and physical characterization findings in 2012 with V_{OC} = 132 mV, J_{SC} = 3.6 mA/cm^2, FF = 0.29, and η = 0.5 %. Orthorhombic SnS (OR) and Zinc-Blende SnS (ZB) are two different crystalline forms of SnS that were chemically deposited by Avellaneda et al. [36] in 2013. These films had bandgap energies of 1.2 and 1.7 eV as well as p-type conductivity. In this paper, the following values were measured for SnO_2: F/CdS/SnS (ZB)/SnS (OR) photovoltaic: V_{OC} is 370 mV, J_{SC} is 1.23 mA/cm^2, FF is 0.44, and efficiency is 0.2%.

With a device configuration of glass/Mo/SnS/SnO_2/Zn (O, S): N/ZnO/ITO, Sinsermsuksakul et al. [39] reported the highest certified efficiency of 4.36% for atomic-layer-deposited (ALD) SnS-based TFSCs employing Zn (O, S): N n-type buffer layer in 2014. The highest efficiency of 4.225% for SnS/CdS heterojunction TFSCs, was reported by Jae Yu Cho et al., together with a *V*oc of 0.346 V, a *J*sc of 20.76 mA cm-2, and a FF of 0.588. By enhancing the heterointerface quality of the VTD-grown SnS absorber and CBD-grown CdS buffer layer, the device's performance was increased.

Getting cell efficiency above 4% for SnS-based TFSCs has remained a significant challenge in spite of these intriguing achievements. Generally speaking, removing the following performance barriers is seen as crucial for SnS- based solar cells. They are the defects in the film and, the formation of the secondary phases, and the band alignment. A further improvement in efficiency can be made by using back reflectors and anti-reflective coatings. One of the biggest problems for SnS technology could be locating a single suitable buffer material. Some works have concentrated on identifying a better buffer candidate to solve that issue. If the two component materials have a considerable lattice mismatch, the SnS/buffer junction's ability to lower open circuit voltage could be characterised by a high interfacial defect density. Poor film quality, i.e., polycrystalline films with several secondary phases, may also be to fault for the poor performance. The range of 1.83-1.92 found for SnS device diode quality factors indicates significant recombination in the space charge region (SCR). These losses are mostly caused by bulk states and/or interface defects, which are strongly influenced by the deposition process. Therefore, to increase solar cell output, crystalline quality must be improved. [13].

1.6.2 Light trapping approaches in solar cell

Adding a surface grating or another scattering layer next to the uniform absorption layer is one of the typical ways to capture light. Although the increased light-trapping in thin film solar cell systems is frequently achieved by light scattering phenomena using a textured metal back reflector (for example, silver (Ag) coated with zinc oxide (ZnO)) within the

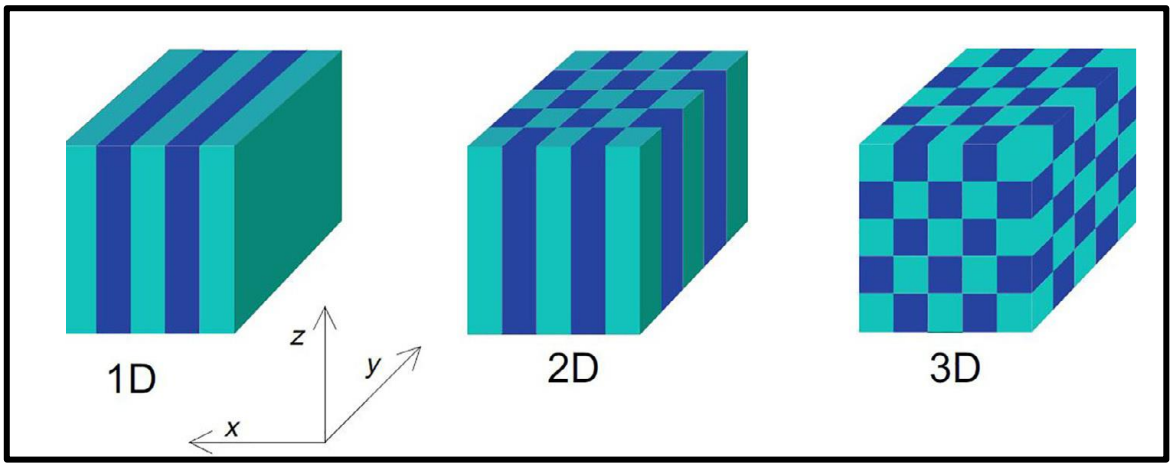

Figure 1.7 Classification of photonic crystals [45]

absorption layer, it exhibits intrinsic losses that come from the surface plasmon modes produced at the interface of granular metal-dielectric in the back reflector. Such intrinsic losses (those reported for Ag back-reflectors are 3%-8% with each reflection at 650 nm) accumulate quickly and result in even higher losses at longer wavelength regions where the photons' absorption lifetimes in the absorber layer lengthen and need several optical passes [63].

Numerous promising light management/trapping structures and ideas, such as photonic crystals (PCs) [64], plasmonic nanostructures [65], honeycomb pattern substrates [63], low pressure chemical vapor deposited-ZnO [66], chemically etched ZnO [67], modulated surface textures [68], and textured glass [69], have been thoroughly studied in recent years for enhancing and optimizing photon absorption. The periodic structure and the capacity to control photon transmission of photonic crystals PCs, also known as photonic bandgap structure, an artificial material with periodic dielectric constants in one, two, or three dimensions as shown in figure 1.7, make it one of the most intriguing of these [63], [69]. Photonic crystals deliver a special form of light-trapping that is suitable for absorbing sunlight's whole spectrum. The improvement of average photon absorption and solar cell efficiencies depends on the greater capture of longer wavelength photons [63], [70].

1.6.3 Photonic crystals

PCs, are a class of substance that can change how light travels through space. They are the optical equivalent of crystals, in which variable dielectric constants have taken the place of the atoms or molecules. As depicted in figure 1.7, photonic structures first appeared in nature many hundreds of millions of years ago in opals, butterfly wings, etc. The periodic potential brought on by crystal periodicity is replaced by periodic dielectric function. Because of this, light that travels through PCs behaves exactly like crystalline solid electrons [71], [72].

Light cannot move in a certain direction because of a band gap caused by periodic dielectric potential. Depending on whether the periodicity of the dielectric material is along one, two, or three axes, photonic crystals can be categorized as one-dimensional (1D), two-imensional

(2D), and three-dimensional (3D). Only when the dielectric periodicity is along three directions is the full photonic band gap produced [73].

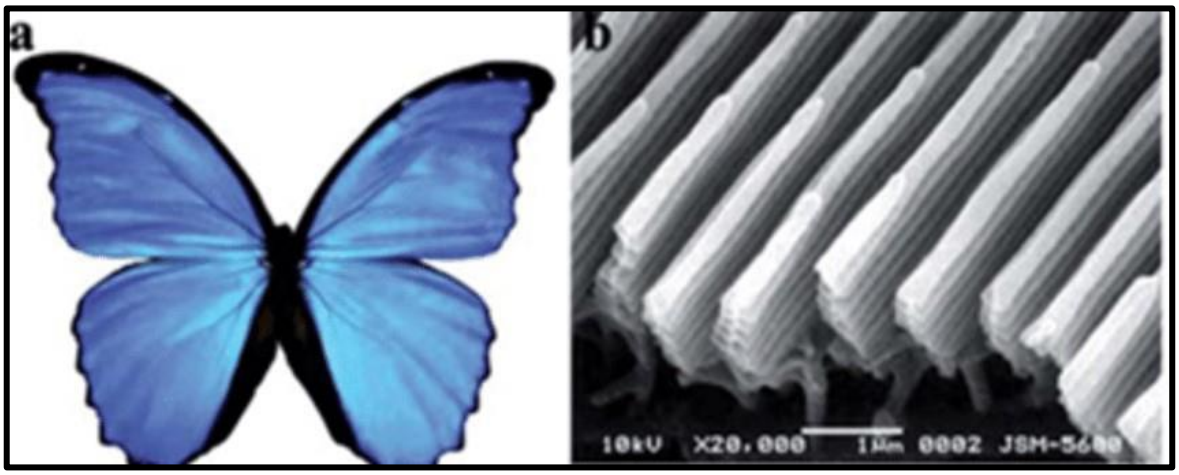

Figure 1.8 Photonic crystals in nature [52]

Methods of fabrication include Electron Beam Lithography [74], Nanoimprint Lithography [75], molecular beam epitaxy [76], Chemical vapor deposition (CVD) technology [77] and holographic exposure of ultraviolet (UV) beams to photosensitive materials [78], [79]. Computer simulations work better as the pre-laboratory for PCs. It will simplify and improve the comfort of designing. The theoretical prediction can be put into practice in labs because all of the material properties are well understood and the length scale is not too small.

Increasing of the efficiency of the SnS solar cells is related to the increase of the absorption of the incident light in the absorber layer via light-trapping concepts. A promising approach to increase the absorption of the thin film Si solar cells is formation of back reflector. In this work ZnO/SiO2 multilayer 1-D photonic crystals as back reflectors for enhancing the absorption in the absorber layer.

1.7 Significance of the study

The relevance of thin film solar cells as an efficient technology to deliver clean, renewable, and affordable energy is highlighted by recent breakthroughs in energy generation. In order to replace the current technology based on scarce, expensive, and poisonous components, thin film solar cells produced from earth-abundant, non-toxic materials with sufficient physical features, such as band-gap energy, large absorption coefficient, and p-type

conductivity, are required. Since tin sulphide has a high theoretical photoelectron conversion efficiency (>20%), is less poisonous, has strong chemical stability, and has constituent elements that are plentiful in the earth's crust, it has been selected for this application. The reported power conversion efficiency (η) of SnS-based solar cells, however, remained under 4%. The ability to produce high-quality SnS thin films and selecting the appropriate n-type semiconductor are two potential barriers to improving the efficiency of SnS-based solar cells. The work here attempted to do this.

In recent years, there has been a lot of interest in developing photon management strategies to maximize light absorption for applications including solar cells, photo electrochemistry, and sensing. The movement of light can be controlled via photonic crystals, which are thought of as the optical equivalent of crystals. In this study, the free and open programme MEEP was used to simulate 1D PC. Investigated were the effects of layer count and dielectric contrast on the photonic band gap. Sputtering was used to create 1D PC made of ZnO/SiO_2. The simulated results and the experimental findings agreed. Because it saves time and money, simulation is always preferable to pre-laboratories.

Chapter 1

Chapter 2

Preparation and Characterization Techniques

2.1 Introduction

Since all microelectronic solid-state devices are built on material structures made by thin-film deposition, deposition technology can be considered to be a vital component in the development of devices. Electronic engineers have consistently required more sophisticated and high-quality films for solid-state devices, necessitating a quick advancement in deposition technology. The criteria for better and more affordable deposition systems, as well as for in-situ process monitors and controls for measuring film parameters, have been successfully satisfied by equipment makers. The better knowledge of the physics and chemistry of films, surfaces, interfaces, and microstructures made possible by the extraordinary developments in analytical instrumentation over the past 20 years is a significant factor in the quick development of deposition technology [80].

2.2 Thin film deposition techniques

When an individual atomic, molecular, or ionic species is caused to condense onto a solid substrate either physically or through ultra-chemical reactions, the solid substance is said to be in thin film form. There are countless deposition processes available for the creation of materials. Limiting the number of approaches to be taken into consideration makes the process of classifying the techniques easier because the focus is on thin-film deposition methods for creating layers with thicknesses ranging from a few nanometers to roughly ten micrometers [81]. Essentially, thin-film deposition technologies are either fully physical, like evaporative techniques, or purely chemical, like chemical processes that take place in the gaseous and liquid phases. Many glow discharge and reactive sputtering-based procedures mix physical and chemical reactions; these overlapping processes can be classified as physical-chemical methods [5], [80], [81]. Figure 2.1 represents the classification of the thin film deposition method. Here Chemical bath deposition method and

magnetron sputtering methods were utilized for the thin film production. In the following session these methods are briefly explained.

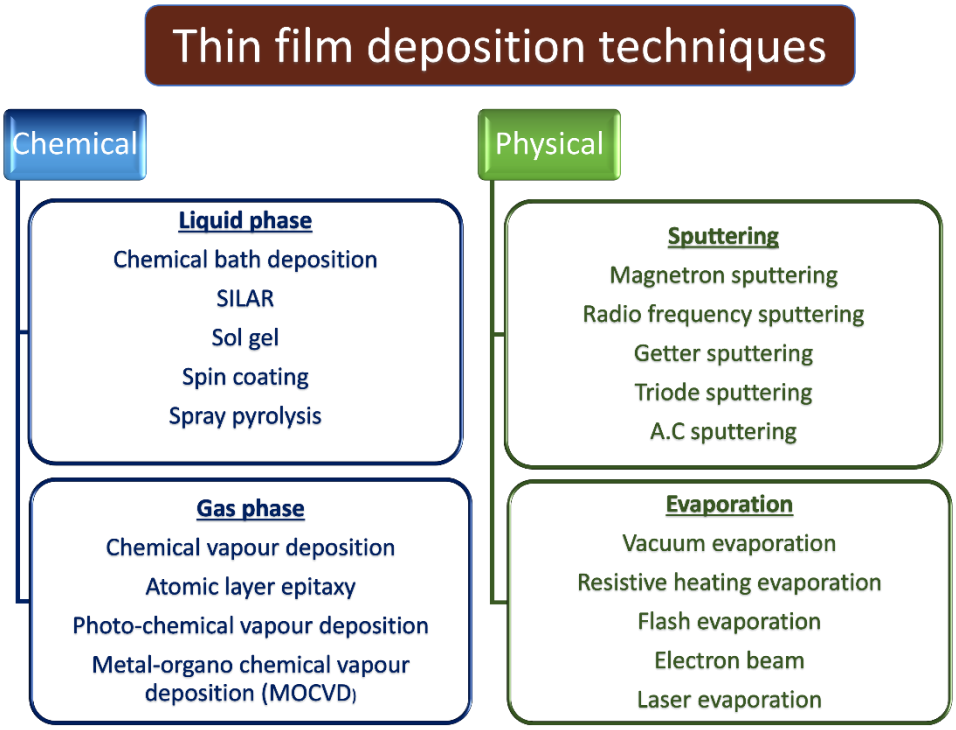

Figure 2.1 Classification of thin film deposition techniques

2.2.1 Chemical bath deposition method

The controlled precipitation of a chosen component from the solution onto the appropriate substrate is the goal of the chemical bath deposition technique. Compared to the more suited vapors phase approaches to semiconducting thin film, this method has numerous advantages. The following are some benefits or reasons to choose this strategy above all other options:

- This method is the simplest and most economical one.
- With this method, multi-compound chalcogenide thin films can be created over a wide range of stoichiometry.
- Chemicals can be used even at ambient temperature and do not require a high vacuum.
- By properly placing the substrate on a shallow tray containing the deposition bath, large area deposition is achieved.

- Creates consistent, reproducible, well-adhered thin films for photovoltaic applications.
- A cheap technique for extensive industrial applications
- Low material use lowers the risk of loss.
- If the right reagents are employed and the solution is kept at a specific pH for an extended period of time, CBD is not a time-consuming procedure and the CBD unit is safe to handle.
- Portable CBD unit

By adjusting the deposition parameters, such as temperature, precursor concentration, the use of complexing agents, and solution pH, this approach allows for precise control of the layer thickness and chemical composition. The most alluring benefit of this approach is its capacity to coat sizable surfaces in a repeatable and affordable process. This technique relies on the formation of thin films from aqueous solutions, either through the passage of a current or through chemical reactions when the right circumstances are present. These films typically aren't very pure due to their preparation conditions. A specific composition of thin films can be achieved with the proper control of the deposition conditions. When a solid substrate is submerged in a diluted solution of one or more metal salts, a source of chalcogenide, X (X=S, Se, Te) ion, and an appropriate complexing agent in an aqueous solution, thin films are deposited on the substrate in the CBD process. This process involves the following four phases for the formation of the metal chalcogenide films on the substrate:

- Achieving equilibrium between the complexing agent and the water
- Metal-complex species formation
- The chalcogenide source is hydrolyzed
- The solid film's formation on the substrate

When the value of the ionic product exceeds the solubility product, the film is deposited on the substrate; otherwise, it is precipitated out. An appropriate complexing agent normally complexes the metal ions, which would then gradually release metal ions during the reaction. The rate at which solid metal hydroxides form, which then results in the creation of solid film, is controlled by the formation of metal-complex ions. Therefore, in order to stop the precipitation of metal hydroxide, the metal ion needs to be complexed. To prevent bulk

precipitation or the deposition of the required film, the strength of the complexing agent should not be too strong or too weak. The fundamental idea behind CBD is to manage the chemical process so as to influence the thin film deposition by precipitation. The method relies on the gradual release of the chalcogenide ion into an alkaline solution that has a low concentration of buffered free metal ions.

The unit of the chemical bath deposition process is depicted in the figure below. It is made up of the holder that glass slides are attached onto. The material to be deposited is combined with the necessary ingredients in a beaker with the correct complexing agent, and the solution's pH is kept within the proper range. By taking a glass slide and continually washing it till the confirmation, the film is checked if it has been deposited on a glass substrate [82]–[84].

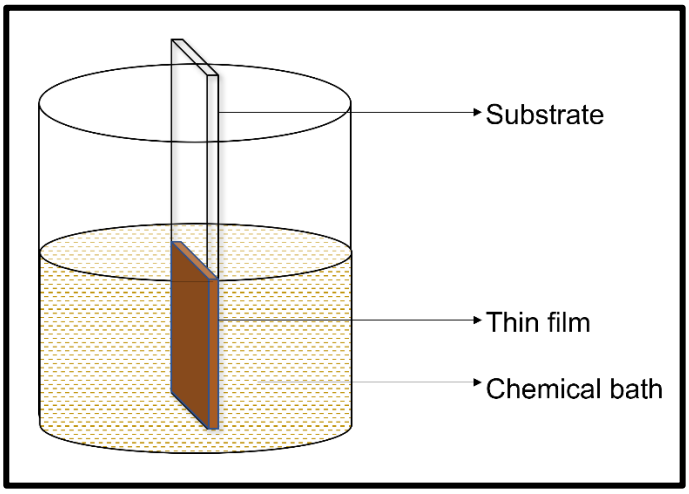

Figure 2.2 Schematic diagram of CBD method

2.2.2 Sputtering

The thin film deposition method at the heart of the current semiconductor, disc drive, CD, and optical device industries is sputtering. Sputtering is the process of ejecting atoms from a target or source material that is to be deposited on a substrate, such as a silicon wafer, solar panel, or optical device, as a result of the bombardment of the target by high energy particles, on an atomic level. A substrate to be coated is placed in a vacuum chamber with an inert gas, often argon, and a negative charge is delivered to a target source material that will be deposited into the substrate and cause the plasma to glow. This is the start of the sputtering

process. The negatively charged target source material releases free electrons into the surrounding plasma environment. These electrons collide with the outer electronic shell of the argon gas atoms and are driven away by their similar charge [2], [85].

When the inert gas atoms collide with the negatively charged target material, they form positively charged ions that are drawn to it at a rapid speed and "Sputters off" atomic-sized particles from the source material. As these particles go through the vacuum deposition chamber of the sputter coater, a thin coating of material is deposited on the surface of the substrate that will be coated. Sputtering only occurs in the "Fourth state of nature" plasma environment when the kinetic energy of the bombarding particles is extraordinarily high, much greater than typical thermal energies. In comparison to melting a source material with normal thermal energy, this can enable a far more exact and pure thin film deposition at the atomic level. The term "sputter yield" refers to the quantity of atoms "Sputtered off" or ejected from the target or source material. The energy and incident angle of the bombarding ions, the relative masses of the ions and target atoms, and the surface binding energy of the target atoms can all affect the sputter yield. Physical vapor deposition techniques like as ion beam and ion-assisted sputtering, reactive sputtering in an oxygen gas environment, gas flow, and magnetron sputtering are frequently employed in sputter coaters [86].

Magnetron sputtering: Ions are charged particles and can have their motion and behavior controlled by magnetic fields. Magnets behind the negative cathode are used in magnetron sputtering deposition to trap electrons over the negatively charged target material, preventing them from bombarding the substrate and allowing for quicker deposition rates. Circular and rectangular cathode/target forms are the most prevalent in magnetron sputtering. Larger size "In-line" systems, where substrates scan linearly past the targets on some sort of conveyor belt or carrier, are where rectangular magnetrons are most frequently used. More often than not, single wafer stations or smaller "Confocal" batch systems have circular sputtering magnetrons [2], [87].

Reactive sputtering: It involves injecting a gas to the vacuum chamber so that it can react chemically with the materials to be coated before coming into contact with them. Due to the high energy collisions, gases like nitrogen and oxygen that are ordinarily stable and inert become ionized and reactive in the plasma environment. When this occurs, the gas may

chemically interact with the cloud of target material to produce a molecular compound, which later transforms into the thin film coating. In the semiconductor business, silicon targets reactively sputtered with oxygen or nitrogen can create silicon oxide films, while doing the same with silicon nitride films [88].

Co-Sputtering: This is frequently combined with Reactive Magnetron Sputtering to create thin films that are compounds like alloys or composites, is the simultaneous sputtering of two or more target materials in the vacuum chamber. The optical and architectural glass industries make extensive use of it. The refractive index or shading effect of the glass can be carefully and precisely controlled on applications ranging from large scale surfaces such as skyscraper architectural glass to sunglasses by using Reactive Co-Sputtering of two target materials such as Silicon and Titanium with dual Magnetron Sputtering. Solar panel production uses it extensively as well.

The target material is bombarded using a variety of power sources, including DC and RF sputtering, pulsed DC, MF, and AC, as well as the recently developed HIPIMS sputtering techniques.

Direct Current Sputtering: With electrically conductive target materials like metals, DC or Direct Current Sputtering is the simplest and most often used method since it is simple to regulate and relatively inexpensive in terms of power usage. If at all feasible, DC sputtering can be a relatively cheap and efficient way to coat a variety of decorative metal coatings. The use of dielectric target materials, which are coatings made of insulating non-conducting materials capable of absorbing a polarized charge, is constrained by DC sputtering. Aluminum oxide, silicon oxide, and tantalum oxide are a few examples of typical dielectric coating materials. The gas in the vacuum chamber ionizes during DC sputtering. As a result, positive ions are generated, which collect on the target face's surface and charge it positively. The discharge of sputtering atoms can be stopped by this gradual development of a positive charge in the dielectric. Many techniques have been devised to pulse or alternate the sputtering power source in order to "clean" the target surface and stop it from becoming positively charged [88].

Radio frequency sputtering: To prevent a charge buildup at radio frequencies, RF or Radio Frequency Sputtering switches the electrical potential of the current. This method of

alternating the current has the effect of reversing the buildup that occurs when the current only flows continuously in one direction throughout each part of the cycle. Similar to DC magnetron sputtering, RF magnetron sputtering coaters increase the proportion of target atoms that are ionized, which in turn increases the growth of the thin film.

Pulsed DC sputtering: It is where the target is bombarded with powerful voltage spikes to clean the target face and prevent the buildup of a dielectric charge. These voltage spikes which clean the target surface are usually set at frequencies ranging from 40 to 200 KHz.

High Power Impulse Magnetron Sputtering: This is a recently developed sputtering method that makes advantage of a high current voltage spike to significantly boost the ionization of the sputtering target. Ionized atoms in these systems have substantially greater energies than in conventional sputtering methods, enabling the production of extremely thick thin film coatings.

Mid Frequency AC Sputtering: This is the most common method for producing non-conductive thin film coatings. When an AC current is switched back and forth between two cathodes, the target surface is cleaned after each current reversal [2], [5], [61], [88].

Here we have used RF magnetron sputtering for the deposition of ZnO/SiO2 1D photonic crystals which was used as back reflectors in SnS/CdS solar cell.

2.2.2.1 Working of RF magnetron sputtering

Figure 2.3 depicts the schematic diagram of the working of RF Magnetron sputtering. The coating materials are first applied to a magnetron in the shape of a target, which is a solid object. You need a sterile setting with only the materials of your choice for exceptionally pure coatings. To almost completely eliminate every molecule from the chamber, it is evacuated for this reason. After that, a process gas is refilled into the chamber. The kind of material to be deposited determines the choice of gas; common process gases include argon, oxygen, and nitrogen. The circumstances are now favorable for the procedure to start. The magnetron cathode, which is the target material to be sputtered, is given a negative electrical potential, while the chamber body serves as the positive anode or ground. Free electrons will speed away from the magnetron as a result of this electrical potential. A process gas atom is stripped of an electron when one of these electrons collides with it, resulting in the formation

of a positively charged process gas ion. The magnetron is approached more quickly by the positively charged ion. This ion has sufficient energy to "sputter" or "knock off" some of the magnetrons' target material. The target material will then gather on surfaces along the magnetron's path. Sputtered material accumulates on your substrate in this way. When the ions unite with free electrons again to form a lower energy state, light is produced from the plasma. Positively charged ions unite once more with unbound electrons to form a neutral atom. When the ions unite with free electrons once more to form a lower energy state, the plasma glow is produced. The "excess voltage" produced when a free electron recombines with an ion is released as light because the ion requires less voltage than the free electron. The glow of the plasma that is visible throughout processing is the light. Until the desired thickness is reached and the cathode is no longer powered, this thin film deposition process is carried out at a constant pace.

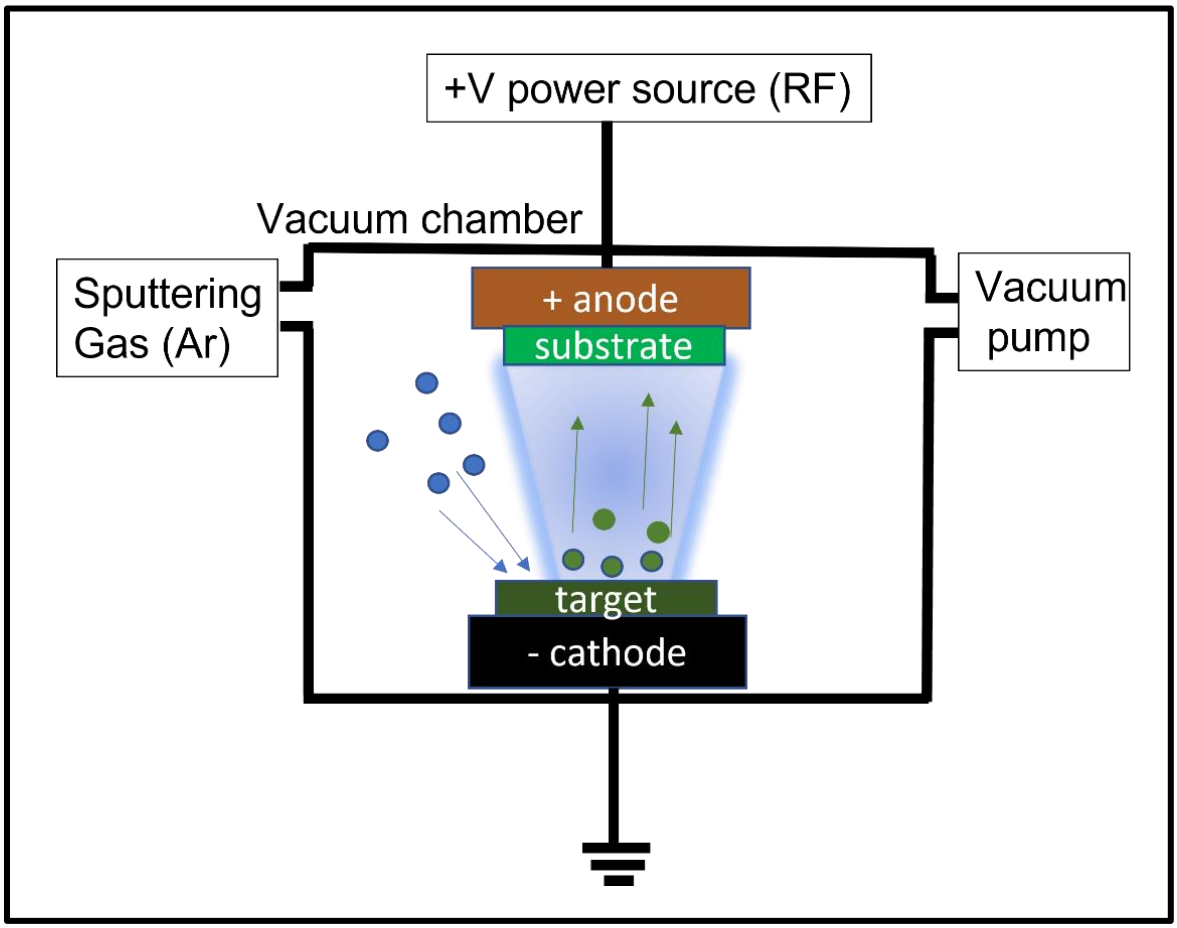

Figure 2.3 Schematic diagram of RF magnetron sputtering

2.3 Thin films characterization techniques

By characterizing the films using a range of investigative approaches, the growth mechanism and characteristics of the films can be explored in great detail. The most crucial factor in regulating material processing and regularizing performance is optimization. To get the best performance out of the films that have been created, one must characterize the films before employing them in applications. Phase analysis, compositional characterization, structural elucidation, micro-structural analysis, and surface characterization are all essential components of a material's comprehensive characterization and have a significant impact on its physical characteristics. This section includes concise description of the techniques that have used to characterize the thin films. X-ray diffraction, Raman spectroscopy, a field emission scanning electron microscope (FESEM), Energy dispersive X ray spectroscopy, UV- visible spectroscopy and Keithley source meter to conduct structural, morphological, compositional, optical and I-V studies.

2.3.1 X-Ray Diffraction (XRD)

An effective method for measuring the structural characteristics of these phases, including their strain state, grain size, epitaxy, phase composition, preferred orientation, and defect structure, is X-ray diffraction (XRD). The atomic configurations in amorphous materials (including polymers) and at interfaces, as well as the thickness of thin films and multilayers, are all determined by XRD. In order to determine the strain states in thin films, XRD is the method of choice since it provides unmatched accuracy in the measurement of atomic spacing. XRD is perfect for in situ studies because it is noncontact and nondestructive. The atomic configurations at interfaces can be determined quantitatively and accurately using the intensities recorded with XRD (e.g., in multilayers). Any element can be found in materials, however high-Z elements are the most sensitive to XRD because their diffracted intensity is substantially higher than that of low-Z elements. The material of interest determines the sensitivity of XRD as a result.

In general, diffraction only happens when the repetition distance between scattering centers is of the same order of magnitude as the wave motion's wavelength. This diffraction requirement is simply Bragg's law, which is expressed as

$$2d \sin \theta = n\lambda \quad (2.1)$$

where d is the interplanar spacing, θ is the diffraction angle, λ is the x-ray wavelength, and n is the order of diffraction. The interatomic spacing of crystalline solids' arranged atoms (referred to as unit cells) is comparable to the x-ray wave length (0.5 to 2.5Å). The schematic representation of Bragg's law is shown in figure 2.4. As a result, crystals make the best gratings for x-ray diffraction.

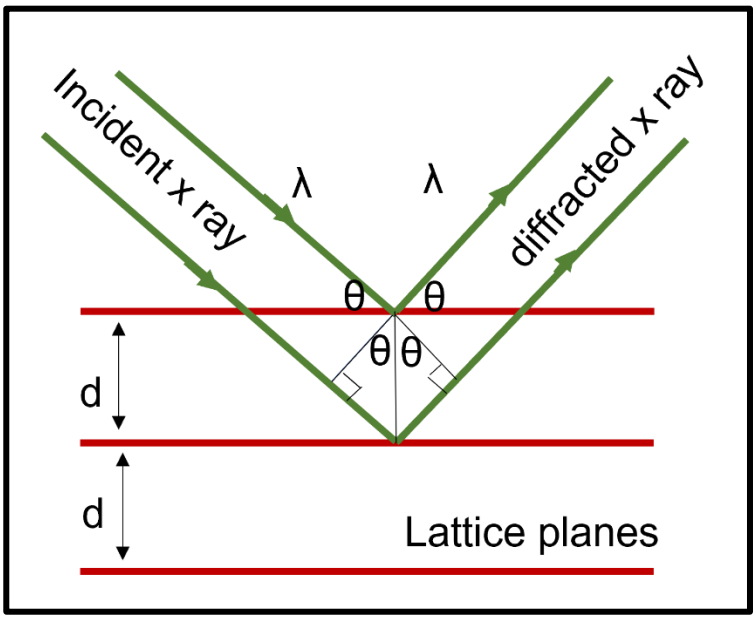

Figure 2.4 Schematic representation of Bragg's law

Studies using x-ray diffraction can confirm the crystal structure and phase development because the directions of diffracted x-rays reveal information about the atomic arrangements. It is determined how to satisfy Bragg's condition, which can be achieved by continuously adjusting either λ or θ throughout the experiment. Each sample particle is a tiny crystal, or an assembly of smaller crystals, that is randomly oriented with respect to the incident beam. Some of the crystals will be positioned correctly, allowing, for instance, their (100) planes to reflect the incident beam. For (110) reflections, for example, other crystals will be orientated appropriately. Every set of lattice planes will be able to reflect as a result. This is how a diffractometer works. According to Bragg's law, the constructive x-ray interference for a particular d value should, in theory, only happen for a specific θ or the Bragg's angle, while at all other angles there should be destructive interference, and the intensity of the diffracted beam will be at its lowest.

Phase identification is one of the most significant applications for thin-film XRD. The diffraction pattern's measured d-spacing and, to a lesser extent, its integrated intensities are compared to known standards in the JCPDS Powder Diffraction File (Joint Committee on Powder Diffraction Standards), and the reflections can be indexed with Miller indices, to achieve this identification. The peak corresponding to the diffracted beam is widened in proportion to the size of the diffracting tiny crystal, but if the size of the diffracting tiny crystal is minimal, there is no longer total destructive interference. Debye-Scherer provided the formula for the relationship, which is

$$D = 0.9\lambda / \beta \cos \theta \tag{2.2}$$

where D is the size of the particle, θ is the diffraction angle, X-ray wavelength is λ, and line broadening at full width at half maxima (FWHM) is β. Additionally, X-ray diffraction from thin films can be performed using the powder diffractometer. It is possible to think of epitaxial or polycrystalline thin films as single crystals or powders (crystals or assemblies of crystals dispersed across substrate), depending on whether or not they are orientated.

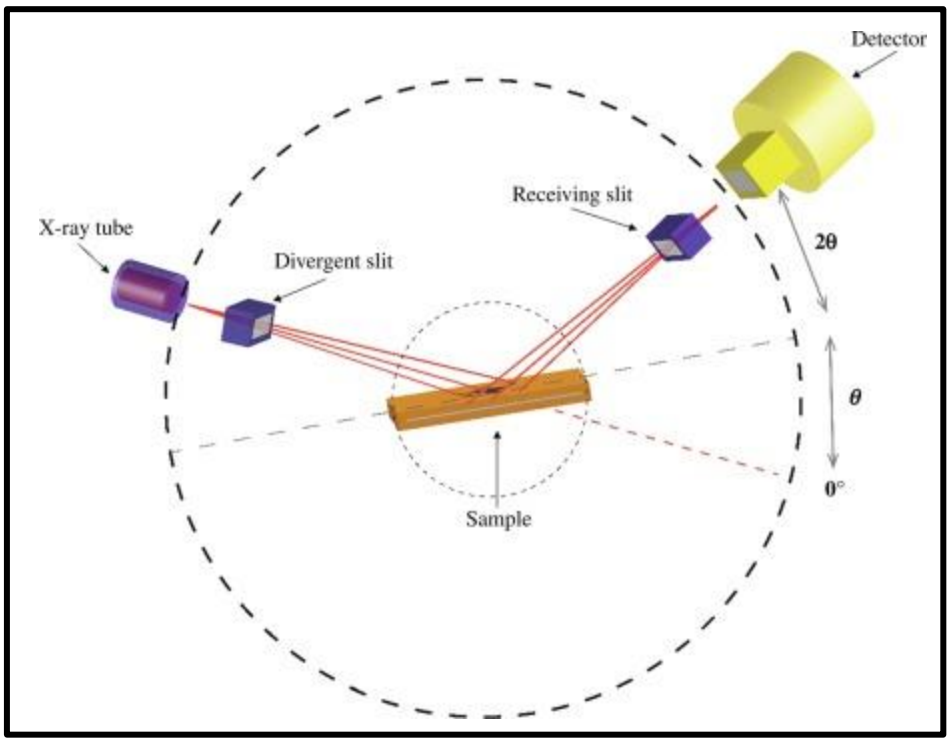

Figure 2.5 XRD instrumentation [66]

The instrumentation of XRD is shown in figure 2.5. The X-rays are produced by x ray tube. The tube has an exit window that allows x-rays to reach the sample. Between the sample and the analyzing crystal and between the analyzing crystal and the detector are two optical collimators. They are formed using curved mirrors or lenses. These tools focus the x-ray beam on a particular region of the sample. When the circumstances are in accordance with Bragg's law, the incident rays' interaction with the sample results in constructive interference (and a diffracted ray). Then, these diffracted X-rays are found, examined, and tallied. Due to the powdered material's random orientation, all feasible lattice diffraction directions should be obtained by scanning the sample across a variety of 2θ angles. An X-ray diffractometer's geometry is such that the sample spins at an angle u in the direction of the collimated X-ray beam and the X-ray detector rotates at an angle of 2θ to capture the diffracted X-rays. A goniometer is the device used to maintain the angle and spin the sample. This X-ray radiation is captured by a detector, which also processes it. The signal is then converted to a count rate and output to a printer or computer monitor. A variety of x-ray detectors, some used to count individual x-ray photons, others to measure count rate, total flux, or energy are used [89], [90].

2.3.2 Raman spectroscopy

A well-liked method for analyzing molecular structure, Raman spectroscopy is today regarded as an addition to infrared spectroscopy. The Raman effect, first discovered by Indian scientist Chandrasekhara Venkata Raman in 1928, serves as the foundation for Raman spectroscopy [91], [92]. Raman spectroscopy differs from the rotational and vibrational spectroscopy discussed above in that it focuses on the scattering of photons by simple processes rather than an absorption process. Molecules vibrate continually. Both Raman and infrared spectroscopy identify and assess the energy of the various molecule-level vibrations, which results in a spectrum. Every crystal or molecule has a distinct and individual Raman/IR spectra. Raman and infrared spectroscopy use radiation differently; in the latter, a broad spectrum of radiation covering the entire IR spectrum is aimed at the sample, and absorption occurs when the radiation's frequency precisely matches that of the vibration. Raman spectroscopy, in contrast, illuminates the sample with a single frequency source, and the light scattered from the molecule is what is picked up in the experiment. The

Raman scattering process is simple to comprehend. In the past 25 years, there has been a significant advancement in instrumentation, primarily in compact air-cooled solid-state lasers, holographic notch and edge filters to remove the strong laser line, high quantum efficiency, and low noise detectors like charge-coupled devices. These advancements have increased the sensitivity and simplicity of Raman systems as well as opened up new scientific fields for the use of Raman spectroscopy. Raman spectroscopy, which was formerly thought of as a method only used in research facilities, has begun to enter the industrial sphere [93]. The Raman spectrometer's basic configuration is displayed in figure 2.6.

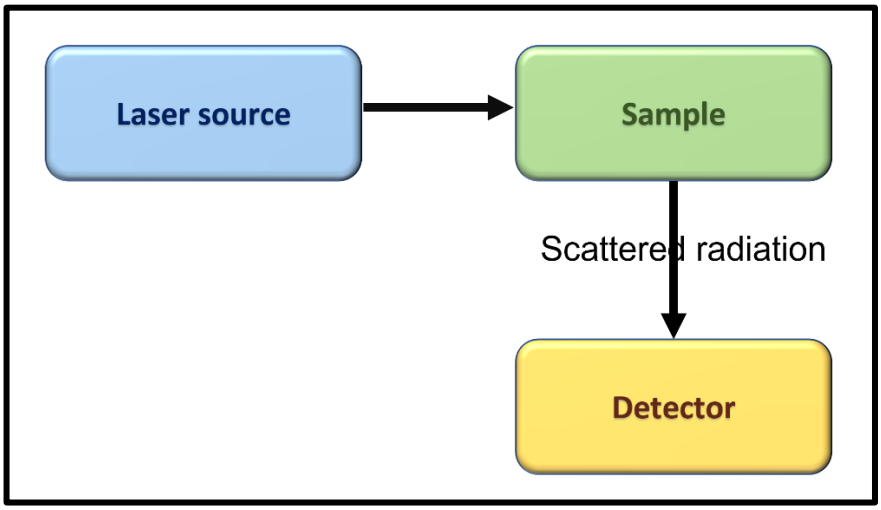

Figure 2.6 Basic set up of Raman spectrometer

The detector must be orthogonal to the direction of the incident radiation in order to only observe dispersed light. The source, which is frequently a laser, must provide intense monochromatic radiation. The prerequisites for a molecule to be Raman active are also different from those for other forms of spectroscopies, which called on a permanent magnetic dipole moment, at least for diatomic molecules. When a stream of energetic photons makes up a light wave. Two of the many things that can happen when a photon strikes a molecule are covered below:

Elastic, or Raleigh Scattering: This occurs when the photon merely "bounces" off the molecule without any energy transfer. In this manner, the great majority of photons will be scattered.

Inelastic, or Raman Scattering: This occurs when the photon and the molecule exchange energy, causing the emission of a subsequent photon with a frequency different from the incident photon. The photon may cause the molecule to either gain or lose energy. According to quantum mechanics, molecules can evolve to a higher energy, virtual state when photons interact with them. There could be a variety of effects from this greater energy level. One such result would be a photon with a different energy level being produced as the molecule relaxes to a vibrational energy level that is different from its initial condition. The Raman shift is the term used to describe the energy gap between the incident photon and the scattered photon. In addition to photons at the incident frequency of υ_0 (elastic or Rayleigh scattering), the weakly scattered radiation also contains photons at other frequencies, such as $\upsilon_0 \pm \upsilon_m$. The Stokes lines are the peaks at lower frequencies; the anti-Stokes lines, which are often much weaker than the Stokes Lines, are the peaks at higher frequencies. Only the Stokes spectrum is typically recorded because the same frequencies are present in every set of lines.

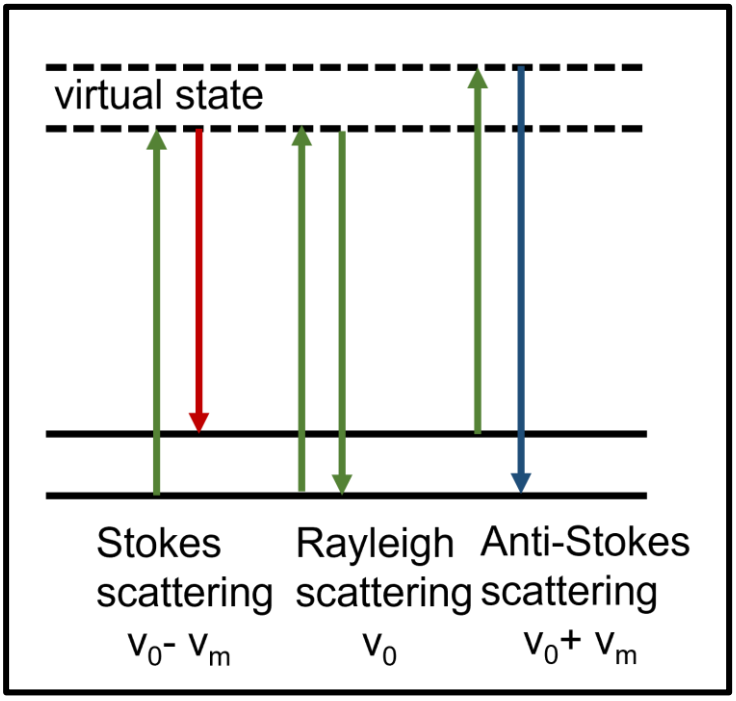

Figure 2.7 Scattering phenomenon in Raman spectroscopy.

Instrumentation: The market for spectroscopy now offers a wide variety of Raman instruments, from very big systems to miniaturized ones that operate in various spectral

bands, as a result of the tremendous technological advancements over the past years. Choosing which Raman instruments and circumstances to employ for various types of samples or studies is frequently a challenge for non-expert Raman users. A laser source, an optical system to illuminate the sample and gather the Raman signal, a "dispersive" system, and a detector are the four essential components of a Raman spectrometer. A laser acts as the excitation source to cause the Raman scattering and is one of the fundamental parts that make up a contemporary, compact Raman spectrometer. Modern Raman equipment often employ solid state lasers with common wavelengths of 532 nm, 785 nm, 830 nm, and 1064 nm. Although the signal produced by shorter wavelength lasers is stronger due to their higher Raman scattering cross-sections, shorter wavelength lasers also have a higher incidence of fluorescence. Because of this, the 785 nm laser is a common component in Raman systems. Fiber optic cables are used to both send and receive the laser energy from the sample. Rayleigh and anti-Stokes scattering are removed with a notch or edge filter, and the light that is still scattered by Stokes is then sent to a dispersion element, usually a holographic grating. The light is captured by a CCD detector, which produces the Raman spectrum. It is crucial that high-quality, optically well-matched components are utilised in the Raman spectrometer since Raman scattering produces a weak signal [89], [91].

Although Raman spectroscopy is an effective method, it has several drawbacks. The Raman effect's own power is one of these restrictions. The majority of light scattering from a substance will be Rayleigh scattering. Raman spectroscopy's ability to detect Raman scattered light is dependent on this, which limits its sensitivity. Increasing the laser's power is a simple workaround, although it has the disadvantage of perhaps harming the sample. Fluorescence is a significant obstacle to Raman spectroscopy. Fluorescence happens when a substance absorbs light and then releases lower-energy light at a later time and this is in contrast to Raman scattering [94].

2.3.3 Field emission scanning electron microscope (FESEM)

It is not a viable alternative to observe particles in the nano regime using optical microscopy since the resolution is constrained by the wavelength of light. Since electrons have a far shorter wavelength than photons do, they can be used in electron microscopes to observe materials at the atomic level. The wavelength of electrons, which has the property of being

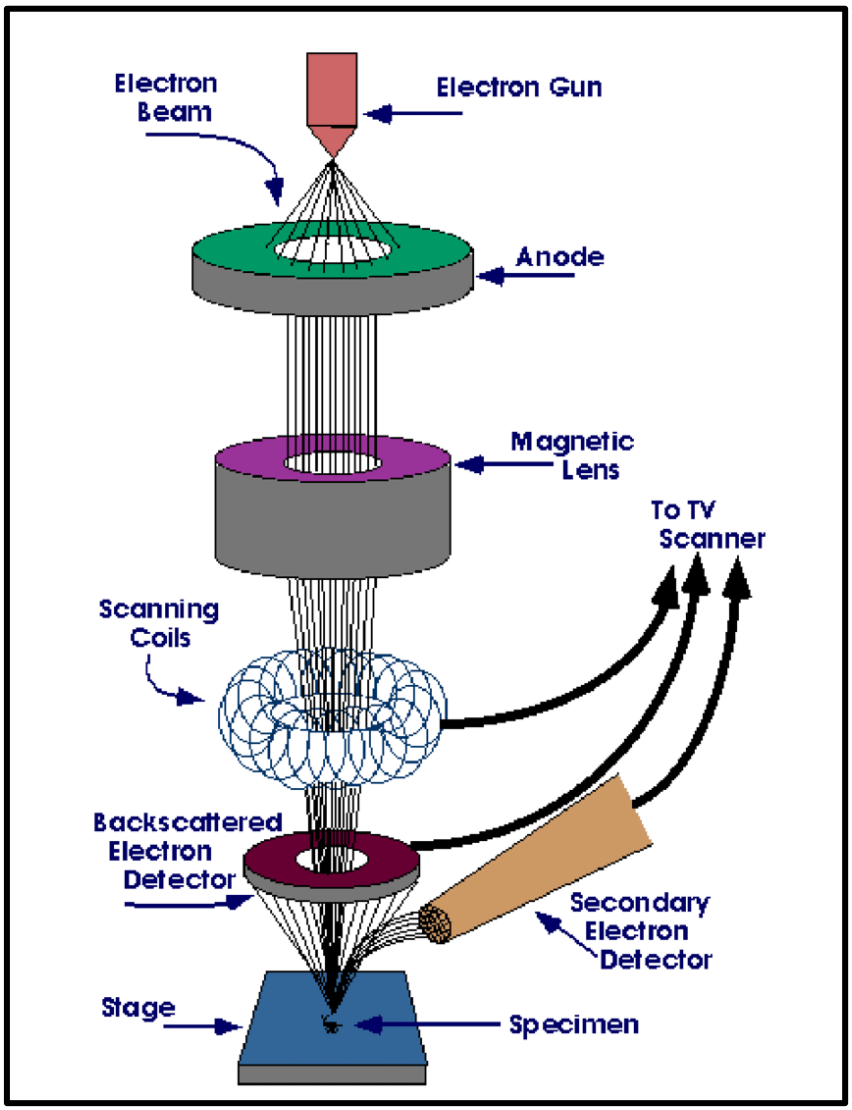

Figure 2.8 Schematic Diagram of field emission scanning electron microscope [69]

inversely proportional to the electron momentum, is said to have a dual nature of particle waves in accordance with quantum mechanics. The electron beam will therefore have a shorter wavelength and be able to transmit information in the nanometer range if we use electron beams that accelerate under high voltage. Techniques for electron microscopy employ this idea [95]. Like a standard SEM, FESEM operates by scanning the sample surface with an electron beam while a monitor shows the relevant data based on the available detectors. The electron generation technology is where a FESEM and a SEM diverge most. The FESEM uses a field emission gun as its electron source, producing intensely focused high and low energy electron beams that greatly enhance spatial resolution and allow work to be done at very low potentials (0.02-5kv). This reduces the effect of charging on non-

conductive specimens and prevents damage to samples that are sensitive to electron beams. The employment of in-lens detectors by FESEM is yet another incredibly noteworthy aspect [96]. In SEM a tungsten tip is covered in a layer of zirconium oxide, which has the peculiar virtue of enhancing electrical conductivity at high temperatures, to create Schottky emitters. A field emission gun is used in electron microscopes to create an electron beam that is more coherent, smaller in diameter, and up to three orders of magnitude brighter than those produced by conventional thermionic emitters like tungsten or filaments with lanthanum hexaboride (LaB6) tips. In comparison to thermionic devices, the outcome is a much-enhanced signal-to-noise ratio, spatial resolution, and emitter life. This is true for both scanning and transmission electron microscopy.

Working: A field emission source releases electrons, and they are then accelerated in a strong electrical field gradient. These so-called primary electrons are focused by electronic lenses within the high vacuum column to create a narrow scan beam that bombards the target. As a result, the object's each spot emits secondary electrons. The surface structure of the item is related to the angle and speed of these secondary electrons. The secondary electrons are captured by a detector, which then generates an electrical signal. A video scan image that can be viewed on a monitor or a digital image that can be recorded and processed further are created from this signal once it has been amplified.

Preparation: The first step in preparing an object for SEM observation is to make it current conductive. They are covered in an incredibly thin layer of gold or gold palladium (between 1.5 and 3.0 nm) to achieve this. Additionally, objects need to be able to withstand the high vacuum and shouldn't change it by losing gas or water molecules, for example. Then, coating is carried out in a different apparatus.

Source of electrons: In conventional electron microscopes, the majority of the electrons are produced by electrically heating a tungsten filament to a temperature of about 2800 °C. No heating is used in a field emission scanning electron microscope instead a so-called "cold" source. In front of a primary and secondary anode, a tungsten needle with a tip diameter of 10-7 m or 10-8 m serves as the cathode. The magnitude of the voltage between the cathode and the anode ranges from 0.5 to 30 KV. The image quality is noticeably improved since the electron beam created by the FE source is around 1000 times smaller than that of a

conventional microscope. Since field emission requires a severe vacuum (10-8 Torr) in the microscope's column, there is a device that periodically cleans the electron source with a current flash. A FE tip can theoretically last a lifetime, unlike a traditional tungsten filament, providing the vacuum is kept steady.

Column with lenses and apertures: The electro-magnetic lenses (condenser lens, scan coils, stigmator coils, and objective lens) and the column's apertures focus the electron beam to a pinpoint sharp spot.

Object chamber: The item is mounted on a unique holder after being covered in a conductive coating (see preparation). The item is positioned on a movable stage and inserted through an exchange chamber into the high vacuum area of the microscope. By using the arrows in the POSITION box, you can move an object horizontally and vertically on the screen in the virtual FESEM. The object in the chamber of a real microscope can be moved using a joystick that steers in the left-right axis, forward, and backward. Additionally, the object can be rotated, moved in the Z direction (i.e., closer or further away from the objective lens. In the chamber, the "secondary electron emission" detector (scintillator) is situated behind the object holder.

Image formation: The levels and angles at the object's surface influence the velocity at which secondary electrons are emitted from the object surface when the primary probe bombards it. The scintillator (fluorescing mirror), which creates photons, is struck by secondary electrons drawn in by the Corona. The characteristics of the secondary electrons determine where and how strongly the mirror is illuminated. In time with the electron beams scan movement, the scintillator signal is amplified and converted to a video signal that is sent to a cathode ray tube. The structure of the object's surface is reflected in the contrast of real time' image that displays on the screen. A digital image is created in parallel with the analogue image, which can then be processed [96], [97].

2.3.4 Energy Dispersive X-Ray spectroscopy (EDX)

One can shorten it to EDS, EDX, EDXS, or XEDS. Energy dispersive X-ray microanalysis (EDXMA) or energy dispersive X-ray analysis (EDXA) are other names for it. It is an investigation technique that is frequently used to characterize objects' chemical or elemental

makeup. The sample might be in any form, including liquid, solid thin films, solid powder, and pellets, among others. The usual EDS setup is comparable to the SEM setup. EDS is actually incorporated within the SEM setup, to be more precise. Similar to SEM, the operation of EDS depends on electron focusing. The element is identified and the sample material's composition is measured using the energy dispersive x-ray method. A spectrum is produced by the EDX analysis. An x-ray's frequency for each energy level is plotted on the EDX spectrum. When the most x-rays were received, the energy levels that are represented by peaks in an EDX spectrum. Typically, an element is the only one with these peaks. Higher peaks in the spectrum denote an element's presence at higher concentrations. Utilizing specialized computer software, overlapping peaks from mixtures are deconvolved [98]. In contrast to X-ray beam excitation, which is used in X-ray fluorescence (XRF) spectrometers, electron beam excitation is used in scanning transmission electron microscopes (STEM) and SEM. X-rays are converted into voltage signals via a detector, which feed a pulse processor, which measures the signals and sends them to a data analyzer for analysis and display. Liquid nitrogen is frequently used to cool Si (Li) detectors at cryogenic temperatures, and some contemporary systems also have silicon drift detectors (SDD) that use Peltier cooling devices.

An object must be struck by either a very energetic beam of charge carriers (electrons or protons) or X-rays in order for it to emit characteristic X-rays. The sample's atoms have bonded ground state electrons (unexcited) at specific energy levels or electron shells. An incoming beam may excite an electron from an inner shell, knocking it out of its shell and creating a hole where the electron existed before the excitation. An electron from a higher-energy shell is capable of occupying this hole. An X-ray is produced due to the energy disparity between the higher and lower energy shells. Depending on which shell an electron is moving from to which shell, an electron transfer will release a certain amount of energy, measured in joules. An energy dispersive spectrometer can measure the energy and number of X-rays that are emitted from the specimen. Because the energies (wavelength) of these emitted X-rays are unique to the element from which they originate, they are referred to as characteristic X-rays. Thus, elemental analysis can be done using this method. The distinctive X-rays released by excited K-shell electrons are known as "K Lines," whereas those emitted by excited L and M shell electrons are known as "L Lines" and "M Lines,"

respectively. When an element is heavy, its characteristic X-ray energies are higher as well, necessitating the need for incident electrons with higher energies. The various peak positions with the relevant energies can be used to determine the sample's qualitative compositional information. The net count rates are necessary for the concentration computation, and a specimen's distinctive X-ray energy serves as a barometer for its atomic number [99], [100].

Because they can concurrently study an object's shape and elemental makeup, scanning electron microscopy with energy dispersive x-ray is a potent method for classifying and differentiating materials. The identification and classification of various material structures, the study of surface morphology, the detection of particle contamination, structural analysis, forensic examinations, the detection of corrosion and oxidation issues, and the identification of product and process failure are some of the typical applications of FESEM/EDS [98].

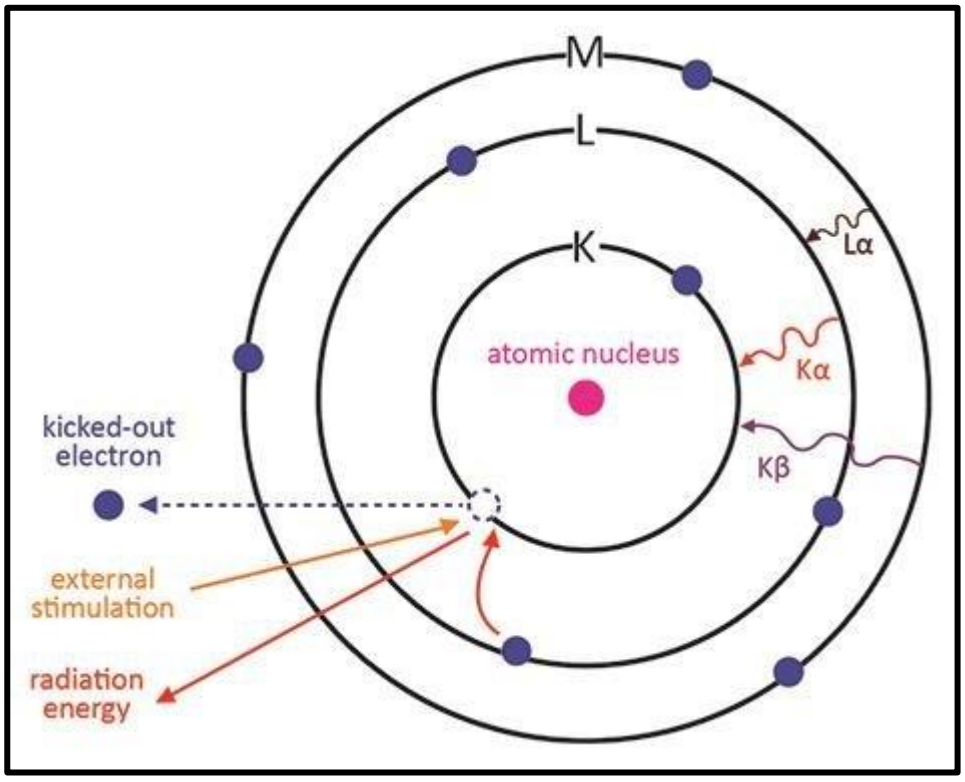

Figure 2.9 Principle of characteristic X-Rays generation in EDX [72].

2.3.5 UV-Vis - NIR spectrophotometry

An essential physical instrument that uses light in the ultraviolet, visible, and near infrared ranges of the electromagnetic spectrum is ultraviolet (UV) spectroscopy. A linear

relationship between absorbance, the concentration of absorbers (or absorbing species) in the solution, and the route length is established by the Beer-Lambert law. As a result, for a fixed path length, UV-Vis spectroscopy can be used to determine the concentration of the absorbing species [1]. This method is incredibly straightforward, adaptable, quick, precise, and economical. The UV-Vis-NIR Spectrophotometer is a tool used for ultraviolet-visible (or UV-Vis) spectroscopy. By utilizing radiative energy associated with the far and near ultraviolet (UV), visible (Vis), and near infrared (NIR) parts of the electromagnetic spectrum, this can be used to analyze liquids, gases, and solids. The following preset wavelengths have been established for these regions: UV: 300–400 nm; Vis: 400–765 nm; and NIR: 765–3200 nm [101], [102].

Principle: The wavelength of the light that reaches the detector after travelling through an object in a light beam is measured. Important details about chemical composition and molecular number are revealed by the measured wavelength (contained in the measured signal intensity). As a result, information that is both quantitative and qualitative can be acquired. The transmittance, absorbance, or reflectance of radiation in the range of 190 to 1100 nm can be used to gain information [2,3]. The promotion of electrons to excited states or the anti-bonding orbitals results from the absorption of incident energy. Photon energy must match the energy required by an electron to be promoted to the next higher energy state in order for this transfer to take place. The fundamental idea behind absorption spectroscopy is this technique.

Instrumentation: Light source (UV and visible), monochromator (wavelength selection), sample stage, and detector are the four fundamental parts of a spectrometer. Typically, a continuous tungsten filament spanning the UV spectrum is utilised as the light source. The typical detector is a photodiode or CCD. In order to filter light of a specific wavelength before it is supplied to the detector, photodiodes are used with monochromators. It is necessary to turn off the visible lamp while monitoring UV spectrum absorbance, and vice versa. A schematic UV-Vis-NIR spectrometer is shown in Figure 2.10.

- When deuterium or hydrogen is electrically excited at low pressures, a continuous UV spectrum is created. An excited molecular species is produced as part of the UV light generating process, and this species then splits into two atomic species and a

UV photon. Both deuterium and hydrogen lamps emit light with wavelengths between 190 and 375 nm.

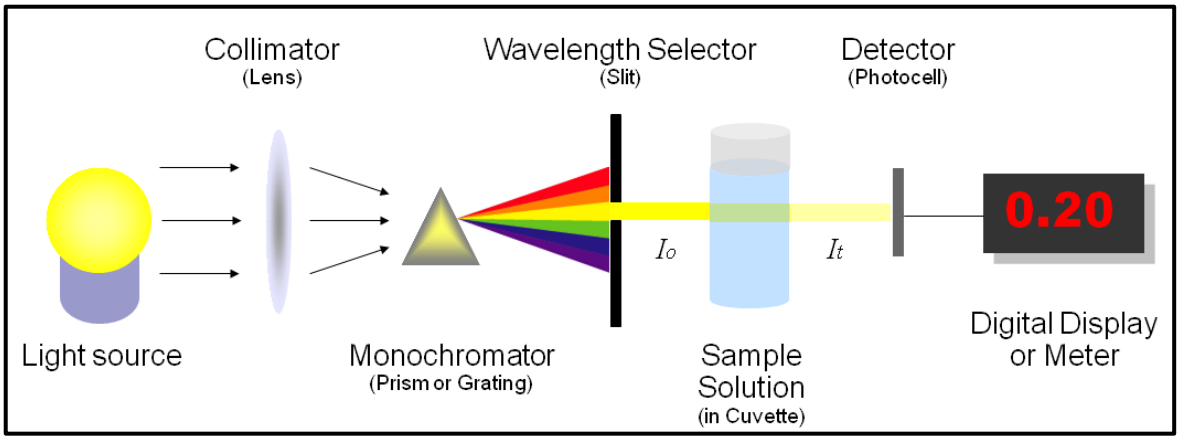

Figure 2.10 Schematic diagram of a UV-Vis - NIR spectrophotometry [75].

The visible light source is a tungsten filament bulb. This lamp has a wavelength range of 350 to 1100 nm. Energy output from a tungsten filament lamp is proportional to the operating voltage raised to the fourth power. Therefore, a highly stable voltage must be applied to the lamp in order to obtain stable emission. Transformers with constant voltage or electronic voltage regulators are used to maintain voltage stability.

- It uses a monochromator source, which is separated into two halves of equal intensity by a half-mirror splitter before it reaches the sample. One component (or sample beam) moves through the cuvette containing the material to be analyzed in a solution in a clear solvent. Another beam, known as the reference beam, travels through a cuvette that contains only solvent. Containers for reference and sample solutions must be transparent to the passing beam.
- A detector measures the amount of light that cuvettes emit, and it communicates this information to a meter so that it can record and show the values. The intensities of light beams are calculated and compared by electronic detectors. A number of UV-Vis spectrophotometers feature two detectors, a phototube and a photomultiplier tube, and simultaneously monitor the reference and sample beams. In UV-Vis equipment, the photomultiplier tube is the detector that is most frequently utilised. It consists of an anode, many dynodes, and a photo emissive cathode that emits

electrons when photons touch it. Dynodes also emit several electrons when a single electron strikes them. Amplification and measurement are done on the generated current. Photomultipliers have quick response times and are extremely sensitive to UV and visible radiation. However, because high power light may harm photomultipliers, they are only used in low power radiation.

Classification: The single monochromator type and the double monochromator type of UV-VIS Spectrophotometers are both available. The single monochromator type and the double monochromator type are indicated by their names by having one and double monochromator respectively.

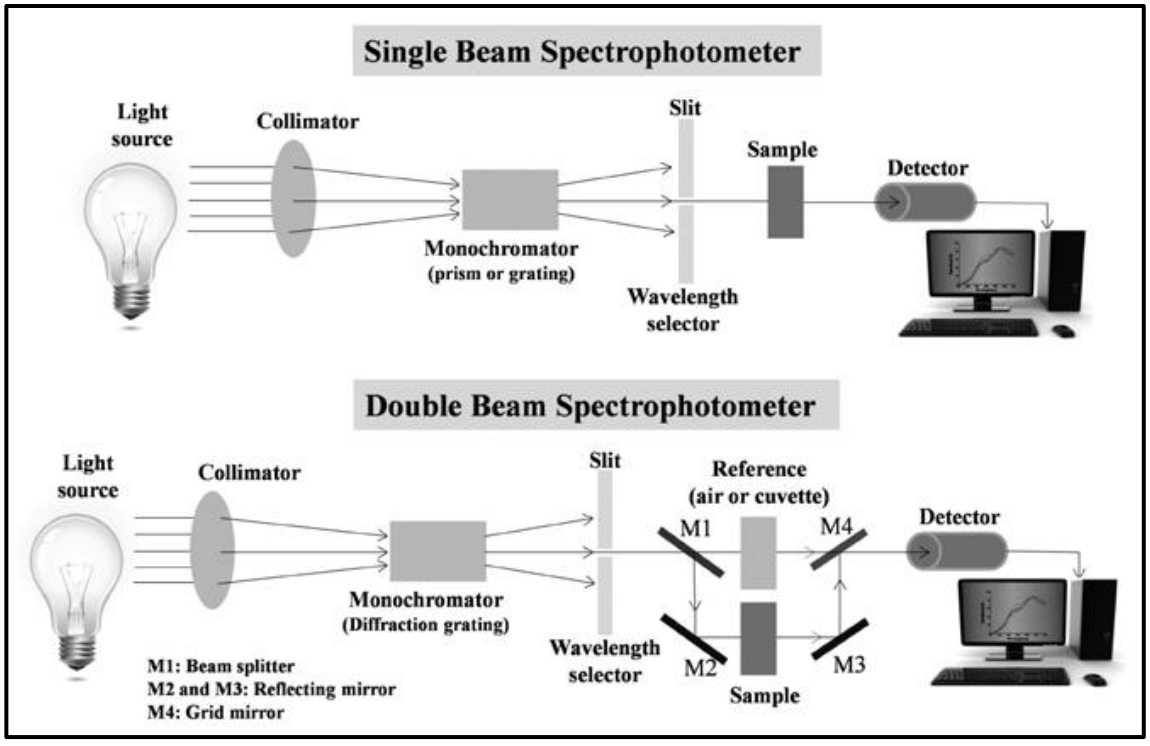

Figure 2.11 Schematic diagram of single and double beam spectrophotometer [76]

Tauc Plot: An essential optical metric that specifies the photon energy needed to excite an electron from the valence band to the conduction band is the optical bandgap energy (Eg) of a semiconductor. The Eg is a crucial aspect of nanomaterials' electronic structures, and it ultimately affects how they could be used in devices in various industries. For determining optical Eg, UV-vis spectroscopy measurement is most frequently used. Although methods like photothermal spectroscopy and spectroscopic ellipsometry exhibit more accuracy, UV-vis spectrometers are generally accessible and simple to use [103]. An ideal direct band gap

semiconductor's UV-vis spectrum shows essentially little absorption for photon energy below the band gap and a significant increase for photon energies above the band gap. Since this reveals the bare minimum of energy needed for a photon to excite an electron across the band gap and be absorbed in the semiconductor material, the band gap in the absorption spectrum corresponds to the point at which absorption begins to increase from the baseline. The local density of states at the valence band maximum and conduction band minimum, as well as excitonic effects, are reflected in the nonlinear increase in absorption that is seen in real spectra. For values of absorption coefficient (α) > 10^4 cm^{-1} frequently follow the relationship below, which was proposed by Tauc and provided by Davis and Mott. According to equation 2.3 it is presumable that a semiconductor's optical absorption coefficient is energy (hν) dependent.

$$(\alpha h\nu)^{1/n} = B\,(h\nu - E_g) \tag{2.3}$$

Where h is Planck's constant, α is absorption coefficient, B is a constant, E_g optical band gap of material and n is a factor that depends on the electronic transitions with values of 1/2, 3/2, 2, and 3, which, respectively, correspond to direct (allowed), direct (forbidden), indirect (allowed), and indirect (forbidden) transitions. When extrapolated to the baseline, these so-called Tauc plots of $(\alpha h\nu)^{1/n}$ vs. hν provide the band gap value. Instead of absorption coefficient, the data from the UV-Vis NIR spectrometer comprises absorbance. As a result, the following relationship is used to determine the absorption coefficient (α) from the absorbance (A).

$$\alpha = 2.303A/t \tag{2.4}$$

where t is the sample's thickness. A distinct linear regime that marks the beginning of absorption may be seen in the resulting tauc graphic. A straight line is used to suit this area, and the bandgap value is given by the x intercept. [101].

2.3.6 Source measuring unit

An instrument that combines a sourcing function with a measurement function on the same pin or connector is known as a source measure unit (SMU). It has the ability to source voltage or current while also measuring voltage and/or current. It combines into a single, precisely

timed instrument the functions of a power supply or function generator, a digital multimeter (DMM) or oscilloscope, a current source, and an electronic load A Source Meter instrument has several benefits over standalone instruments due to their close coupling. Saving costly rack space and streamlining the remote programming interface are both benefits of being able to fit a source and a meter in a single half-rack enclosure.

The Source Measure Unit (SMU) Instruments from Keithley's Series 2400 are made specifically for test applications that require tightly connected sourcing and measurement. All Source Meter versions include measurement capabilities as well as precision voltage and current sources. Each Source Meter SMU instrument is a real instrument-grade 612-digit multimeter as well as a highly stable DC power source. Low noise, readback, and precision are some of the properties of the power source. High repeatability and minimal noise are two of the qualities of the multimeter. A small, single-channel DC parametric tester is the end result. These devices can function as voltage sources, current sources, voltage meters, current meters, and ohmmeters when in use. The source Meter SMU instruments are incredibly useful for a wide range of characterization and production test applications, which will be of great value to manufacturers of components and modules for the communications, semiconductor, computer, automotive, and medical industries.

Figure 2.12 Keithley 2400 source measuring unit [77].

Engineers are exploring for ways to create solar cells that are more affordable and efficient in research labs. A small-scale test device is created, its performance is characterized to determine how well a solar cell is functioning. Although these test cells are too small to

produce any useful power beyond, say, lighting a single LED, they are big enough to describe the fundamental operating range and efficiency [104].

Chapter 3

Effect of pH on SnS and CdS thin films

3.1 Introduction

Numerous writers have claimed that the structural, optical, morphological, and chemical characteristics of the various constituent layers have an impact on the efficiency of thin film solar cells [105]. Various factors can be varied to optimize the properties of SnS and CdS thin film which includes annealing temperature [3], [55], [106], [107], bath composition [108], [109], deposition time [59], [110] and pH of the bath solution [34], [111], [112]. T. Ben. Nasr et al. [113] proposed that the physical properties of the ZnS thin film can be modified, and V. S. Raut et al. [112] investigated the impact of the pH of the bath solution on the structural, optical, and morphological properties of CdSe thin films. In this work, SnS and CdS thin films were prepared chemically, and the influence of pH on their properties was investigated. SnS/CdS heterojunctions were fabricated by taking different combinations of films. The performance of the cells was also evaluated.

3.2 Experimental details

3.2.1 Preparation of SnS thin films

In this work, stannous chloride ($SnCl_2.2H_2O$) and thioacetamide (CH_3CSNH_2) were used as tin and sulphur precursors, respectively, to prepare SnS thin films. As complexing agents, triethanolamine $N(CH_2CH_2OH)_3$ (TEA), and trisodium citrate $Na_3C_6H_5O_7.2H_2O$ (TSC), were used to avoid sudden precipitation. All the chemicals used in this work were of analytical grade and were purchased from Merck. The molarity formula was used to obtain the required amount of weight of the reagents.

$$\text{Weight(gm)} = \text{Molarity(M)}*\text{volume(L)}*\text{molar mass (mol/gm)}$$

Digital weighing machine was used to measure accurately the amount of chemicals. Firstly, 0.3 M $SnCl_2.2H_2O$ dissolved in glacial acetic acid was added to 5 ml of 0.6 M trisodium

citrate, which was followed by the sequential addition of 5 ml of TEA and 5 ml of 0.1 M thioacetamide. To adjust the pH of the bath solution, Sp. gr. .91 pure ammonia solution was added. The chemicals used and their role is represented in figure 3.1.

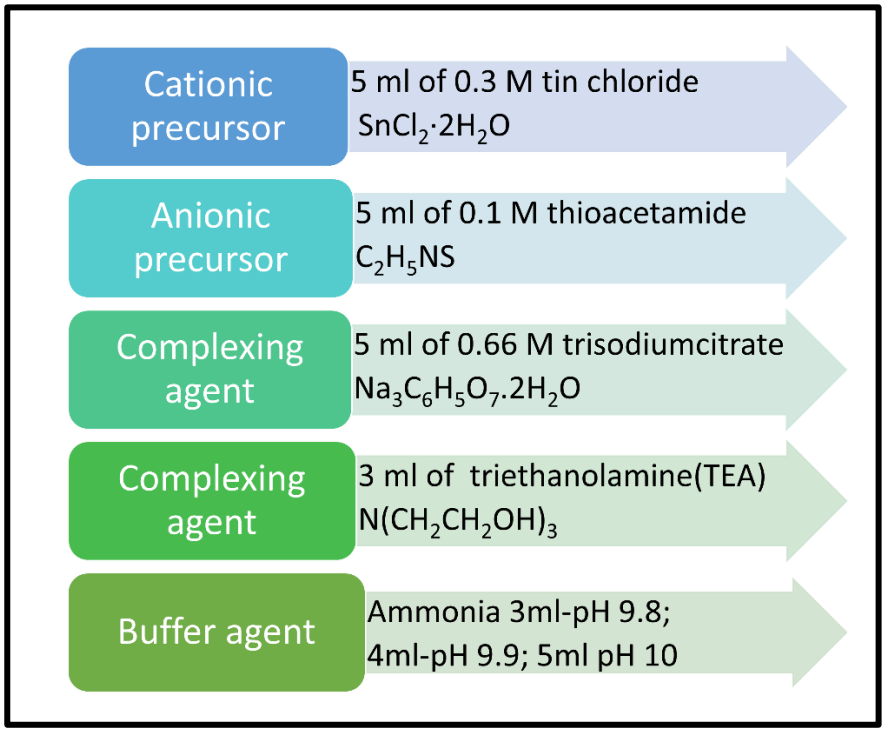

Figure 3.1 Chemicals used for the preparation of SnS thin films

After the addition of the required amount of ammonia, the final solution was made up to 100 mL by the addition of deionized water, and thoroughly cleaned glass substrates were immersed in it. The clear solution was gradually changed to yellow, which eventually turned chocolate brown. The dark brown SnS thin film was obtained at room temperature. For varying the pH, ammonia solution was added in amounts of 3 ml, 4 ml, and 5 ml, and the pH values obtained were 9.8, 9.9, and 10, respectively. The deposition time decreased considerably with the increase in pH. The film formation was completed within 12 hours, 10 hours, and 9 hours for the pH values of 9.8, 9.9, and 10. It was observed that when the pH of the source solution was below 9.8, film formation did not take place even after 48 hours at room temperature. For solutions with a pH value greater than 10, the chemical reaction took place at a faster rate in the ambient conditions, and the film was not formed. The films were prepared by varying the pH between 9.8 and 10. The films that were obtained had a dark brown colour. The films were annealed at 60 °C for 30 minutes, and the

characterizations were done. The steps involved in the preparation are schematically represented in figure 3.2.

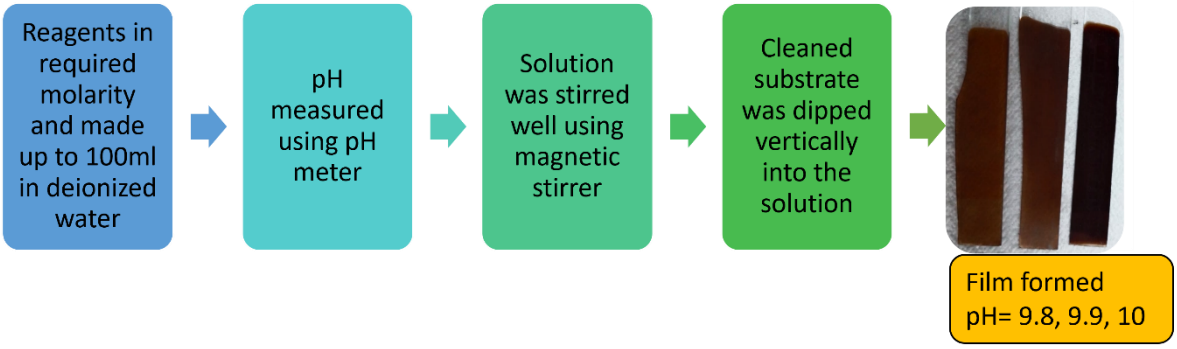

Figure 3.2 Method of preparation of SnS thin films.

3.2.2 Preparation of CdS thin films

For the preparation of the cell CdS thin film is chosen as it shows n-type conductivity and have a wide bandgap (2-3 eV) which is apt for the window layers. CdS thin films were prepared from a chemical bath containing 0.1 M cadmium acetate ($(CH3COO)_2Cd.2H_2O$) as a cationic precursor, 0.3 M thiourea as an anionic precursor, triethanolamine (TEA) as a complexing agent, and ammonia as buffer solution [56]. The chemicals used are shown in figure 3.4.

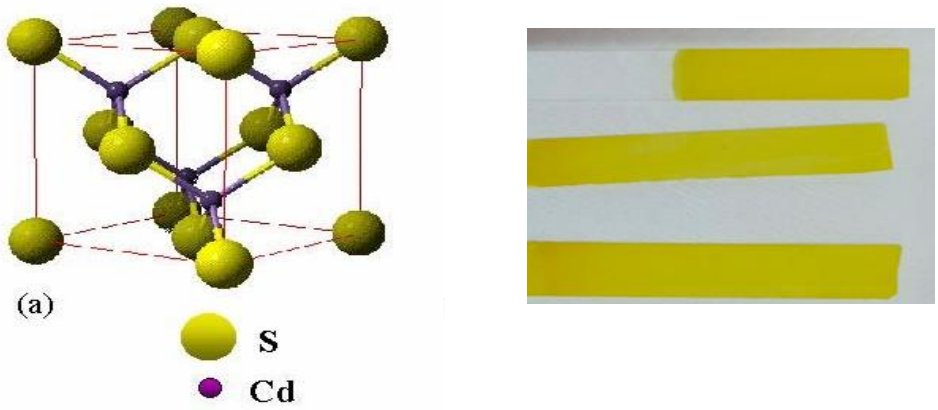

Figure 3.3 Cubic structure of CdS and the prepared CdS thin film

Three different bath solutions with pH values of 11.3, 11.4, and 11.5 were used to make the films. The films were not formed for pH values outside this range at ambient conditions. The deposition times for pH values 11.3, 11.4, and 11.5 were respectively 5 hours, 4 hours, and 2 hours. The prepared CdS thin films were yellow in colour and were homogeneous, smooth, and adherent to the substrate. The samples were annealed at 60 °C for 30 minutes and characterized using various techniques. The prepared CdS films and the cubic structure of CdS is shown in figure 3.3.

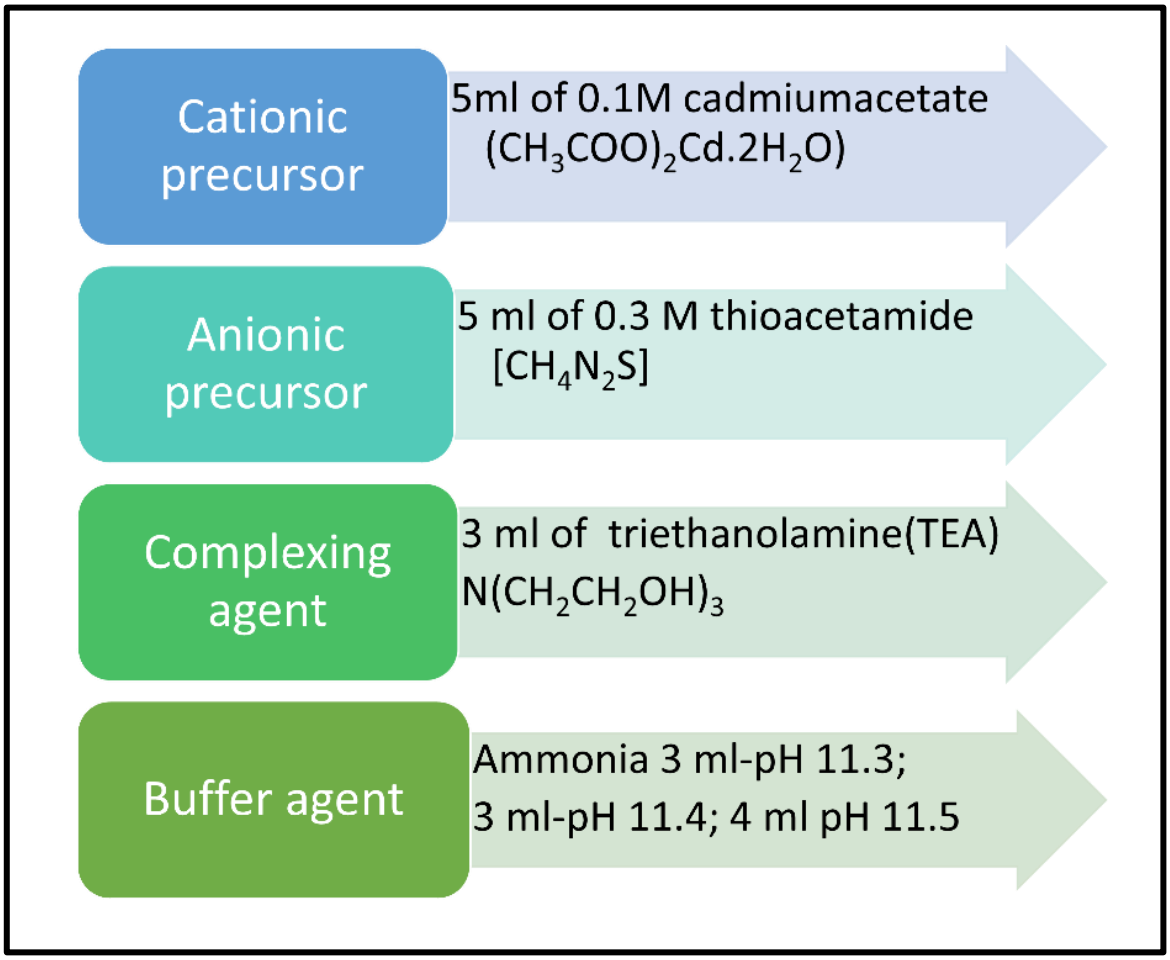

Figure 3.4 Chemicals used for the preparation of CdS thin films

3.2.3 Fabrication of SnS/CdS heterojunction

The heterojunction was formed on a thoroughly cleaned ITO substrate. Firstly, the SnS thin film was coated and annealed as mentioned before, followed by the deposition of CdS. The

whole structure was then annealed at 60 °C for 30 minutes. A thin silver contact was drawn above the heterojunction using silver paste. The junction was fabricated by choosing different thin films of SnS and CdS prepared from varying pH of the source solutions, as mentioned earlier, and the I-V characteristics were studied using a Keithley source meter. The cell structure is shown in figure 3.5.

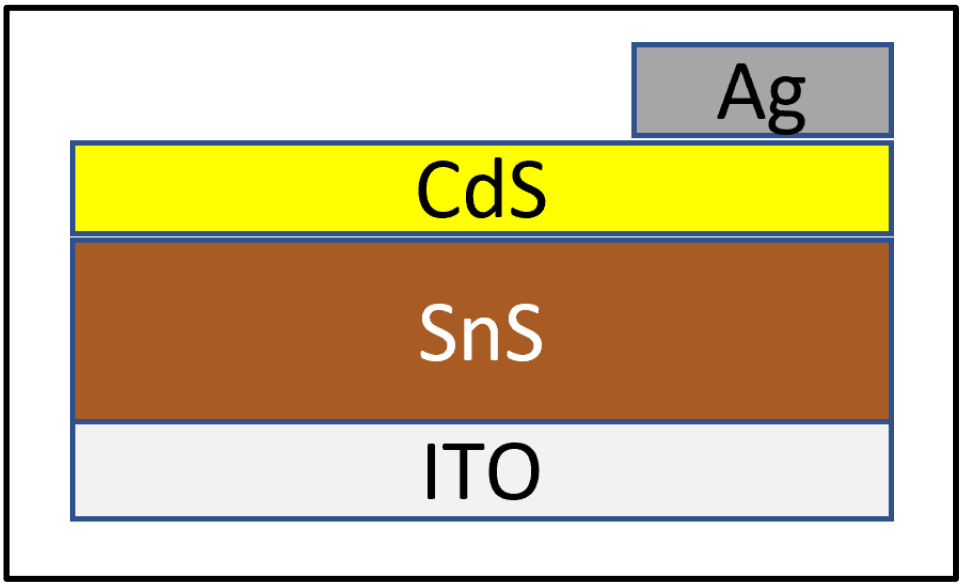

Figure 3.5 Structure of the SnS based solar cell

3.3 Results and discussion

Structural studies of SnS thin films were performed using the Bruker D8 Advance X-ray diffractometer (Cu Kα source). Raman analysis was done using a Horiba Labram HR Evo Raman spectrometer. The annealed films were optically characterized using an Intek UV-vis spectrophotometer. The wavelength used for the characterization was in the range of 190 nm to 1190 nm. Deuterium was used as the source for UV and Tungsten for visible radiation. The morphology of the films was studied using a field emission scanning electron microscope (FESEM SUPRA 55 VP-4132 Carl Zeiss). Energy dispersive spectra (EDS) were recorded along with FESEM to get a better understanding of the chemical composition.

3.3.1 Reaction mechanism

The four processes-the simple ion-ion mechanism, simple hydroxide cluster mechanism, the complicated ion-by-ion decomposition mechanism, and the complex cluster decomposition

mechanism are active during nucleation and film growth in CBD. Ions diffuse over to the substrate in the initial phase of the straightforward ion-ion reaction. The substrate promotes nucleation by acting as a catalyst. As ions in the solution are absorbed, nucleation expands and new crystals are formed. Crystals come together to form a film that uses Van der Waals forces to bind to one another. Hydroxide colloidal particles diffuse to the substrate and adhere there in a straightforward hydroxide colloidal mechanism. Free ions interact with hydroxide colloidal particles that are attached to the substrate. The free ion displaces the hydroxide as a result of this reaction. The first particles produced by reaction stick together to form an aggregated film. In last two processes, the initial ions diffuse to the substrate to generate heterogen nuclei that develop or exist as complexed nuclei colloids in the solution. In the intricate breakdown procedure, first nucleation is exposed to chemical interactions to create a film. To get a high-quality film from CBD, it is necessary to ensure that the reaction in the solution is realized gradually. Metal ions can form a complex with a ligand to stop the solid chemical from precipitating quickly. This reaction suggests that film generation can happen via complex mechanisms in addition to simple ion-by-ion or cluster methods. On the basis of all this knowledge about the procedure, it has been assumed that the mechanism below is effective in the creation of SnS thin films on a substrate [57]:

$$[Sn(TEA)]^{2+}+CH_3CSNH_2+2OH^- \rightarrow SnS+TEA+CH_3CONH_2+H_2O$$

During the initial stages of deposition, Sn^{2+} ions formed bonds with the triethanolamine (TEA) ligand to form Sn [TEA]. This complex served to prevent the precipitation of undesirable materials like $[Sn(OH)_2]$, and at a later stage, the complex broke down to form bonds with sulphur ions, forming SnS compound. Trisodium citrate (TSC) can be substituted for TEA in a similar calculation[40]. When the pH increases, the $[Sn(TEA)]^{2+}$ complex releases more Sn^{2+} ions. As SnS precipitates more quickly in more basic solutions, results in speedy SnS deposition with increasing ammonia concentration[34]. The same reaction mechanism is applicable to the formation of Cadmium sulphide[109].

3.3.2 Structural properties

The X-ray diffraction patterns of the prepared samples of SnS (pH: 9.8, 9.9, and 10), and CdS (pH: 11.3, 11.4, and 11.5) with various pH values were displayed in figures 3.6 (a) and

(b), respectively. In SnS thin films, an intense peak was observed at 2θ value of 31.6°, which corresponds to the diffraction from the (0 1 3) plane, while the other peaks determined at 30.5° and 44.8° were indexed with the (1 1 0) and (0 2 2) planes, respectively. All the peaks were indexed and compared with the standard ICDD data card of SnS (ICDD file no. 001-0984), and the crystal structure was found to be orthorhombic. The intense peak observed for CdS thin films was at 51.8°, associated with the (3 1 1) plane of cubic CdS. The miller planes (1 1 1) and (2 0 0) correspond to the minor peaks at 26.7° and 30.9°, respectively. The peaks from the XRD pattern were indexed using the cubic CdS standard card (ICDD file no. 065-2877). Figure 3.7 shows the variation of intensity of the different peaks of SnS and CdS thin films. It was found that the intensity of the XRD peaks increased with the pH value of the bath solution for both SnS and CdS films.

3.3.2.1 Williamson–Hall method

The literature contains numerous techniques for calculating crystallite size and lattice strain. Williamson and Hall is the approach that is most frequently applied among those strategies. This means that the line broadening caused by strain and particle size is independent of one another and has a Cauchy-like profile; the observed line width is just the sum of the breadth caused by lattice strain and crystallite size [114]. The Williamson-Hall plots were drawn to determine the crystallite size and strain of the films. The width of the XRD peaks was due to two reasons, one from the crystallite size and the other from lattice strain broadening. The broadening is measured in terms of full width at the half maximum (β).

$$\beta_{total} = \beta_{crystallite\ size} + \beta_{micro\ strain} \tag{3.1}$$

The Scherrer equation can be used to calculate the crystallite size broadening while the other uses the strain equation.

$$\beta_{total} = \frac{k\lambda}{D\ cos\theta} + 4\varepsilon\ tan\theta \tag{3.2}$$

In the equation (3.2), k is the shape factor of the value 0.9, λ is the wavelength of the x-ray, which is 1.5406 Å, D is the crystallite size, θ is the Bragg angle, and ε is the micro strain of the lattice. A straight-line equation can be obtained by rearranging this equation.

$$\beta_{total} = \frac{k\lambda}{D\ cos\theta} + 4\varepsilon \frac{sin\theta}{cos\theta} \quad (3.3)$$

$$\beta_{total} cos\theta = \varepsilon\ 4sin\theta + \frac{k\lambda}{D} \quad (3.4)$$

Now equation (3.4) is in the form of the straight-line equation y = mx + c, where m and c are the slope and intercept, respectively. A straight line with microstrain (ε) as the slope and kλ/D as the intercept can be obtained by drawing a graph with 4sinθ on the x-axis and β_{total}cosθ on the y-axis [30,31]. As long as the values of k and are known, the crystallite size can be calculated from the intercept.

Figures 3.8 and 3.9 show the Williamson-Hall plots of samples prepared from different bath solutions with varying pH values for SnS and CdS thin films, respectively. As by equation (3.4), the microstrain and the crystallite size were obtained from the slope and the intercept of the straight line that was linearly fitted to the obtained points. The crystallite size was found to be 19.3 nm, 33.9 nm, and 37.2 nm for the pH values of 9.8, 9.9, and 10 for SnS thin films, respectively. For CdS thin films, it was found to be 15.2 nm, 16.2 nm, and 19.47 nm for the pH values of 11.3, 11.4, and 11.5. Figure 3.10 shows the variation the crystallite size with the pH values of the bath solution. It was observed that as the pH increased, the crystallite size increased, which in turn enhanced crystallinity. Moreover, as pH rises, OH- ions from the ammonia solution increase, which causes more cations to get into the solution, making the thin film more homogeneous and crystalline.

The slope of the fitted line gives the micro strain, and it was found to have positive values showing lattice expansion. The internal stress during the formation of the thin film causes a change in the crystallization, and this deformation is termed as microstrain. The microstrain values were 0.00226, 0.00384, and 0.00443 for the pH values of the bath solution, which were 9.8, 9.9, and 10 for SnS thin films, respectively. Figure 3.11 (a) shows the variation of the lattice stain of the SnS thin films with the pH of the bath solution. This is because, as mentioned above, as pH increases, more tin ions get into the solution and make the film denser, which is consistent with the FESEM images. This increase in density increases the strain in the lattice.

Effect of pH on SnS and CdS thin films

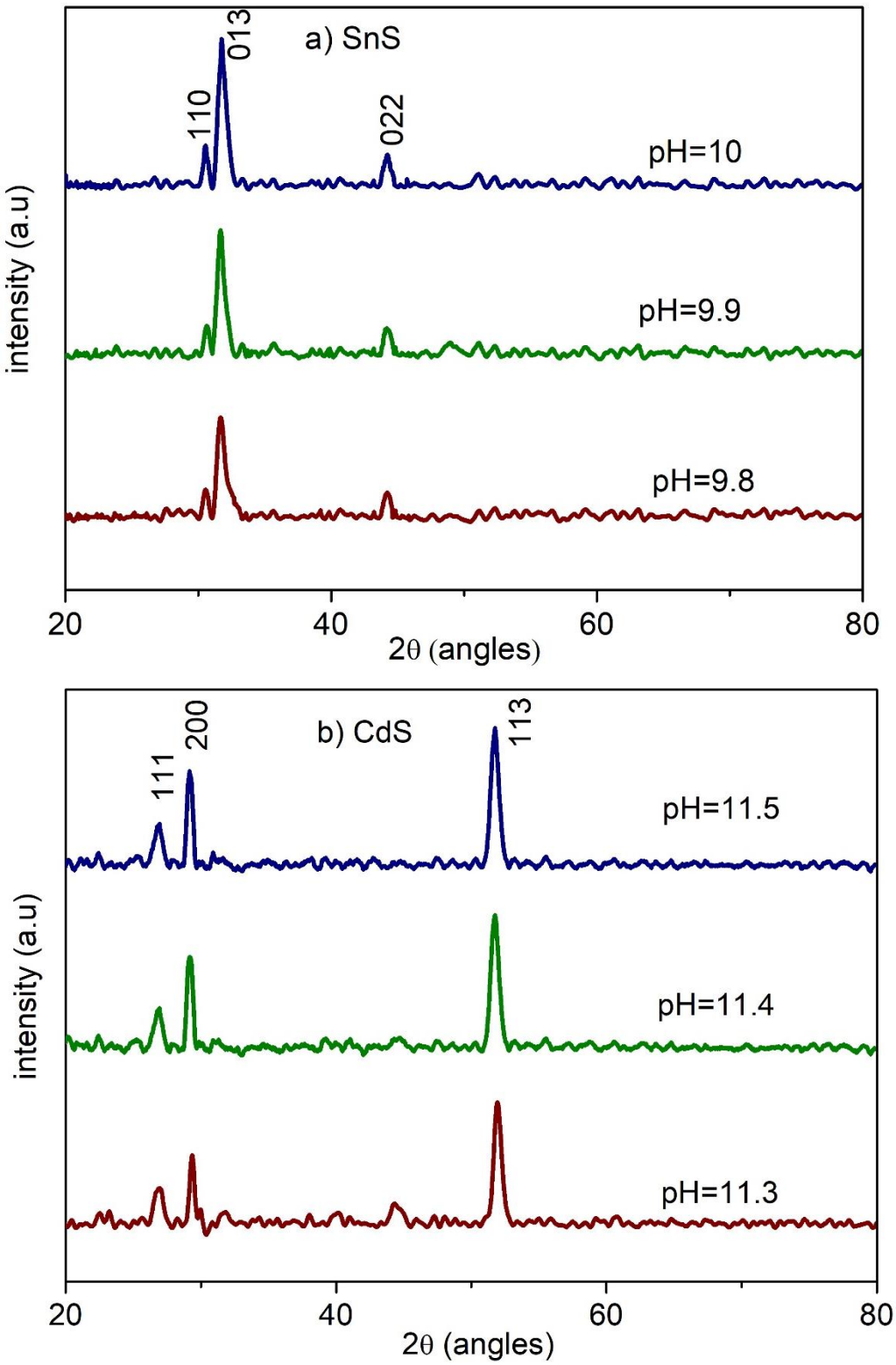

Figure 3.6 X-ray diffraction pattern of (a) SnS and (b) CdS thin films for different pH of the bath solution.

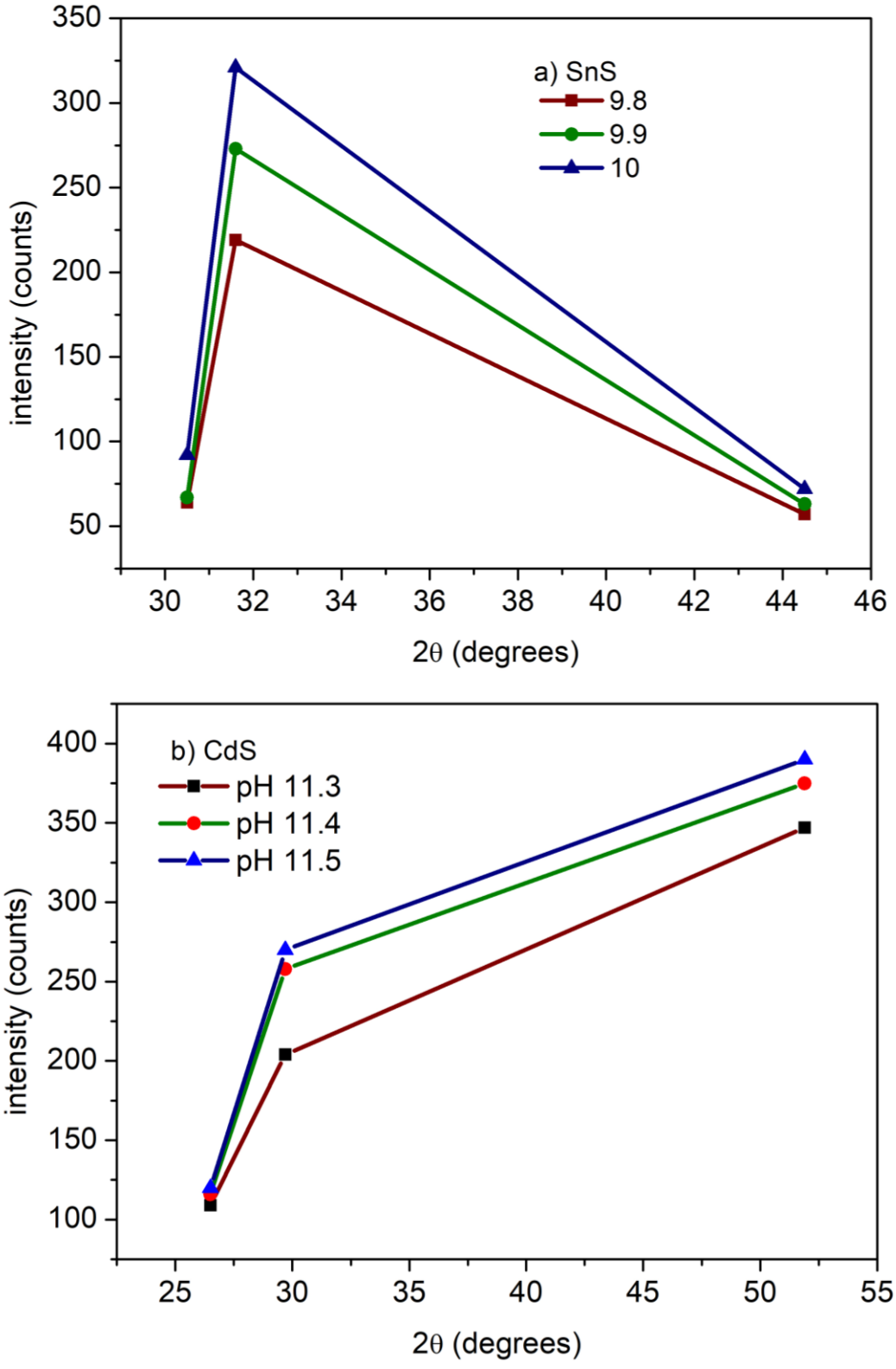

Figure 3.7 Intensity variation of XRD peaks with pH (a) SnS and (b) CdS

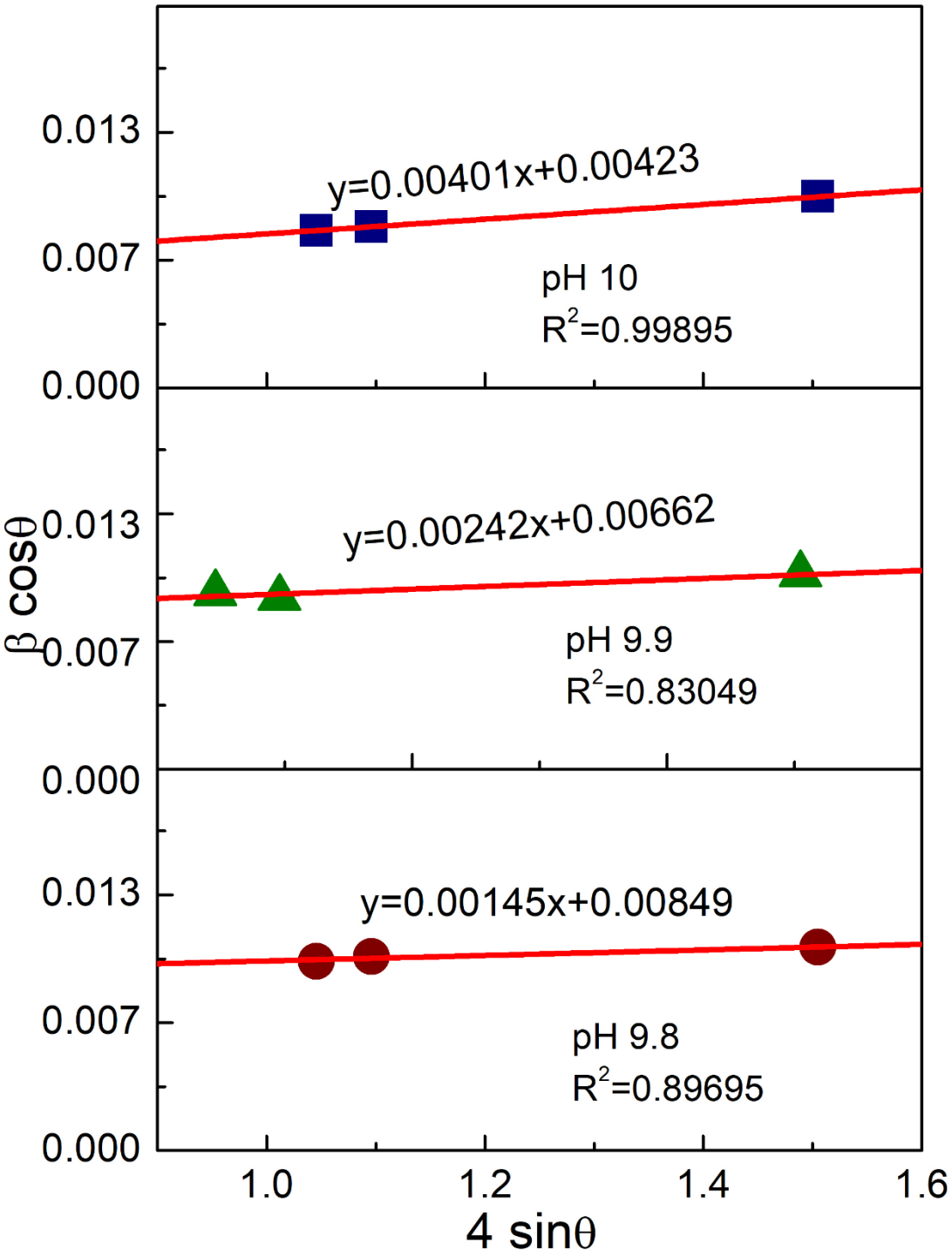

Figure 3.8 Williamson-Hall plots of SnS for different pH of the bath solution

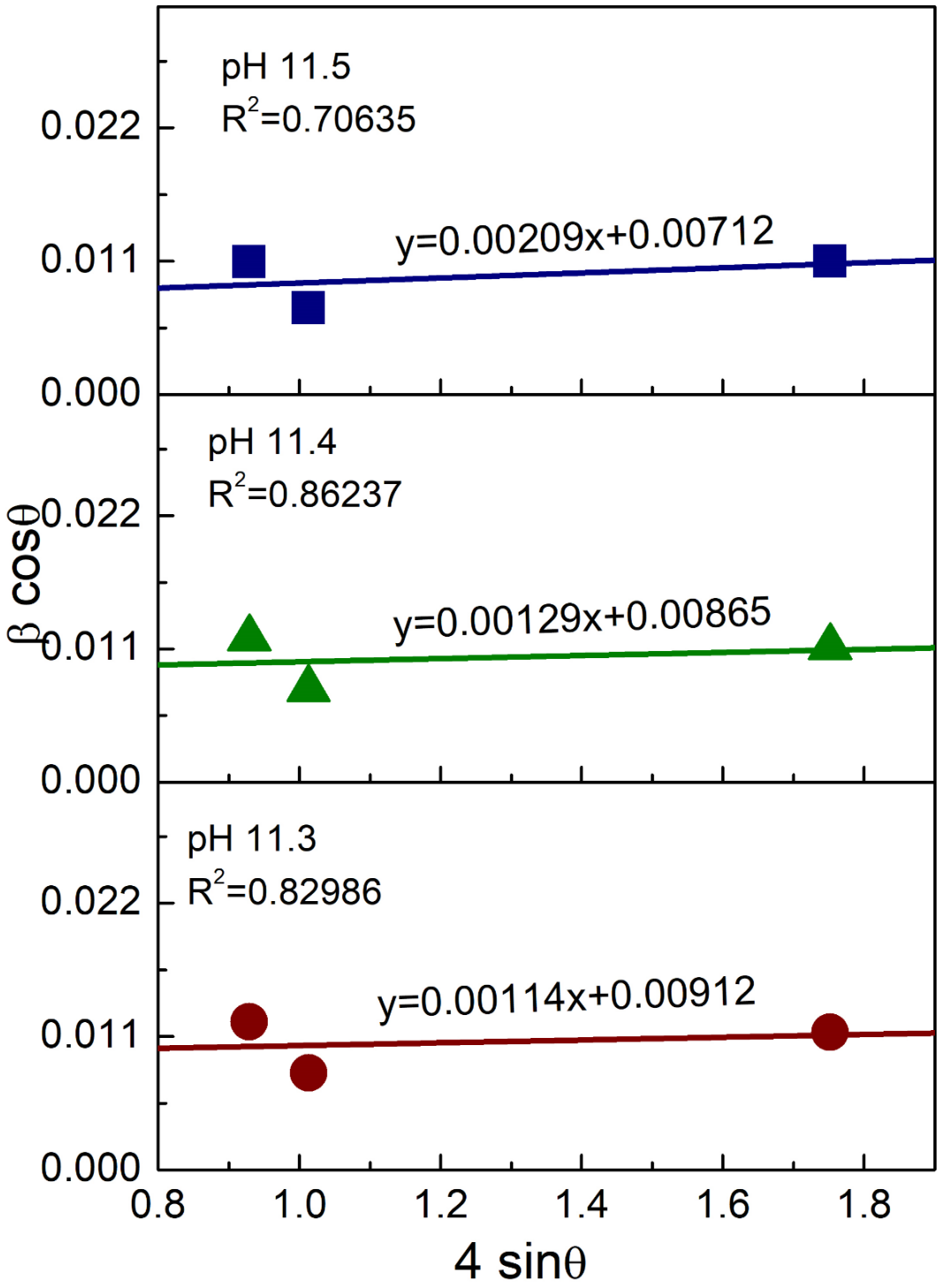

Figure 3.9 Williamson-Hall plots of CdS for different pH of the bath solution

Effect of pH on SnS and CdS thin films

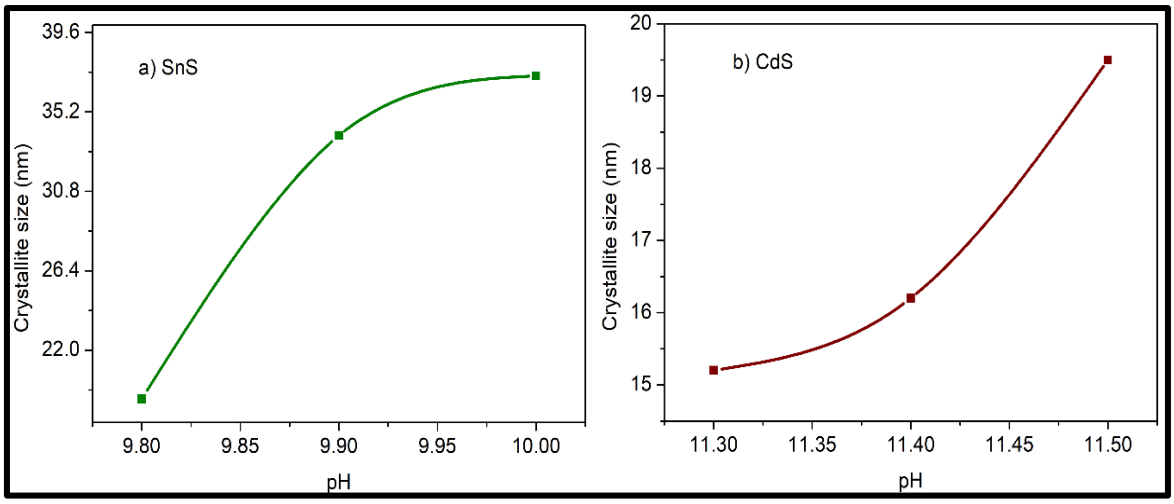

Figure 3.11 Variation of crystallite size with pH (a) SnS (b) CdS

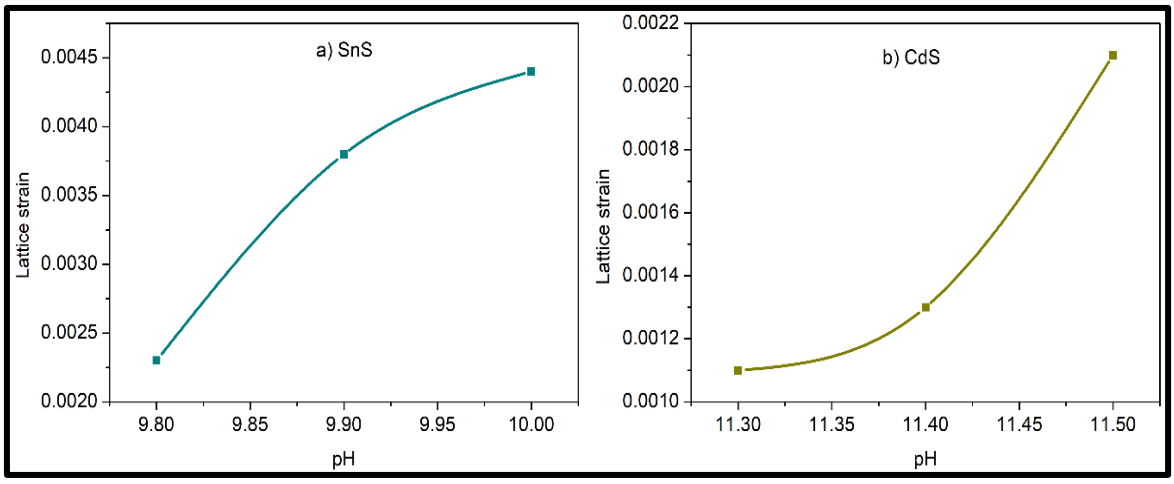

Figure 3.10 Variation of lattice strain with pH (a) SnS (b) CdS

For the CdS thin films, it was found to be 0.00114, 0.00129, and 0.00209 for the pH values of 11.3, 11.4, and 11.5. From figure 3.11 (b) the microstrain of the CdS thin films also increases as the pH of the solution increases because more cations in the solution increase the density of the thin films, which causes an increase in the strain. The XRD data points are tabulated in table 3.1.

Table 3.1 XRD data table of SnS and CdS thin films with varying pH values.

	pH values	2theta		Miller planes	Microstrain	Crystallite size (nm)
		Observed (°)	Standard (°)			
SnS	9.8	30.5	30.5	(1 1 0)	0.0023	19.3
		31.5	31.6	(0 1 3)		
		44.3	44.8	(0 2 2)		
	9.9	30.6	30.5	(1 1 0)	0.0038	33.9
		31.6	31.6	(0 1 3)		
		44.3	44.8	(0 2 2)		
	10	30.5	30.5	(1 1 0)	0.0044	37.2
		31.7	31.6	(0 1 3)		
		44.3	44.8	(0 2 2)		
CdS	11.3	26.9	26.7	(1 1 1)	0.0011	15.2
		29.3	30.9	(2 2 0)		
		51.8	52.5	(1 1 3)		
	11.4	26.8	26.7	(1 1 1)	0.0013	16.2
		29.1	30.9	(2 2 0)		
		51.8	52.5	(1 1 3)		
	11.5	26.8	26.7	(1 1 1)	0.0021	19.5
		29.3	30.9	(2 2 0)		
		51.7	52.5	(1 1 3)		

3.3.3 Raman Analysis

The Raman spectra of SnS and CdS thin films are shown in Figures 3.12 (a) and (b), respectively. The prominent peaks related to SnS phonon modes are clearly observed at 94 cm^{-1} (A_g), 160 cm^{-1} (B_{2g}), and 221 cm^{-1} (A_g) in the spectra. To become more knowledgeable about the scientific literature, a description of the nomenclature used in group theory and vibrational spectroscopy has been given. The symmetry species of a system is represented by Mulliken shorthand symbols. The species represented by A is symmetric with regard to the primary axis of symmetry, and B is in opposition to the primary axis of symmetry. E represents a two-dimensional, irreducible, double-degenerate representation, and T represents a three-dimensional, irreducible, triple-degenerate representation. g and u depict those that are symmetric and antisymmetric with respect to a center of symmetry

respectively. A subscript 1 shows that the system is symmetric with respect to an axis that is perpendicular to the principal axis, and a subscript 2 represents that which is antisymmetric [116]. During the interaction of radiation with the lattice it vibrates and this vibration can be longitudinal (L) or transverse (T). Lattice vibrations can be low in energy which is termed as acoustic and high energy as optic [117].

The B_{2g} mode represents the interaction through the interlayer b axis, whereas the A_g mode indicates the symmetric Sn-S bond stretching in the a-c plane. The spectra are comparable to those of the bulk crystal and concur with past studies on SnS thin films. These results suggest that a SnS thin film with good crystallinity has been synthesized on the glass substrate. Among the Ag modes identified, the peak at 221 cm^{-1} was attributed to the longitudinal optical (LO) mode, while the peak at 94 cm^{-1} was assigned to the transverse optical (TO) mode [51]. The films made from bath solutions with high pH values were found to have strong and sharp Raman line intensities, emphasizing good formation in these films. The peak intensities of the SnS thin films increase as the pH of the bath solution increases, which is consistent with the XRD patterns displayed in figure 3.5 (a).

Figure 3.12 (b) depicts two distinct bands in the Raman spectra of CdS films at various pH values. These two peaks, which were observed at 300 cm^{-1} and 600 cm^{-1}, respectively, represent the CdS crystal's first and second-order longitudinal optical phonon (LO) modes. The results match those of the bulk crystal and are consistent with earlier studies on CdS thin films [32,33].

The intensity of different Raman peaks of SnS and CdS for different pH values are displayed figure 3.13(a) and (b) respectively. The Raman peak intensities of both films rose as the pH values increased, which is consistent with the XRD patterns in figure 3.5 (b). It should be noted that the Raman spectra may be noticeably affected by the larger crystallite size of the SnS phase in thin films. It is well known that the number of scattering centers in the volume of the sample illuminated by the laser beam directly relates to the intensity of the Raman scattering. Xu et al. [120] revealed this influence of crystallite size on the Raman spectra, where Raman peaks were shown to be stronger and sharper [121] as the grain size increased.

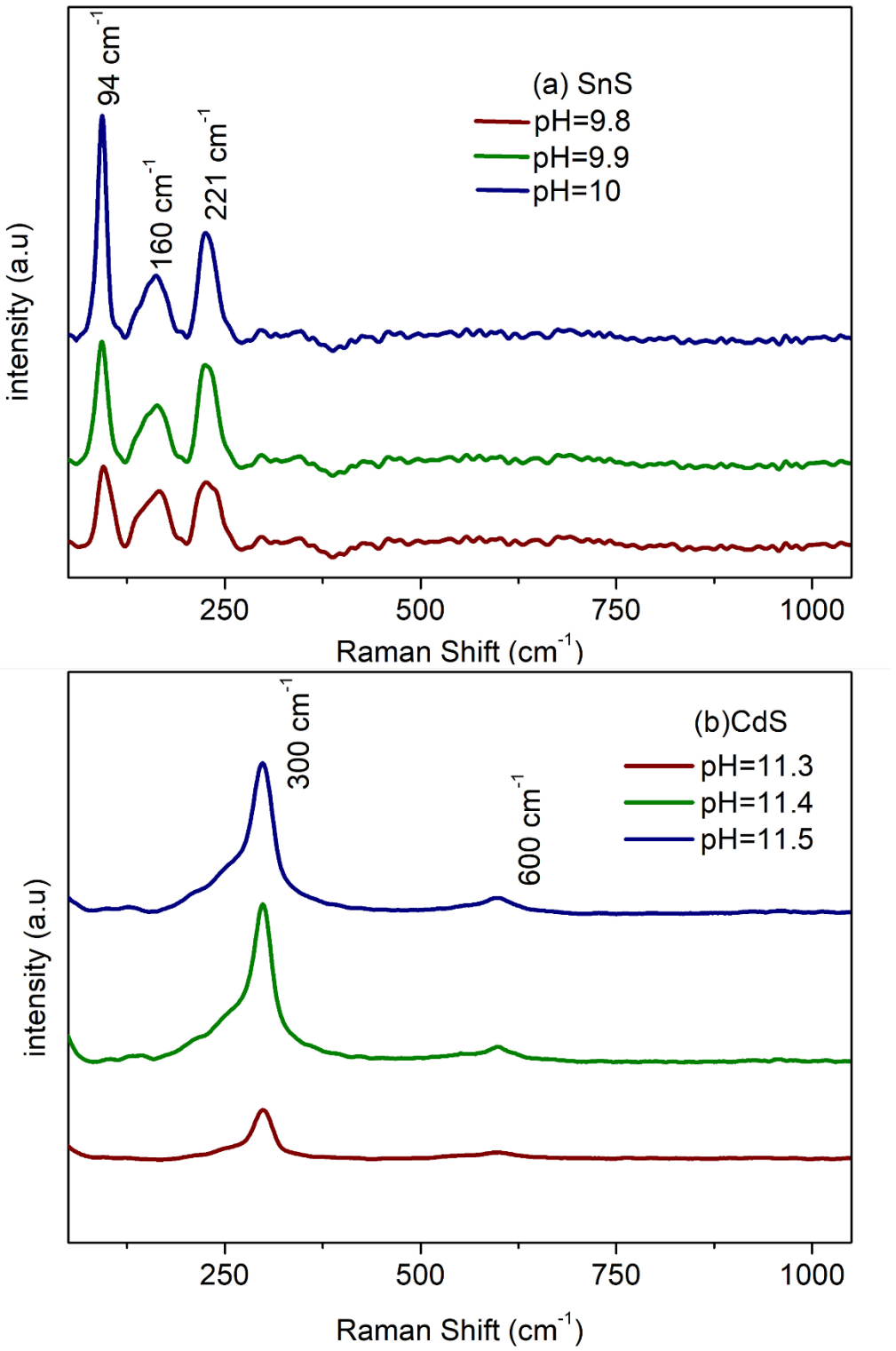

Figure 3.12 Raman analysis of SnS (a) and CdS (b) films deposited with various pH of the bath solution

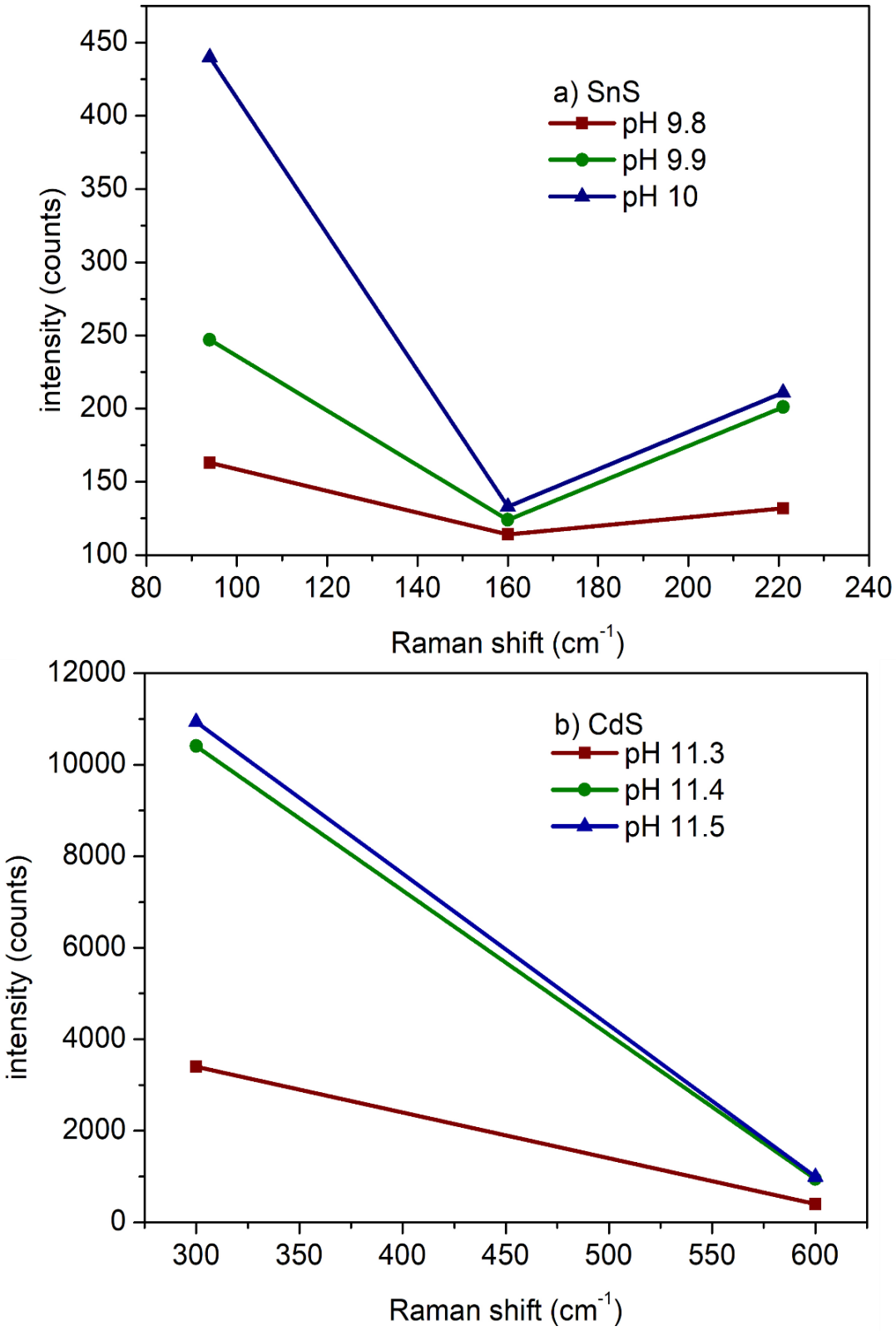

Figure 3.13 Intensity of Raman peaks (a) SnS and (b) CdS

3.3.4 Optical properties

Figures 3.14 (a) and (b) show the absorption spectra (inset) and tau plot of SnS and CdS thin films prepared at different pH values of the source solutions. The absorption spectra showed a red shift as pH values increased for both SnS and CdS thin films.

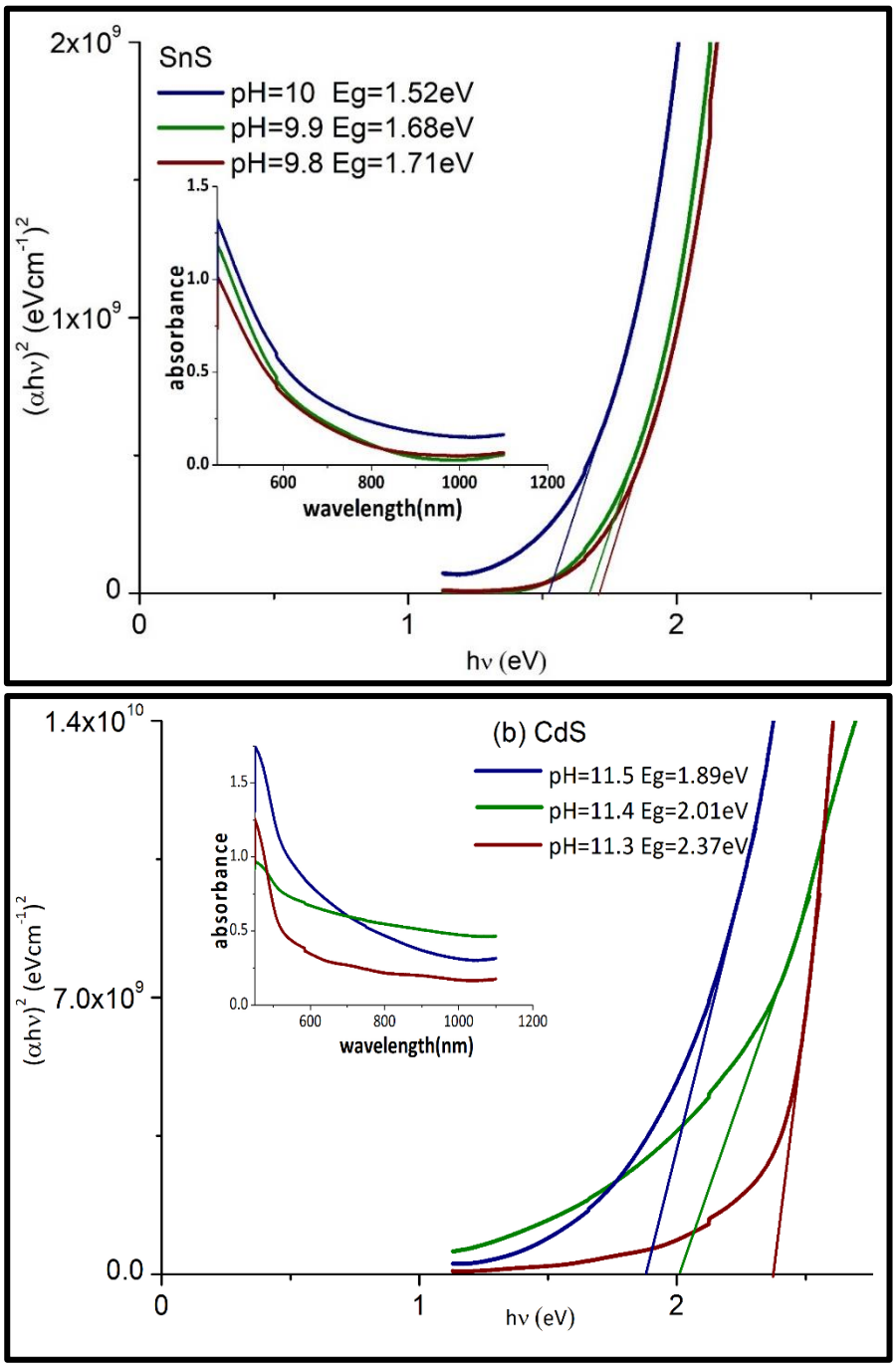

Figure 3.14 Absorption spectra (inset) and Tauc plots of SnS (a) and CdS (b) films deposited with various pH of the bath solution

Effect of pH on SnS and CdS thin films

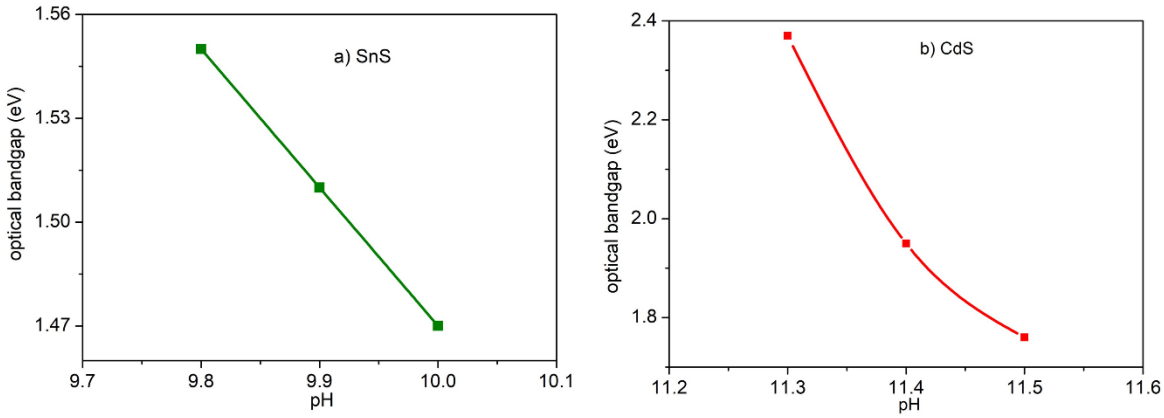

Figure 3.15 Variation of optical bandgap of (a) SnS and (b) CdS with pH

The tauc relation connecting bandgap energy and absorption coefficient (α) is given as αhυ = A (hυ- Eg) n Where A denotes a constant, h denotes photon energy, υ the frequency, Eg denotes the allowed energy gap, and n = 1/2 denotes the allowed direct transition as mentioned in chapter 2. For a direct bandgap semiconductor, a tauc plot is drawn with hυ on x the axis and (αhυ)2 on the y axis. The presence of the linear portion in the curve indicates the presence of a direct optical transition in the material.

SnS thin films had band gaps of 1.71 eV, 1.68 eV, and 1.52 eV, corresponding to pH values of 9.8, 9.9, and 10, respectively. CdS, on the other hand, had larger band gaps of 2.37 eV, 2.01 eV, and 1.89 eV for pH values of 11.3, 11.4, and 11.5, respectively. Due to its wider optical band gap, CdS can be used as a window layer for the solar cells. Similarly, moderate values of band gap in SnS thin films make them suitable candidates for absorber layers.

Figure 3.15 shows the variation of optical bandgap with the pH of the bath solution. The energy band gap can be determined by extrapolating the straight portion of the plot to the energy axis. The energy gap increases as the pH of the bath solutions decreases for both SnS and CdS. The increase in the energy gap may be due to the existence of grain boundaries in the polycrystalline structures, which results in free carrier concentrations and the existence of potentials in the boundaries. Therefore, an electric field was formed, and the band gap increased. It's possible that the decreasing band gap may be due to larger grains and this result in improved crystallinity [106].

3.3.5 Morphological studies

Figure 3.16 displays FESEM images of the SnS and CdS films. All the films formed were crack free, homogeneous and continuous.

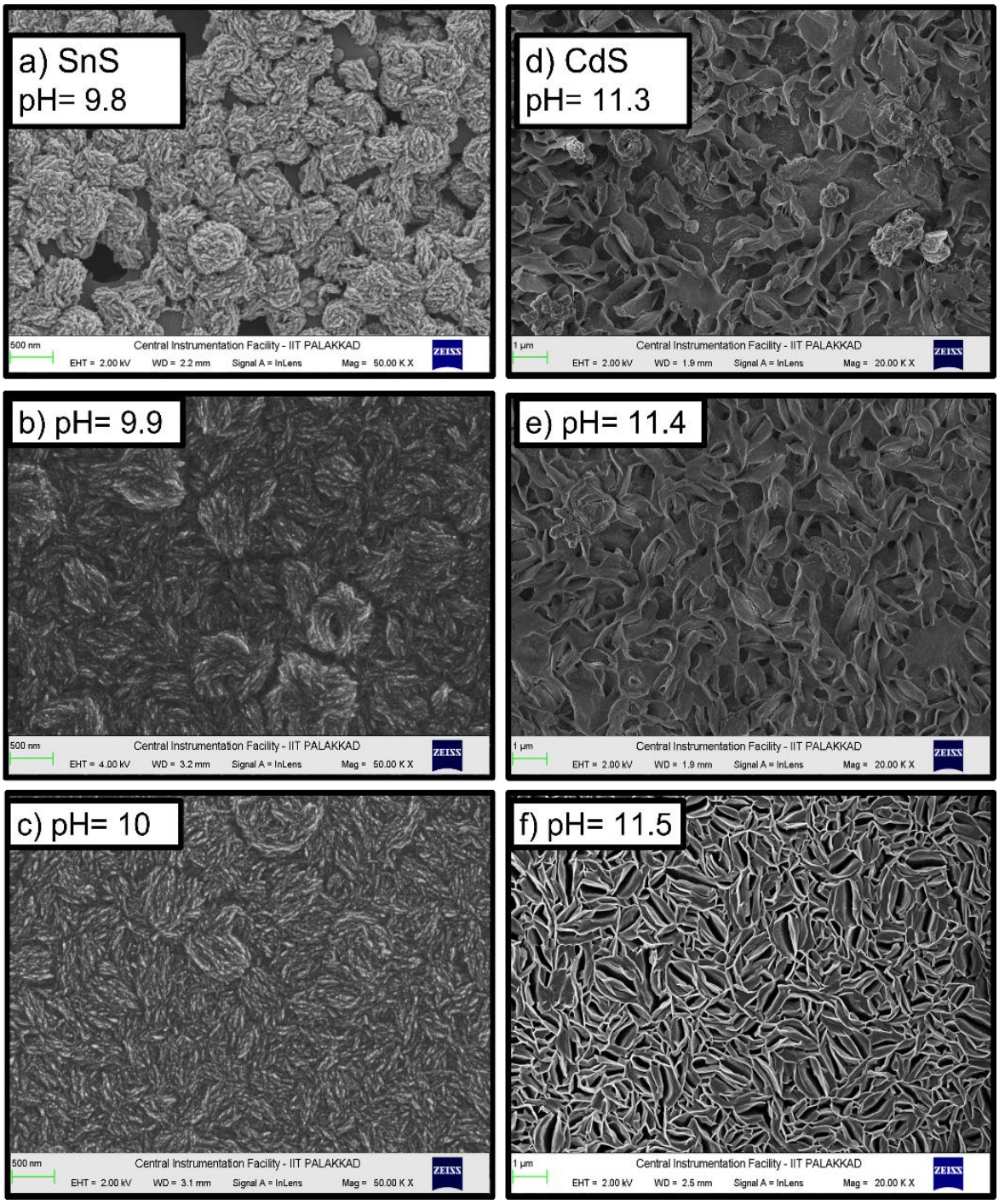

Figure 3.16 Field emission scanning electron microscopy (FESEM) images of (a-c) SnS and (d-f) CdS thin films deposited with various pH of the bath solution

Effect of pH on SnS and CdS thin films

While analyzing the morphology of SnS films (figures 3.14 (a)–(c)), it was evident that the number of clumps in the film increased and more homogeneous structures formed at higher pH levels. Additionally, it was discovered that the density of clusters gathered at the lowest pH level of 9.8 was low, leaving voids and creating a more porous structure.

Figure 3.14 (d)–(f) depicts the surface morphology of a CdS thin film, which displayed a well-adhered, homogeneous, densely packed, and pinhole-free film. The micrograph also revealed that the films were continuous and had a flake-like morphology. As the pH of the bath solution increased, the interconnected nanoflakes were observed to develop an asymmetrical nanosheet-like morphology and spread throughout the surface.

3.3.6 Compositional analysis

Figure 3.17 (a)–(c) indicates the EDS spectra of SnS thin films with various pH values showing the presence of Sn and S peaks. The other unnamed peaks arise from the substrate used. No other contaminant peaks showed up in the spectra.

When a sample is irradiated with highly energetic beam of electrons then a characteristic X-ray is generated. Due to irradiation when an electron is excited from the inner shell of its parent atom, the vacant place is occupied by the higher energy electron from the outer shell and the energy difference between the two shells is emitted as an X-ray. The joule of energy liberated in electron transfer is dependent upon from which shell it is transferring to which shell. Emitted X-rays energy as well as number through specimen is obtainable by an energy dispersive spectrometer. Because the energy (wavelength) of these emitted X-rays is unique to the element from which they originate, they are referred to as characteristic X-rays. Thus, elemental analysis can be done using this method. The distinctive X-rays released by excited K-shell electrons are known as "K Lines," whereas those emitted by excited L and M shell electrons are known as "L Lines" and "M Lines," respectively [100]. The typical EDS spectra of the CdS thin films for different pH values of bath solution are given in Figure 3.18 (d)–(f). The cadmium (Cd) and sulphur (S) peaks are clearly visible in the spectra, and other contaminant peaks were absent. The atomic ratios of Sn/S and Cd/S obtained were greater than the expected stoichiometric ratio of unity, which indicates the surface of the sample was rich in metal. Both SnS and CdS thin films go to a metal rich composition with increasing pH values of the bath solution.

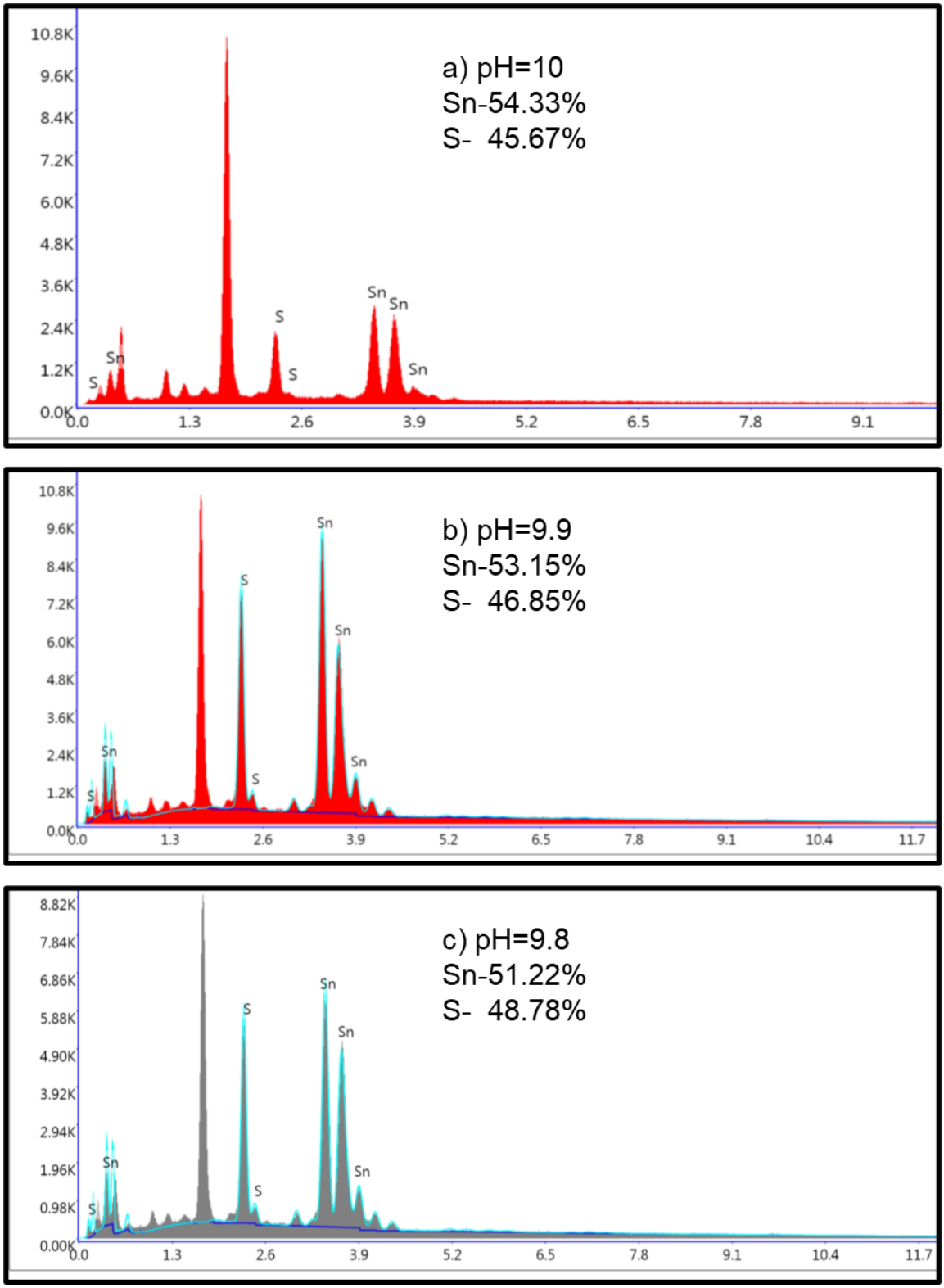

Figure 3.17 EDS images of SnS thin films (a-c) deposited with various pH of the bath solution

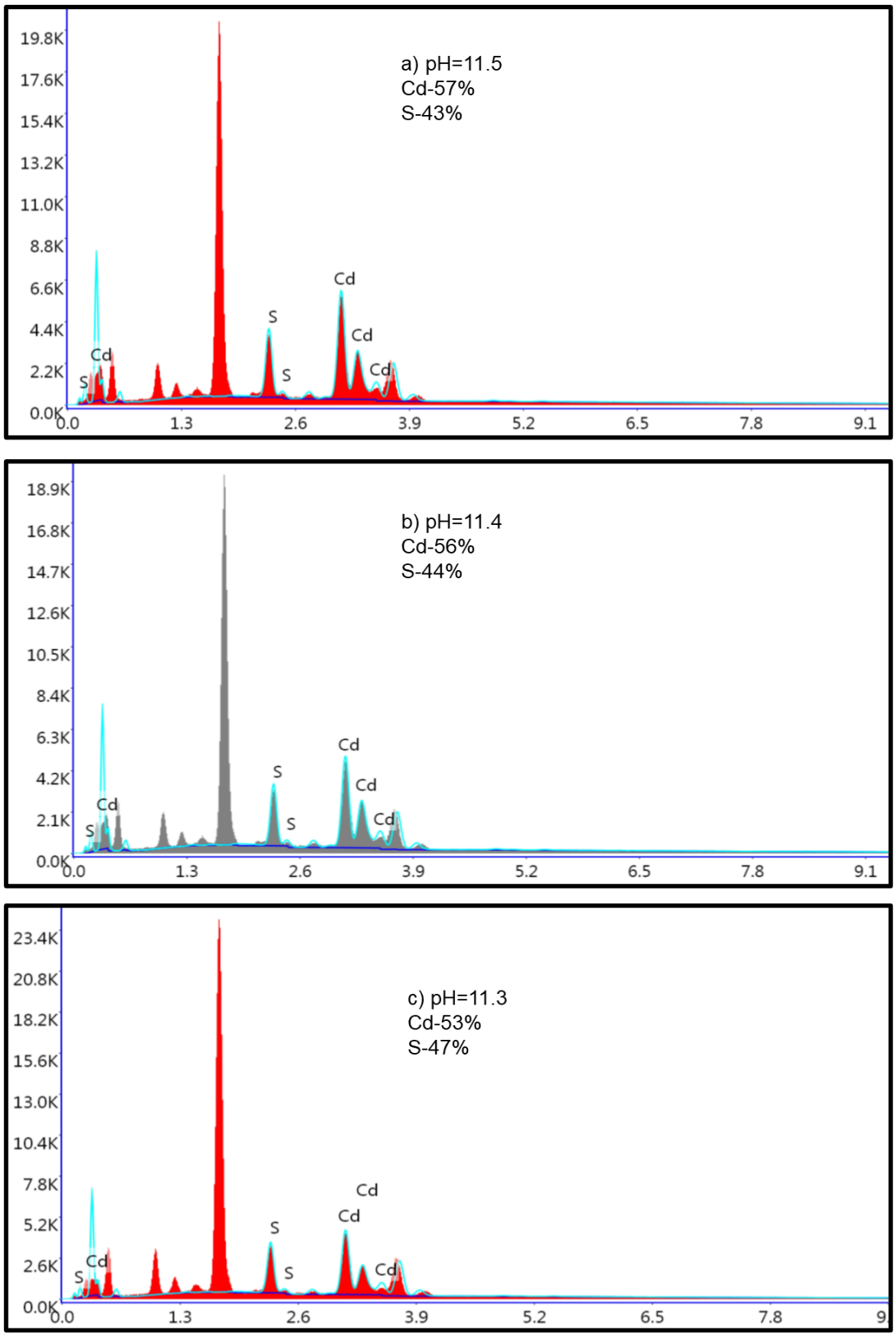

Figure 3.18 EDS images of CdS thin films (a-c) deposited with various pH of the bath solution

This finding is consistent with the fact that as the pH of the solution increased, the OH-ions liberated more and more cations into the solution

3.3.7 I-V characterization

Finally, a SnS based solar cell was fabricated using commercial ITO (Indium Tin Oxide) as the front contact, CdS as an n-type semiconductor, SnS as a p-type semiconductor, and silver paint as the back contact (ITO/CdS/SnS/Ag). I-V characterization for different combinations of pH values is shown in figure 3.19 The table 3.2 shows the open circuit voltage (Voc), short circuit current (Jsc) and efficiency for all the combinations. Better cell performance was exhibited by the heterojunction fabricated with the combination of SnS with the highest pH value (pH = 10) and CdS with the lowest pH value (pH = 11.3) with a conversion efficiency of 0.12×10-3 %. The short circuit voltage of the cell produced is on par with the highest reported efficiency of SnS based solar cell [60]. But the current produced by the cell is very low. This may be due to the recombination of photo carriers in SnS thin films. The characteristics of the cell's components need to be optimized upstream in order to increase the output photovoltaic performance. The optimal selection of n type layer and proper pH of the solution which in turn determines the structural, optical, morphological and compositional can achieve this [35].

Voc value mainly depend on the crystallinity and the band gap of the absorber layer which is better for the SnS thin films prepared from the bath solution with pH value 10. The value of Isc mainly depends on the density of photons that reaches the junction which is possible when the window layer has wider band gap. In this combination, SnS thin films have the high crystallinity, morphological uniformity, lowest band gap, and high absorption required for an absorber layer, while the CdS film has the highest band gap and lowest absorption, making it suitable for a window layer[60], [108], [122], [123].

Generally, poor photovoltaic efficiency is exhibited by SnS-based solar cells for a number of reasons, including insufficient CBO (Conduction Band Offset), carrier recombination, high resistivity of SnS thin film, sulphur vacancies, low thickness, etc.[13], [39]. A better-quality films cans be produced by annealing, which is discussed in chapter 4. The light

trapping techniques like back reflectors and anti-reflective coatings can be used to get a better performance which is discussed in chapter 6.

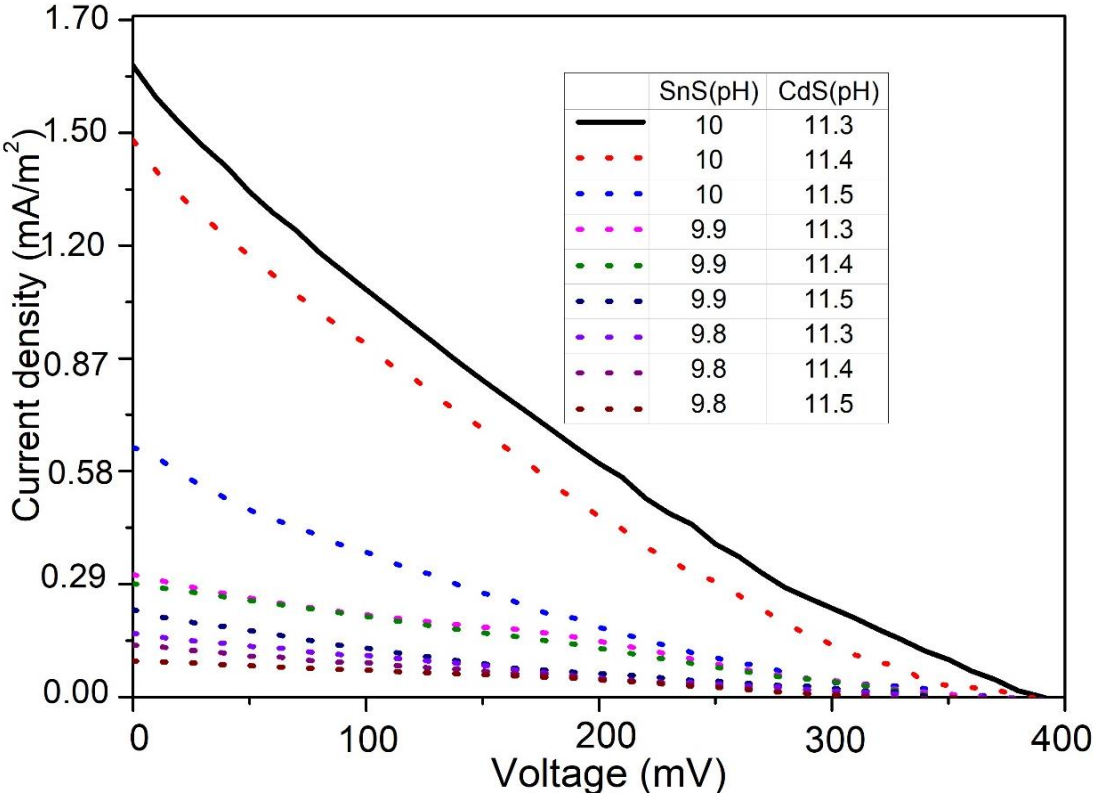

Figure 3.19 I-V characteristics of SnS/CdS photovoltaic cell

Table 3.2 The cell parameters of SnS/CdS photovoltaic cell

SnS (pH)	CdS (pH)	V_{oc} (mV)	J_{sc}(mA/m^2)	Efficiency (%)
10	11.3	390	1.62	$0.120*10^{-3}$
10	11.4	383	1.43	$0.040*10^{-3}$
10	11.5	370	0.64	$0.036*10^{-3}$
9.9	11.3	365	0.32	$0.026*10^{-3}$
9.9	11.4	350	0.29	$0.013*10^{-3}$
9.9	11.5	340	0.22	$0.012*10^{-3}$
9.8	11.3	334	0.16	$0.011*10^{-3}$
9.8	11.4	326	0.13	$0.010*10^{-6}$
9.8	11.5	312	0.092	$0.003*10^{-3}$

3.4 Conclusion

SnS and CdS thin films were synthesized chemically for different pH values of bath solutions. The optimal pH values for SnS film formation were 9.8, 9.9, and 10, while the pH values for CdS were 11.3, 11.4, and 11.5. Film formation did not take place outside this pH range at ambient conditions. The structural, morphological, optical, and chemical characterization revealed changes in the thin film properties with the pH variation. Structural analysis showed an increase in crystallite size for SnS and CdS as the pH of the solution increased. The optical band gap was found to decrease as the pH of the solution increased for both materials. Morphological studies showed that the film became more continuous and uniform as the pH of the bath solution increased. The atomic weight of metal increased as the pH increased, according to the EDS spectra of both films. Photovoltaic cells were fabricated with an ITO/CdS/SnS/Ag configuration, where the SnS thin film deposited at pH = 10 and the CdS film deposited at pH = 11.3 showed better performance. It was observed that the pH of the bath solution has an effect on the efficiency of the photovoltaic cell. Even though, the cell performance of the fabricated heterojunction was poor, the successful formation of the p-n junction was confirmed. However, SnS thin films are potential candidates for solar cells, and trials can be made to improve the solar cell's performance by optimizing the cell configuration.

Chapter 4

Effect of annealing on SnS thin films

4.1 Introduction

Various scholars have claimed that the structural, optical, morphological, and chemical characteristics of the various constituent layers have an impact on the efficiency of thin film solar cells, especially the absorber layer [105]. T. Ben. Nasr et al. [113] suggested that the physical properties of the ZnS thin film can be modulated, and Melda Francis et al. [112] studied the effect of annealing on the structural and optical properties of the chemically prepared Cu2Se thin films. In this work, SnS thin films were prepared chemically and annealed at four different temperatures. The effect of annealing temperature on the properties of SnS thin film was investigated. SnS/CdS heterojunctions were fabricated, and the performance of the cells was also evaluated.

4.2 Materials and methods

The pH of the bath solution was optimized as 10 for SnS thin film formation. Glass substrates that had been completely cleaned were submerged in the final solution after the requisite amount of ammonia had been added. The final solution had been brought to 100 ml by the addition of deionized water. The initially clear solution darkened gradually to yellow, then to chocolate brown. After six hours at room temperature, the SnS thin film with a dark brown colour was produced. The formed films were annealed in muffle furnace for different temperatures. In a muffle furnace or muffle oven shown in figure 2.1, the subject material is kept separate from the fuel and all combustion byproducts, such as gases and flying ash. The films were characterized after a half hour of annealing at 100°C, 150°C, 200°C, and 250°C.

Firstly, the SnS thin film was coated and annealed as mentioned before, followed by the deposition of CdS. A thin silver contact was drawn above the heterojunction using silver paste. The I-V characteristics were studied using a Keithley source meter.

Figure 4.1 Muffle furnace

4.3 Results and Discussion

The annealed samples are characterized using XRD, Raman spectroscopy, UV-Vis spectrometer, FESEM and EDS. The I V Characteristics of the cell formed were done using Keithley Source meter.

4.3.1 Structural properties

SnS samples as prepared and those annealed at 100°C, 150°C, 200°C, and 250°C are displayed in figure 4.2. In SnS thin films, an intense peak was observed at a 2θ value of 31.6 ° which, corresponds to the diffraction from the (0 1 3) plane for the films as prepared and those that were annealed at 100 °C. But for those annealed at 150°C and 200°C, the preferred orientation changes to the (1 1 0) plane related to the 2theta value of 30.5 °, while the other peaks determined at 26.9°, 30.5°, and 44.5° were indexed with the (0 1 2), (1 1 0) and (0 2 2) planes, respectively. All the peaks were indexed and compared with the standard ICDD data card of SnS (ICDD file no. 001-0984), and the crystal structure was found to be orthorhombic. The peaks become sharper and more intense on annealing, which shows a better crystallinity [106]. The samples annealed at 250°C showed no peaks of SnS. This may be because the

sulphur in the sample may have escaped at a temperature of 250 °C, causing the breaking of the stoichiometry of SnS.

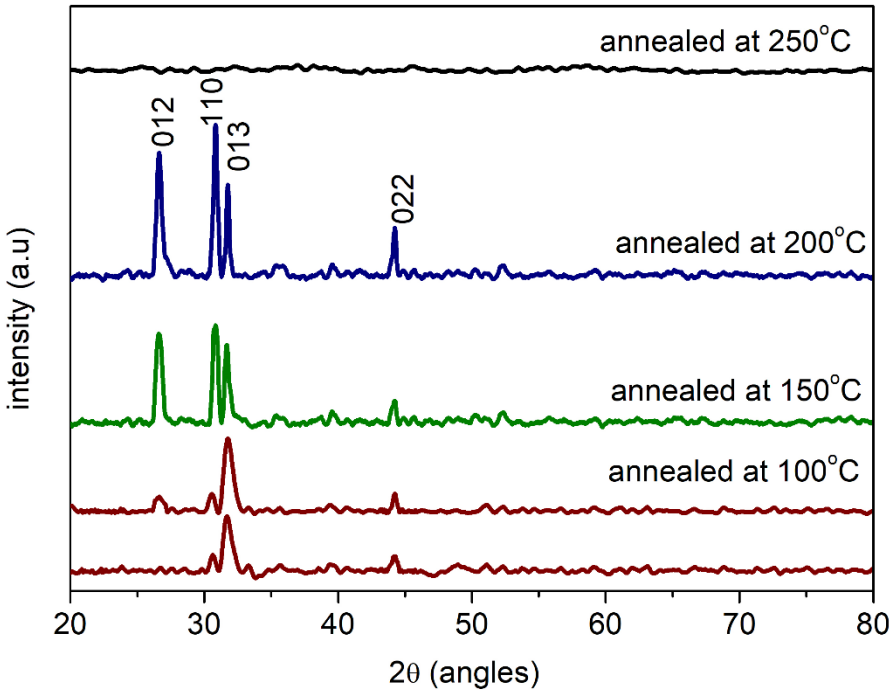

Figure 4.2 The X-ray diffraction patterns of the SnS thin films annealed at different temperatures

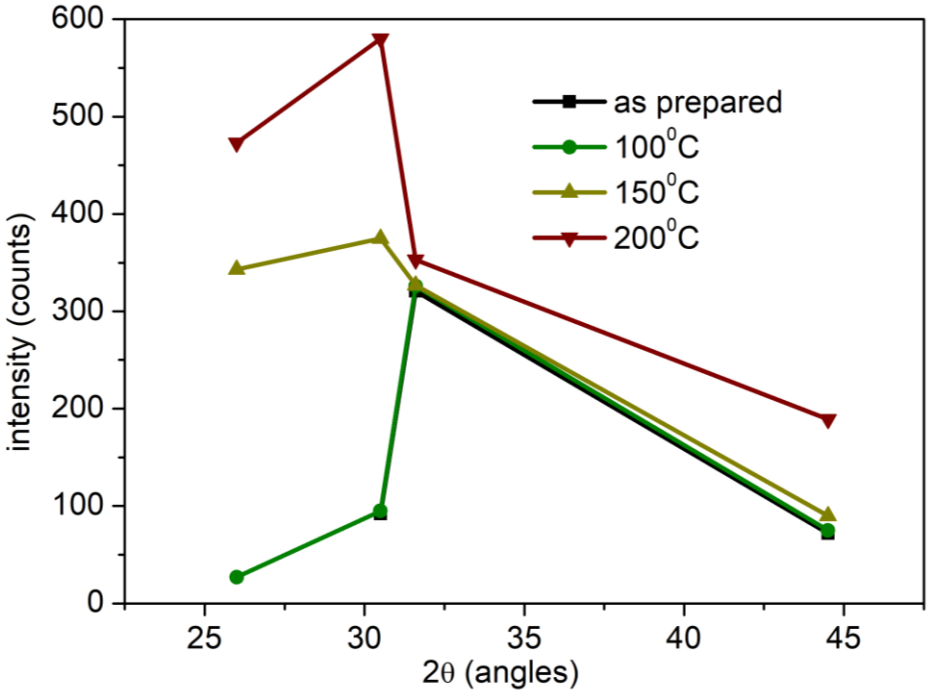

Figure 4.3 The intensity variation of XRD peaks with annealing temperature

4.3.1.1 Williamson–Hall method

Figure 4.4 depicts the W-H plot of as-prepared and annealed samples at temperatures of 100 °C, 150°C, and 200°C.

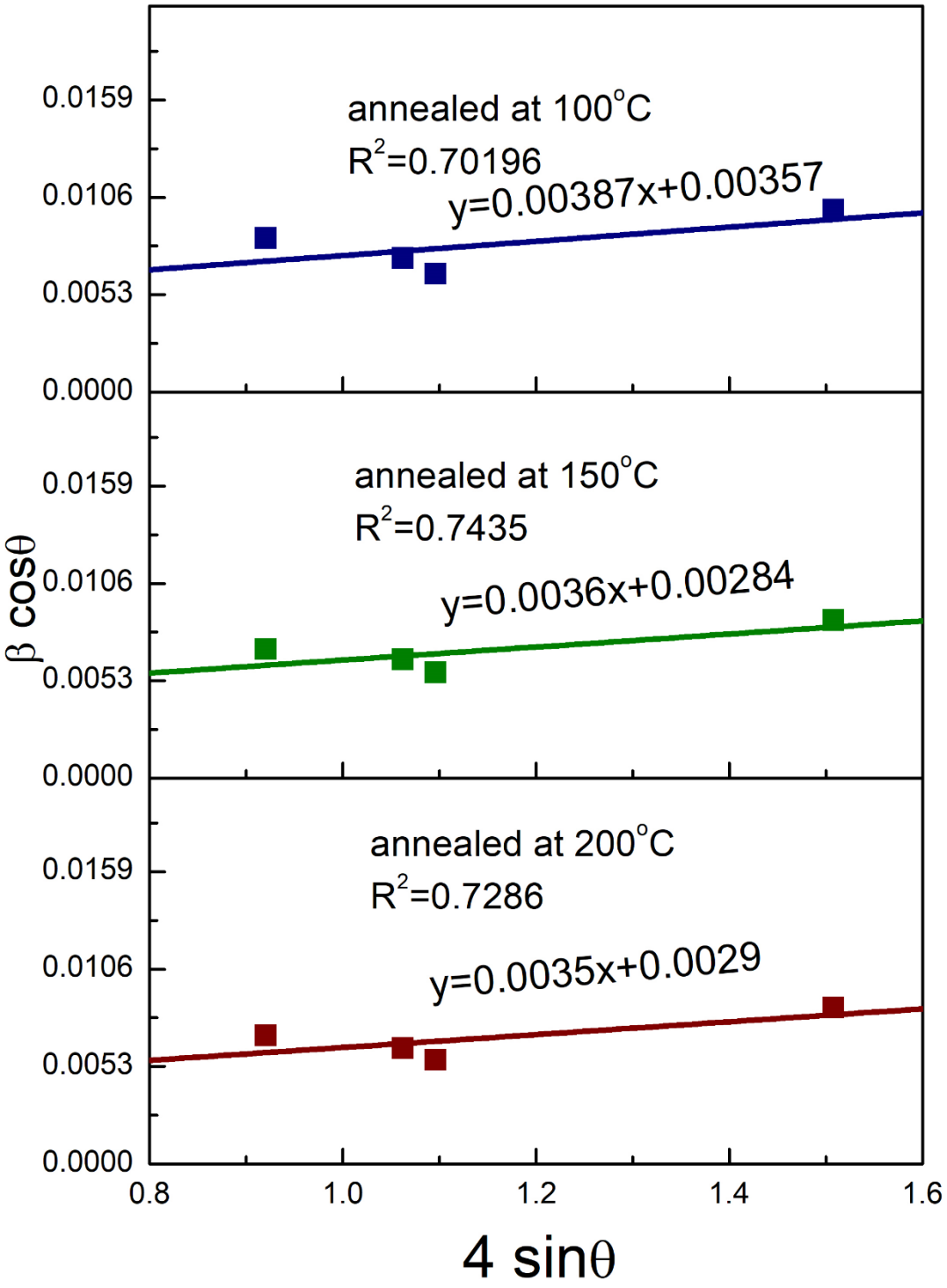

Figure 4.4 Williamson-Hall plots of SnS thin films annealed at different temperature.

Effect of annealing on SnS thin films

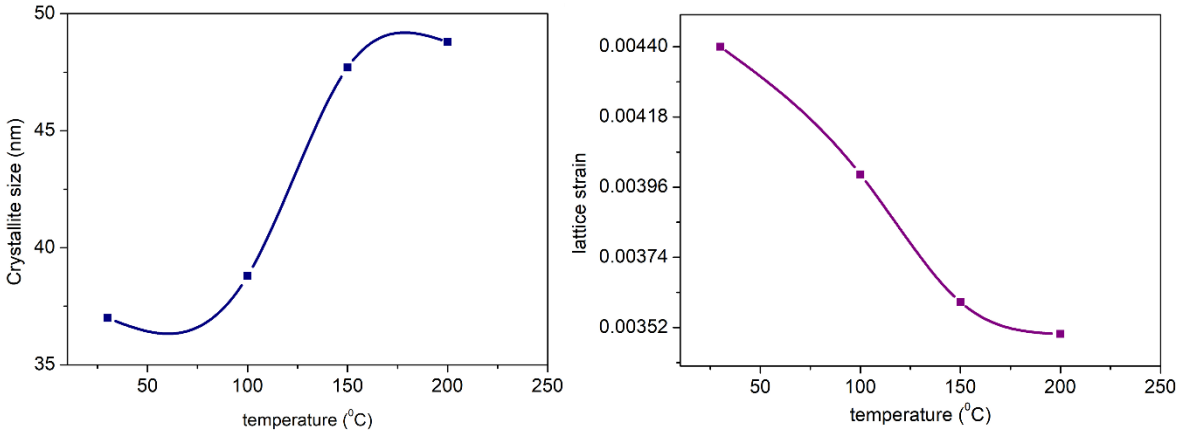

Figure 4.5 Variation of crystallite size and lattice size with annealing temperature

Table 4.1 XRD data of SnS thin films annealed at different temperatures

Annealing temperature (°C)	2theta		Miller planes	Microstrain	Crystallite size (nm)
	Observed (°)	Standard (°)			
As prepared	30.5	30.5	(1 1 0)	0.0044	37
	31.5	31.6	(0 1 3)		
	44.3	44.8	(0 2 2)		
100	26.4	26.0	(0 1 2)	0.0040	38.8
	30.6	30.5	(1 1 0)		
	31.7	31.6	(0 1 3)		
	44.3	44.8	(0 2 2)		
150	26.5	26.0	(0 1 2)	0.0036	47.7
	30.7	30.5	(1 1 0)		
	31.7	31.6	(0 1 3)		
	44.3	44.8	(0 2 2)		
200	26.5	26.0	(0 1 2)	0.0035	48.8
	30.8	30.5	(1 1 0)		
	31.7	31.6	(0 1 3)		
	44.2	44.8	(0 2 2)		

The crystallite sizes were found to be 37 nm, 38.8 nm, 47.7 nm, and 48.8 nm, respectively, for those as prepared and those with annealing temperatures of 100°C, 150°C, and 200°C. The annealing helps to decrease the dislocations in the thin films and increases the crystallite size. The micro strain was determined to be 0.0043, 0.004, 0.0036, and 0.0035 for the as prepared and for annealing temperatures of 100°C, 150°C, and 200°C, respectively.

Figure 4.5 displays the variation of crystallite size and lattice strain with the annealing temperature. The reduction of the grain boundary, the elimination of deformation, and the removal of crystal defects could possibly be responsible for the increase in crystallite size, which indicates that the degree of perfection of the grains has increased. Thus, the reduction in the lattice imperfection reduces the strain in the lattice. Table 4.1 shows the XRD data of SnS thin films annealed at different temperature.

4.3.2 Raman analysis

Figure 4.6 displays the Raman spectra of SnS thin films.

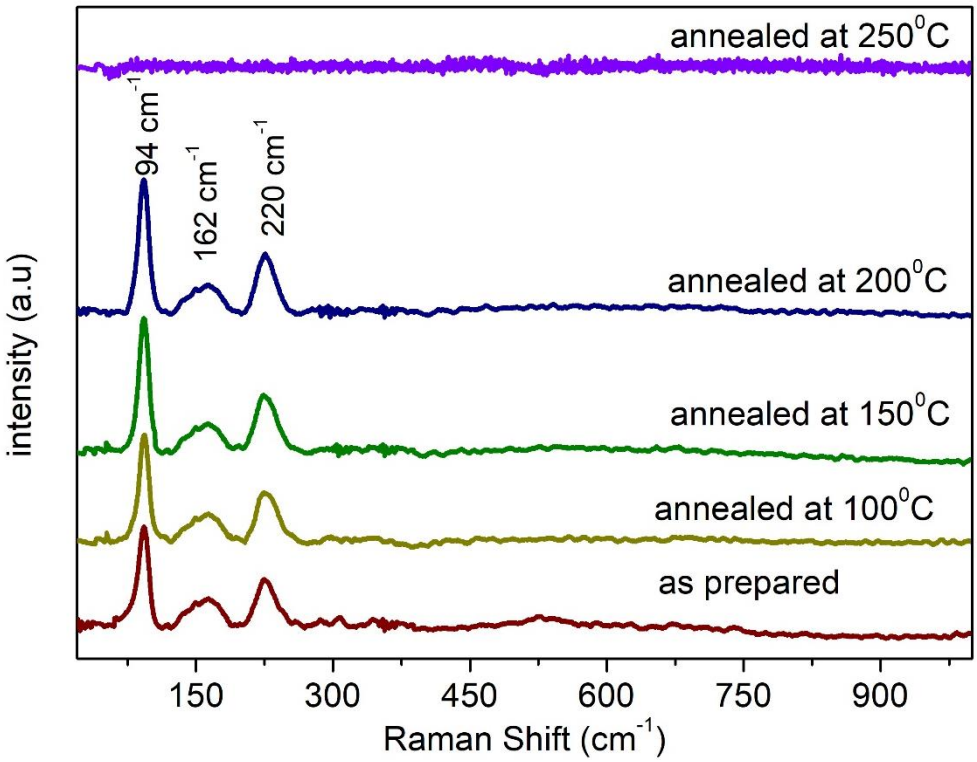

Figure 4.6 Raman analysis of SnS thin films annealed at different temperature

Effect of annealing on SnS thin films

Prominent peaks related to SnS phonon modes are clearly observed at 94 cm^{-1} (Ag), 162 cm^{-1} (B2g), and 220 cm^{-1} (Ag) in the spectra. The B2g mode represents the interaction through the interlayer b axis, whereas the Ag mode indicates the symmetric Sn-S bond stretching in the a-c plane. Among the Ag modes identified, the peak at 220 cm^{-1} was attributed to the longitudinal optical (LO) mode, while the peak at 93 cm^{-1} was assigned to the transverse optical (TO) mode [51][124]. The spectra are comparable to those of the bulk crystal and concur with past studies on SnS thin films. These results suggest that a SnS thin film with good crystallinity has been synthesized on the glass substrate

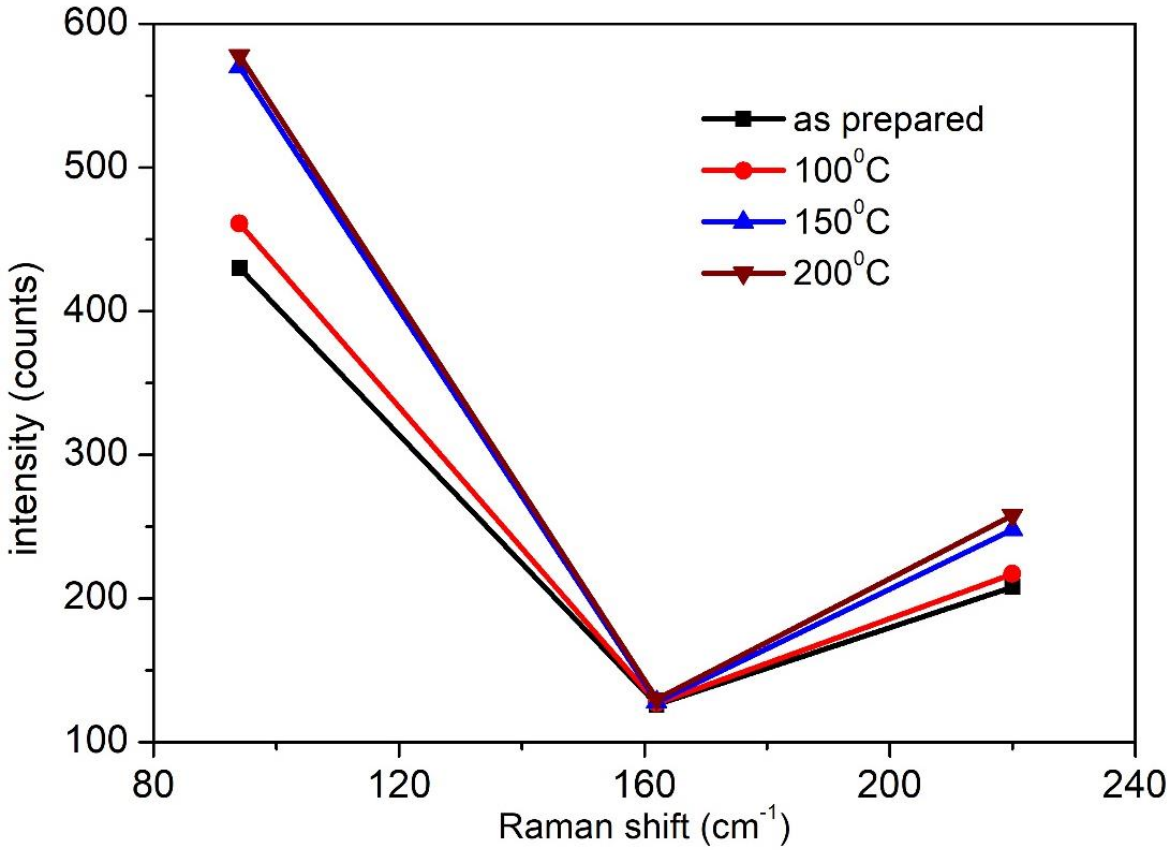

Figure 4.7 Intensity variation of Raman peaks with annealing temperature

Figure 4.7 displays the variation of intensity with annealing temperature. The intensity of Raman lines was found to be high and sharp for the films annealed at 200°C, which emphasizes improved crystallinity in these films and is consistent with the XRD patterns in figure 1. It appears that the SnS peak shows the largest value when annealed at 200°C. In

contrast, the SnS peaks disappear at 250°C or higher temperatures, while they have a considerable intensity at 200°C and below.

4.3.3 Optical properties

Figure 4.7 shows the absorption spectra (inset) and Tauc plot of SnS thin films for as prepared and annealed samples. The absorption spectra showed a red shift as the annealing temperature increased.

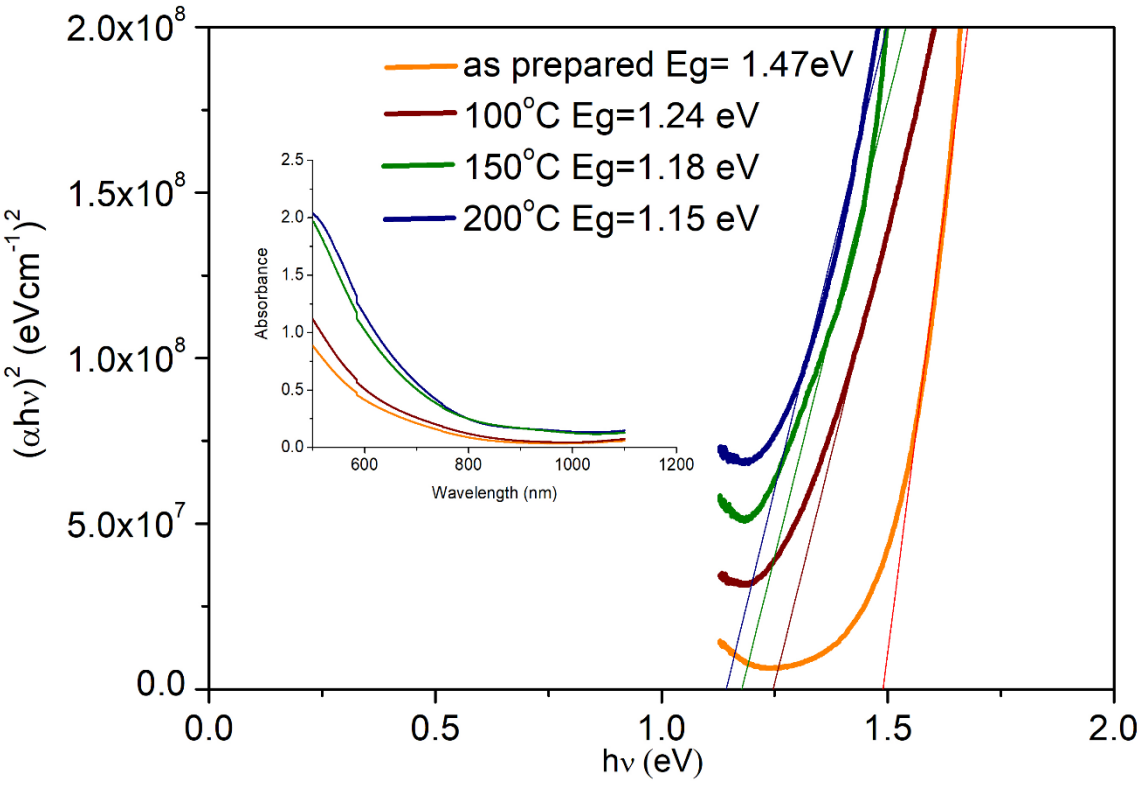

Figure 4.8 Absorption spectra (inset) and Tauc plots of SnS films as prepared and annealed at different temperatures.

The band gaps of SnS thin films were 1.47 eV, 1.24 eV, 1.18 eV and 1.15 eV corresponding to the as prepared and those annealed at 100°C, 150°C, and 200°C, respectively. Figure 4.8 shows the variation of the optical bandgap with annealing temperature. The energy gap increases with a decrease in the annealing temperature. The presence of grain boundaries in polycrystalline structures, which produce free carrier concentrations and the presence of potentials in the boundaries, may be the cause of the expanding energy gap. As a result, an

electric field was created, which caused the band gap to widen. The film annealed at 200°C has a band gap of 1.15 eV, which is appropriate for an absorber layer for effective light absorption.

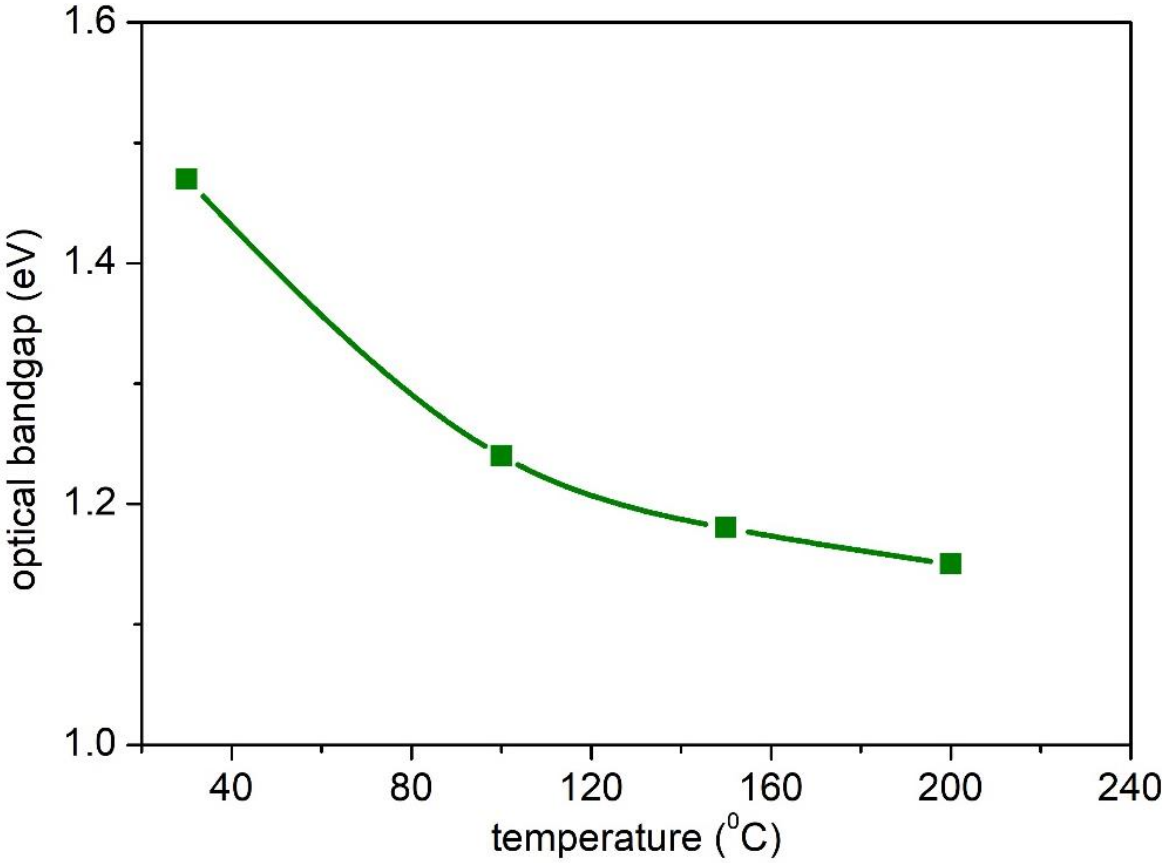

Figure 4.9 Variation of optical bandgap with annealing temperature

4.3.4 Morphological studies

The FESEM images of the SnS films are shown in Figure 4.10. The morphology of SnS films (figure 4.10(a)-(d) revealed that as-deposited layers contain a lot of smaller needle-shaped grains, and as the annealing temperature rises, the grain size increases at the expense of the smaller crystals. The films exhibit considerable growth in three dimensions. These SEM photos clearly show that annealing causes grain development to switch from a needle-like to a plate-like structure. At 200°C, the grains achieve their stable position with improved crystallinity. The reduction of grain boundaries is related to the improvement in crystallinity and grain size at higher temperatures. The films that have been annealed at 200°C are

uniform, smooth, and have a dense surface structure with larger grains than the films that were initially deposited

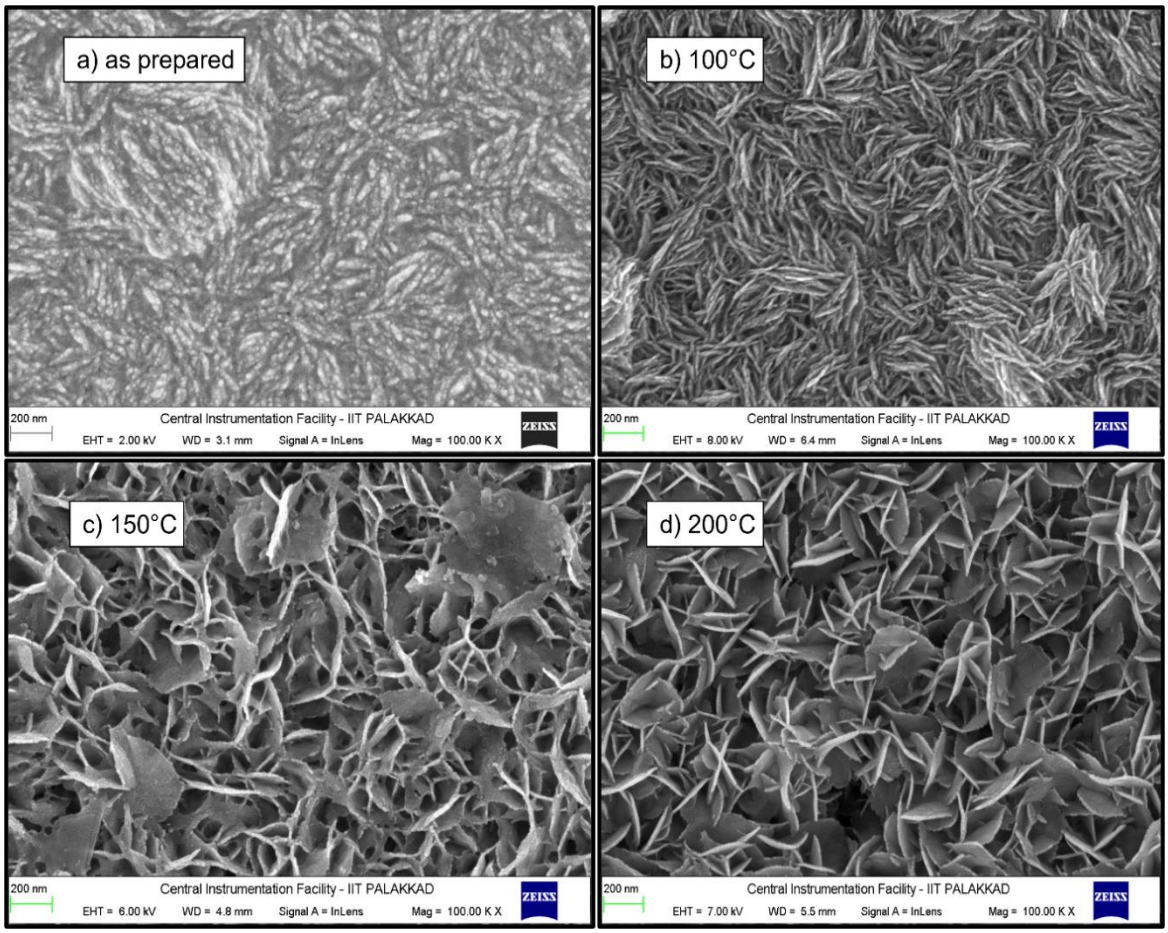

Figure 4.10 Field emission scanning electron microscopy (FESEM) images of SnS

4.3.5 Compositional analysis

The EDS spectra of SnS thin films at various annealing temperatures are shown in Figure 4.11 (a)–(d), demonstrating the presence of Sn and S peaks. The substrates employed give rise to the other unlabeled peaks. The spectra contained no further contamination peaks. The Sn/S atomic ratios found were higher than the predicted stoichiometric ratio of unity, indicating that the sample's surface was metal rich. As the annealing temperature increases, the atomic weight percentage of sulphur decreases. This is because the sulphur may have escaped from the sample with the increase in temperature.

Effect of annealing on SnS thin films

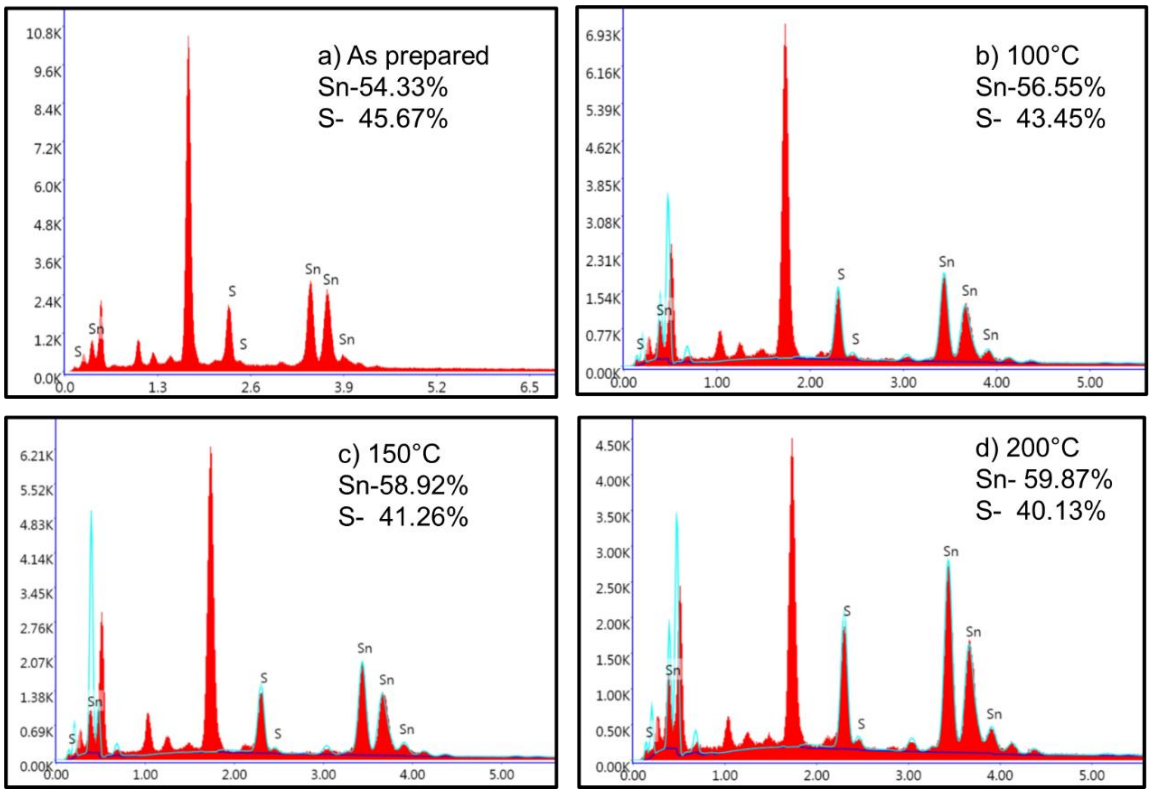

Figure 4.11 EDAX images of SnS thin films annealed at different temperatures.

4.3.6 I-V characterization

In the end, a SnS-based solar cell was created using ITO (Indium Tin Oxide) sold commercially as the back contact, CdS as the n-type semiconductor, SnS as the p-type semiconductor, and silver paint as the front contact (ITO/SnS/CdS/Ag). When the as-prepared SnS films were used as a p-type layer, their efficiency was 0.12×10^{-3} % and the photocurrent was in the order of 10^{-4} mA, which was very low. Then SnS film annealed at 200°C was selected as the p-type material because it demonstrated the best crystallinity among the annealed films. Figure 7 displays the I-V characterization for the aforementioned combination. The open circuit voltage (Voc), short circuit current (Isc), maximum power and current, fill factor, and efficiency are shown in the table that is displayed as an inset in the picture. A 0.01% efficiency was achieved. This is far better than the configuration made out of as-prepared SnS film. Still, the efficiency has to be improved.The insufficient CBO (Conduction Band Offset), carrier recombination, high resistivity of SnS thin film, sulphur vacancies, low thickness, etc. may all contribute to the poor performance[13], [39]. Another

reason may be due to the loss of photons, which can be enhanced using anti-reflective coatings at the front and reflective coatings at the rear end of the configuration.

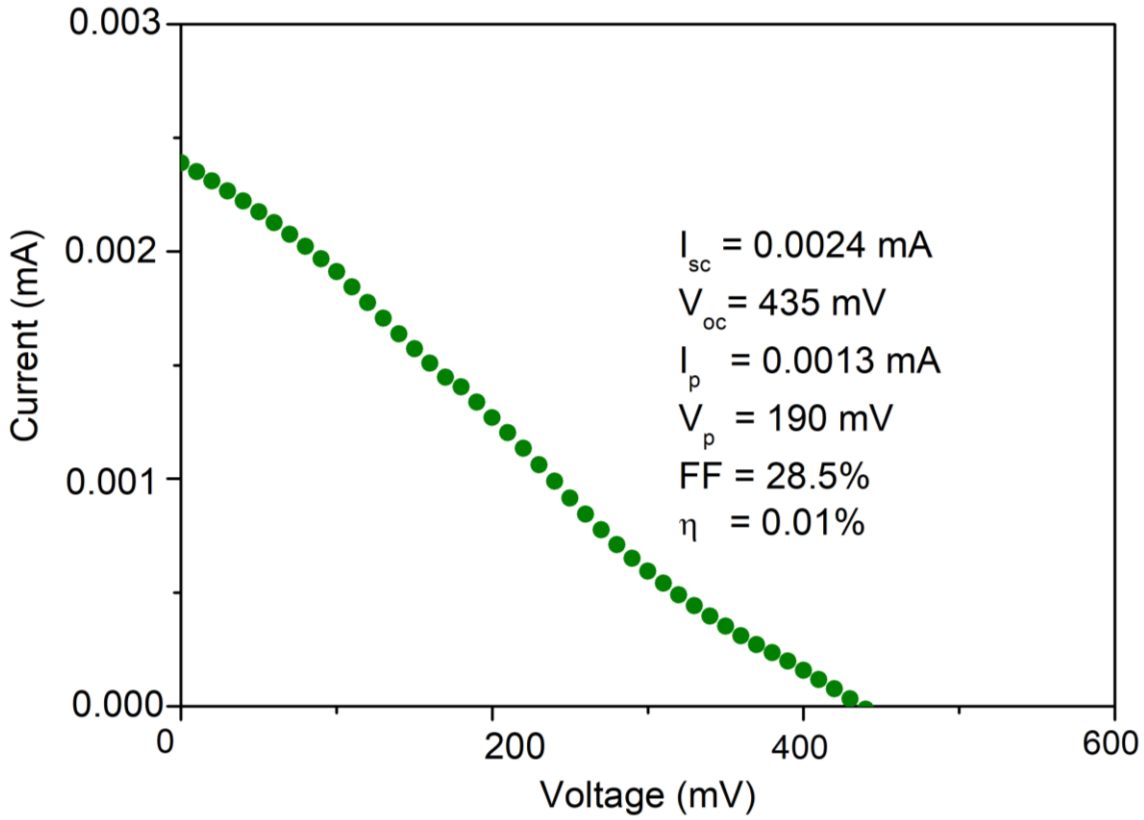

Figure 4.12 I-V characteristics of SnS/CdS photovoltaic cell.

4.4 Conclusion

The chemically created SnS thin films were subjected to various annealing temperatures. The ideal annealing temperature for SnS was determined to be 200°C. No peaks were visible in the films' annealed at 250°C XRD or Raman spectra. The structural, morphological, optical, and chemical characterization demonstrated that variations in the annealing temperature led to modifications in the thin film properties. The films' crystallite size grew as the annealing temperature rose, according to structural analyses. It was discovered that when the annealing solution's temperature rose, the optical band gap shrank. With annealing, morphological tests revealed that the film became denser and the needle-shaped morphology changed to a plate-shaped one, increasing the grain size. The atomic weight of sulphur dropped as the annealing temperature rose, according to EDS spectra. ITO/SnS/CdS/Ag configuration were employed in the construction of photovoltaic cells, and a thin SnS film

that had been annealed at 200°C served as the absorber layer. The efficiency of the solar cell was found to be impacted by the annealing of the film. An increase in efficiency was seen by annealing the SnS thin film. This technique is an inexpensive way to produce SnS thin films for the absorber layer of solar cells.

Chapter 4

Chapter 5

Simulation of 1D Photonic Crystals

5.1 Introduction

Modern advanced electronic, optoelectronic, and photonic devices are in demand for multilayer thin film structures, which are also considered as 1D photonic crystals (PC) [42][125]. Photonic crystals are considered the optical analogue of crystals, in which atoms are replaced by macroscopic periodic dielectric structures. If the periodicity is only in one direction, it is considered a 1D PC; in two directions, a 2D PC; and if it extends in three directions, a 3D PC. We get complete PBG; that is, the gap extends to cover all propagation directions for 3D PC. [70]. As the lattice in crystals prohibits the propagation of electrons with certain energy, the photonic crystals also prevent electromagnetic radiation with a specific frequency. This gap in the photonic band structure is termed the "photonic band gap" (PBG) [126], [127]. A small amount of disorder will not destroy the PBG but will allow localized modes to exist within the gap, which can be utilised for wave guiding. Vertical cavity surface emitting diodes, waveguides, sophisticated solar cells, and other devices all use this method of light manipulation [128].

It is preferable to optimize the PC's design on the computer before building it. They are favorable for computation because the length scales are not too small, and the Maxwell equations that govern the propagation of electromagnetic radiation through the PC are practically exact [129]. The programs called MIT electromagnetic equation propagation (MEEP) were used for computing transmission spectra. Meep implements the finite-difference time-domain (**FDTD**) method. This is a widely used technique in which space and time are divided into a discrete grid and the derivatives of the Maxwell equation are approximated using discrete time steps. This approach can imitate many real-world issues almost identically since it gets closer and closer to the true continuous equations as the grid and time increments are made finer and finer [130].

5.2 Theory of photonic crystals

5.2.1 Master equation from Maxwell's equation.

The four Maxwell's equations control how light moves through photonic crystals.

$$\nabla . \mathbf{B} = 0 \tag{5.1}$$

$$\nabla . \mathbf{D} = \rho \tag{5.2}$$

$$\nabla \times \mathbf{E} = -\frac{\partial B}{\partial t} \tag{5.3}$$

$$\nabla \times \mathbf{H} = J + \frac{\partial D}{\partial t} \tag{5.4}$$

Where ρ and J are the free charge and current densities, E and H are the macroscopic electric and magnetic fields, D is the displacement field, B is the magnetic induction field, and so forth.

We place some limitations on the media that will be taken into consideration in the interest of simplicity. First, it is expected that the medium is free of free charges and currents, homogenous, and time-invariant within regions of the same material. Furthermore, we limit ourselves to linear, isotropic, and non-dispersive materials. According to linearity, E and H are connected to D and B by constitutive relations. excluding all but the fields' first order words, which we express

$$\mathbf{D}(r) = \varepsilon_0 \varepsilon (r) \mathbf{E}(r) \tag{5.5}$$

$$\mathbf{B}(r) = \mu_0 \mu (r) \mathbf{H}(r) \tag{5.6}$$

In isotropic and non-dispersive media, relative permittivity and permeability are constant scalars. Vacuum permittivity and permeability are represented by ε_0 and μ_0, respectively. Since only non-magnetic materials will be taken into account from this point on, $\mu = 1$. The presumption of transparent media, such that is both real and positive, is a last restriction.

Since Maxwell's equations are linear, it is possible to expand them into a collection of harmonic modes in order to isolate the fields' time dependence from their spatial

dependency. A spatial pattern that changes harmonically throughout time is how the fields are express

$$\mathbf{H}(\mathbf{r},t) = \mathbf{H}(\mathbf{r})\, e^{-i\omega t} \tag{5.7}$$

$$\mathbf{E}(\mathbf{r},t) = \mathbf{E}(\mathbf{r})\, e^{-i\omega t} \tag{5.8}$$

Notably, the physical fields will be the real part of these fields, which are today defined mathematically as complex valued functions.

Applying the previously established medium requirements while incorporating the aforementioned two equations into Maxwell's equations (5.1) and (5.2), we arrive at

$$\nabla .\, \mathbf{H}(\mathbf{r}) = 0, \qquad \nabla .\, [\varepsilon(\mathbf{r})\, \mathbf{E}(\mathbf{r})] = 0 \tag{5.9}$$

These equations provide significant constraints on the fields, which can be understood in one of two ways. They first assert that there are neither point sources nor sinks of H nor D. Second, equation (5.9), which assumes a plane wave H(r) = an exp(ik.r), demands that a k = 0. Equation (5.9) is referred to as the transversality criterion since it states that electromagnetic waves must be transverse to create the fields.

We may decouple Maxwell's equations into a wave equation wholly written in H(r) by taking the curl of equation (4) and merging it with equation (3):

$$\nabla \times \left(\frac{1}{\varepsilon(\boldsymbol{r})} \nabla \times \boldsymbol{H}(\boldsymbol{r}) \right) = \left(\frac{\omega}{c} \right)^2 \boldsymbol{H}(\boldsymbol{r}) \tag{5.10}$$

The vacuum speed of light, denoted by the formula $c = 1/\sqrt{\varepsilon_0 \mu_0}$, is the factor c. Since it defines all features of H(r), along with the transversality criterion, equation (5.10) will be referred to as the master equation.

The master equation is an eigenvalue problem, with the eigenvalues being $(\omega/c)^2$ and the eigenfunctions being H(r). For convenience, the differential operator $\hat{\Theta}$ on the left side will be combined into an operator that is defined as

$$\nabla \times \left(\frac{1}{\varepsilon(\boldsymbol{r})} \right) \nabla \times \tag{5.11}$$

Many characteristics of electromagnetic eigenmodes can be understood immediately from those of $\hat{\Theta}$. It follows that every linear combination of the master equation's solutions will be a solution since the operator is linear. Additionally, like the Hamiltonian in quantum physics, $\hat{\Theta}$ is a Hermitian operator.

A number of significant inferences that may be made regarding H(r) and the eigenvalues $(\omega/c)^2$ as a result of the fact that $\hat{\Theta}$ is Hermitian, including mode orthogonality, the requirement that the eigenvalues be real, and the possibility of obtaining the eigenmodes using a variational principle [131], [132].

5.2.2 Electromagnetic variational principle

Despite the complexity of harmonic modes in a dielectric media, there is a straightforward approach to comprehend some of their qualitative characteristics. Generally speaking, a mode, while staying orthogonal to the modes below it in frequency, tends to focus its electric-field energy in areas of high dielectric constant. The electromagnetic variational theorem, which is comparable to the variational principle of quantum physics, can explicitly define this valuable yet ambiguous idea. In specifically, the field pattern that minimises the functional has the lowest frequency mode and the smallest eigenvalue, which is $(\omega/c)^2$.

$$f(H) = \frac{(H,\widehat{\Theta}H)}{(H,H)} \tag{5.12}$$

When H and $\widehat{\Theta}H$ from Maxwell's equation are substituted for in the master equation, we obtain

$$f(H) = \frac{(\nabla\times E,\nabla\times E)}{(E,\varepsilon(r)E)} = \frac{\int d^3r|\nabla\times E(r)|^2}{\int d^3r\varepsilon(r)|E(r)|^2} \tag{5.13}$$

By the variational principle, f(H) should be kept as orthogonal to lower frequency as possible, and f should concentrate E in high-frequency areas to reduce oscillations. Equation (5.133), when minimised, requires a big denominator and a small numerator. The numerator is modest if there are few spatial oscillations in the field pattern, while a large denominator is obtained by concentrating the electric field energy in high- areas. We shall be able to comprehend the band gap origin as well as the field distribution of modes in various types

of photonic crystals with the aid of these heuristic principles for the modes of $\hat{\Theta}$ [129], [133], [134].

5.2.3 Bloch's theorem

For a system with continuous translational symmetry, it remains unchanged by translation through a distance d, $\hat{A}$ represents the continuous translational operator in the y direction and k is the wave vector.

$$\hat{A}e^{iky} = e^{ik(y-d)} = e^{-ikd}e^{iky} \tag{5. 14}$$

So in a homogeneous medium with continuous translational symmetry in all three directions the modes will have the form H(r) = H(r) =$H_0e^{ik.r}$, H_0 is a constant vector. These are plane waves polarized in the direction of H_0.

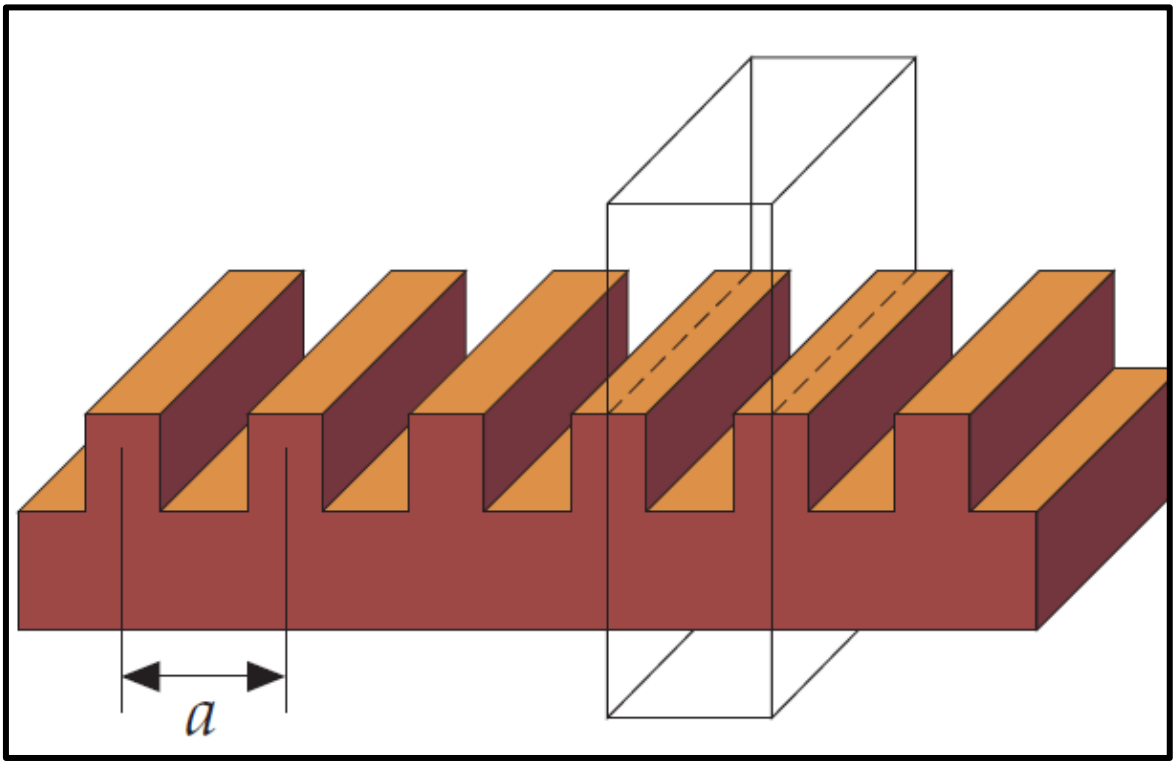

Figure 5.1 Discrete translational symmetry [107]

Photonic crystals have discrete translational symmetry; the system is invariant under translation through distances that are multiple of a basic length, d=la where a is the lattice constant. We have chosen discrete translational symmetry in x direction and continuous translational symmetry in y direction as shown in figure 5.2. $\hat{G}$ represents the discrete translational symmetry then

$$\hat{G}e^{ik_x x} = e^{ik_x(x-la)} = e^{-ik_x la}e^{ik_x x} \tag{5.15}$$

From this equation it can be shown that k_x and $k_x+2\pi/a$ have the same Eigen value. Analogues to crystal physics we call $b=2\pi/a$, x as primitive reciprocal lattice vector. So, in our system the modes will have the form

$$H(r) = e^{ik_x x}e^{ik_y y}u_{k_y}(y,z) \tag{5.16}$$

where u_{ky} is a periodic wavefunction. This discrete periodicity makes the H as the plane wave modulated by periodic function, this is Bloch's theorem. The state with kx and kx + mb are identical where m is an integer. So, we can restrict the eigen value problem in the region $-\pi/a < k_x < \pi/a$ and is known as Brillouin zone. This restriction makes discrete set of eigen values that is labelled by the band index n [135].

5.2.4 Origin of photonic bandgap

By taking into account the electric field mode profiles for the states immediately above and below the gap, the gap's physical origin can be understood. At k=a, which is the boundary of the Brillouin zone, the gap between the bands n=1 and n=2 appears as shown in figure 5.2. The waves' wavelength for k=a is 2a, which is twice the crystal's spatial period (also known as the lattice constant).

A mode of this kind can be centered in one of two ways. The nodes can be placed in either the high or low layers, as shown in figures 5.3 (a) and 5.3 (b), respectively. Any other place would go against the unit cell's symmetry around its center. The high frequency modes have a bigger proportion of their energy in the low frequency areas, whereas the low frequency modes concentrate their energy in the high frequency regions. Given this, it is clear why there is a difference in frequency between the two scenarios. The mode immediately below the gap has a lower frequency than the following band, which has the majority of its energy

in the low dielectric areas as shown in figure 5.3 (d) and more of its energy concentrated in the high dielectric regions as shown in figure 5.3 (c). As a result, there is typically a gap between each set of bands, either at the periphery or the center of the Brillouin zone. For every dielectric contrast, the bandgap always manifests. Energy will be concentrated in a region of low dielectric in the high band and high dielectric in the low band. A band gap is produced by the bands opposite movements [134].

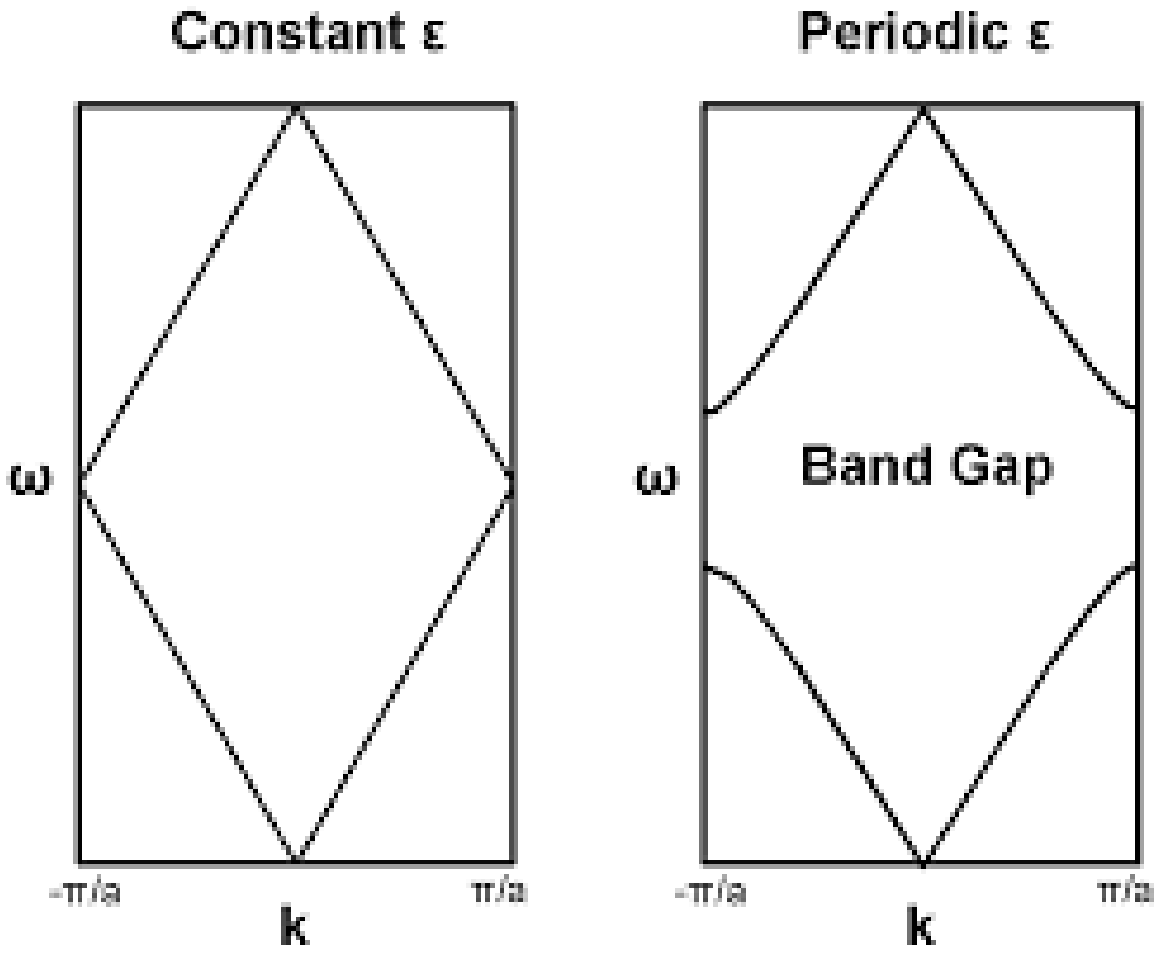

Figure 5.2 Band structure of photonic crystals [107]

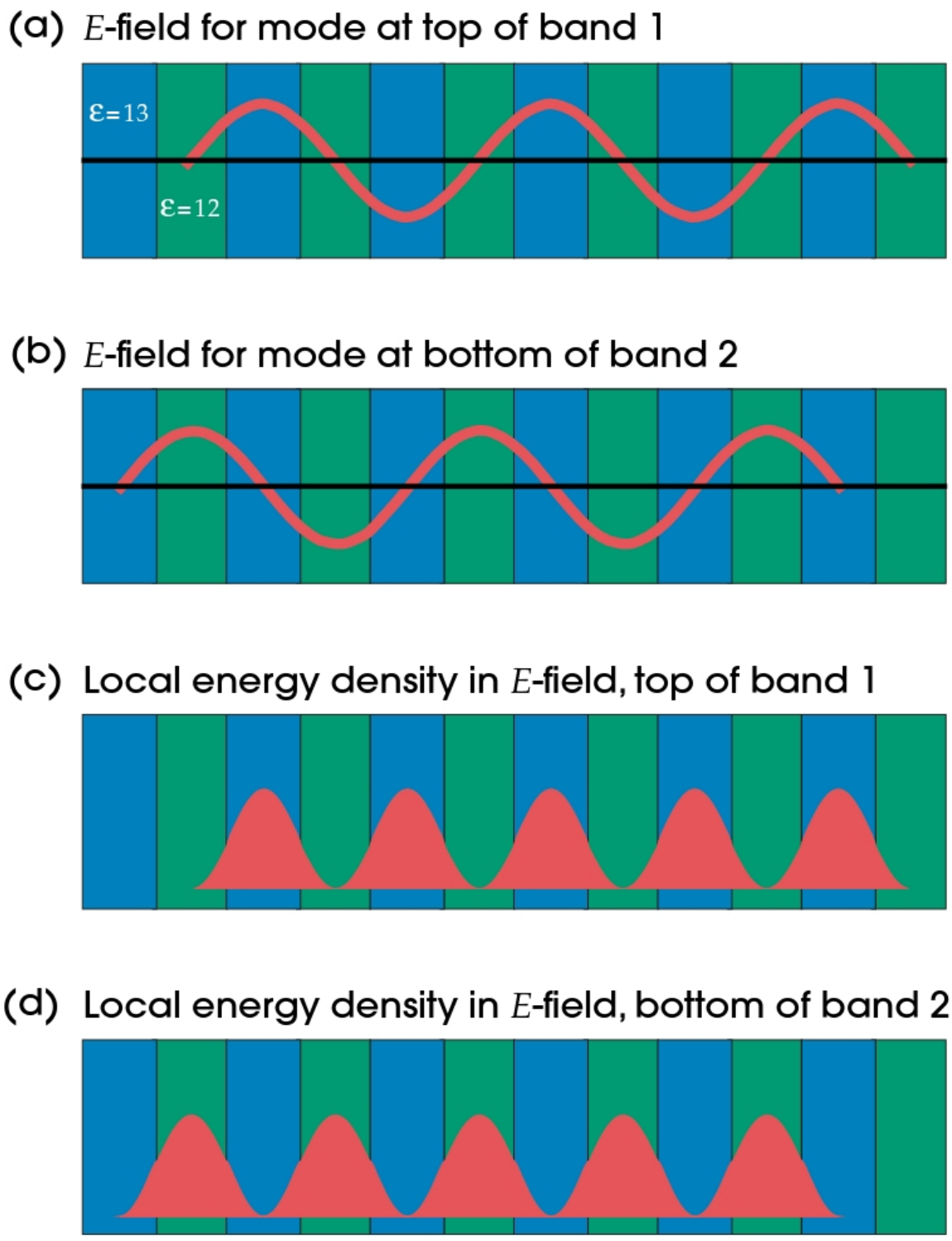

Figure 5.3 Origin of photonic bandgap [107]

5.3 Simulation method

To analyze dielectric structures, particularly photonic crystals, we can employ computational electromagnetic methods. In order to simulate the interaction of electromagnetic fields with a physical environment, computational electromagnetism approximates Maxwell's equations numerically. Prior to fabrication, optical structures like photonic crystals can be planned, simulated, and optimized using computers. The findings of simulations and experiments are frequently quite consistent. These computer techniques allow us to simulate how electromagnetic waves behave in complicated media. We can accomplish this in a number of ways. Each of these approaches begins with the Maxwell's equations and solves them numerically in a different way. Each technique, however, comes with built-in presumptions and limitations. As a result, using one strategy rather than another may be more appropriate for solving some situations. The Frequency Domain technique was employed in this project.

5.3.1 Classification of computational electromagnetism

The three kinds of computational photonics issues include time-domain simulations, frequency-domain eigenproblems, and frequency-domain responses. The following list outlines the unique qualities and restrictions of each category of approaches. In this project, just the first one will be applied.

- *Time Domain Simulations:* By allowing the Maxwell's equations to change over time in a limited computational area, this technique simulates the entire set of time-dependent Maxwell's equations. In what is basically a numerical experiment, the fields E(r, t) and H(r, t) are propagated in time, usually beginning with some time-dependent current source J(r, t). The finite-difference time-domain (FDTD) approach is one particular and widely used method for time-domain simulations.
- *Frequency-Domain Eigenproblems:* By rewriting equation as a finite matrix eigenproblem and employing linear algebraic methods to identify the first few eigenvectors and eigenvalues, band structures (k) and related field patterns can be discovered. The Bloch envelope of the magnetic field, is periodic in periodic dielectric media, necessitating only computation across the finite unit cell. The band structures and eigen fields of photonic crystals can thus be discovered using

frequency-domain eigenproblems, which are effective computational techniques. In general, the band structure (k) and the related fields are discovered by formulating the issue as a finite matrix eigenproblem $Ax = \omega^2 Bx$ and using linear algebraic methods to identify some of the eigenvector x and eigenvalues ω^2.

- *Frequency-Domain Responses:* These methods are based on identifying the fields $E(r)e^{-i\omega t}$ and $H(r)e^{-i\omega t}$ that develop in response to a constant frequency current source, $J(r)e^{-i\omega t}$. This technique allows for the determination of useful physical properties such as transmission and reflection via a finite structure at particular frequencies. Maxwell's equation can be made linear by including currents, which can then be discretized into N unknowns. Then, a N × N matrix equation appears that can be immediately or iteratively solved for the unknown fields. In general, the resulting fields are determined for a given current distribution $J(x)e^{-i\omega t}$ fixed frequency by formulating the issue as a finite matrix equation Ax = b and using linear algebraic methods to solve for x [132].

5.3.2 Finite-difference time-domain methods

Those numerical methods that simulate the entire time-dependent Maxwell equation, propagating the fields in both space and time, are undoubtedly the most broadly applicable for electromagnetism. The finite time difference time domain approach, sometimes known as FDTD, is by far the most popular method for time domain simulations. The FDTD methods provide a finite rectangular grid to divide space and time. The propagation in time, in particular, adopts a leap-frog approach in which the E fields at time are computed from the E fields at time $t-\Delta t$. This method is mainly utilized to compute transmission and reflection spectra. It is able to compute the response of a linear system at many frequencies with a single computation by taking the Fourier transform of the response to a short pulse [136].

5.3.3 MEEP software

With a wide range of applications, the MEEP software package uses the finite-difference time-domain (FDTD) approach to simulate electromagnetics. The letters MEEP stand for MIT electromagnetic equation propagation. Meep can compute lossy resonant modes,

rapidly compute a large number of ω's at once with a single brief pulse, and effectively extract modes from the interior of the spectrum (for example, in a band gap). It also supports metallic and absorbing materials. It can be used to solve a variety of optical issues, including

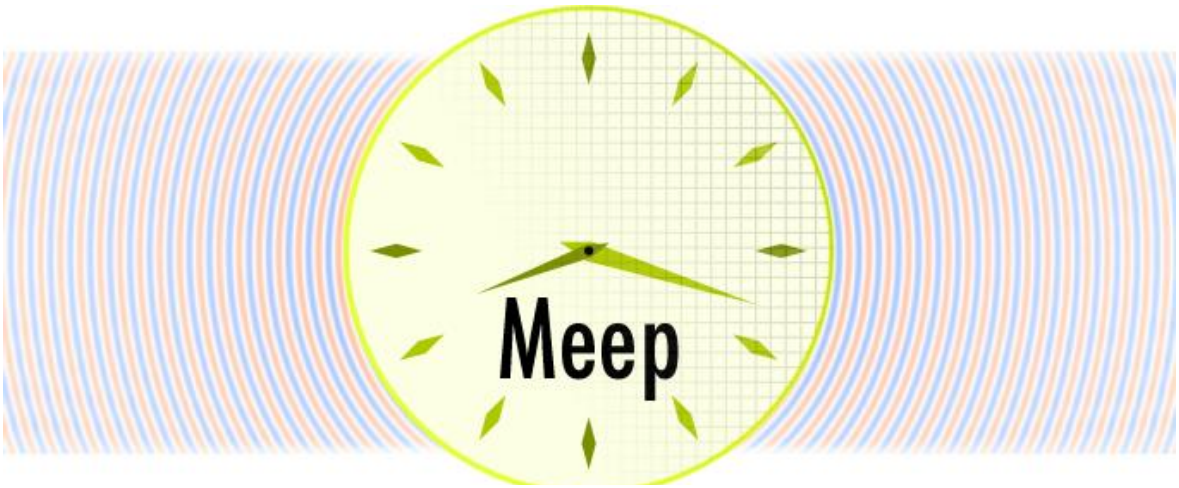

Figure 5.4 Logo of MEEP [105]

those involving waveguides, resonator systems, and photonic crystals. It is Free and open-source software under the GNU GPL with complete scriptability via Python, Scheme, or C++ APIs. The software can be installed in any Unix-like operating system such as Linux, macOS, and FreeBSD [130][137].

Units in MEEP: Meep uses dimensionless units in which constants like ε0, μ0 and c are unity. Practically speaking, the units usually cancel out as for computing quantities such as reflectance/transmittance spectra, resonant/mode frequencies, etc.) is expressed as a ratio. In particular, it is convenient to use scale-invariant units in electromagnetic problems since Maxwell's equations are scale invariant (multiplying all sizes by 10 just divides the corresponding frequencies by 10). This allows one to select a particular length scale that is distinctive of the system, such as a, and utilizing that as the unit of distance. Additionally, since c=1 in Meep units, a (or a/c) also serves as the unit of time. The frequency f in Meep is specifically given in units of c/a (or, alternatively, in units of 2c/a), which is equivalent to expressing f as 1/T: the inverse of the optical period T in units of a/c. Consider expressing a photonic structure, for instance, at infrared frequencies, where it is convenient to describe distances in microns. So, we set a to 1 μm and λ as 1.55 μm ,we define the frequency f as 1/1.55 = 0.6452 [130].

5.3.4 Algorithm

1. Import the required modules from the MEEP repository.
2. Resolution=20
3. Define the parameters of the structure: the lattice constant is 200 nm, dielectric contrast
4. Measure the flux spectrum at one end of the computational cell from a source at the other end
5. Normalize the flux from a case with no dielectric contrast
6. Compute the transmission spectra.
7. The data are extracted
8. plot using matplotlib

Measure the flux spectrum at one end of the computational cell from a source at the other end, normalized by the flux from a case with no index contrast, then compute the transmission spectra. Load the required modules from the MEEP repository. The parameters of the structure are: the thickness of the single layer is 100 nm, and the lattice constant is 200 nm. FDTD simulations can incorporate absorbing boundary conditions using the perfectly matched layer (PML) method. The method involves enclosing the computational cell in a material that, in principle, completely absorbs electromagnetic waves of all frequencies and incidence angles. The source is set to be a typical Gaussian pulse, situated at one edge of the cell just outside the PML. The X and Y axes of the structure have mirror symmetry lines. The mirror symmetry through the Y axis is broken by the source, but the unusual mirror symmetry through the Z axis remains. At the opposite end of the computational cell, before the PML, calculate the flux spectrum [130]. The data are extracted and plotted using matplotlib. The transmission spectra with different dielectric contrasts were plotted, and their effects on the width and position of the photonic bandgap were studied. The spectra for different numbers of layers were also drawn and investigated.

5.4 Results and discussions

MEEP was used to simulate the transmission spectra of multilayers with varying number of layers and refractive index contrast, and the spectra were drawn using Matplotlib. The corresponding images of the layers were also generated using h5topng, which is a utility that converts two-dimensional slices of a database in HDF5 files to Portable Network Graphics (PNG).

5.4.1 Transmission spectra using meep

Varying dielectric contrast: The transmission with the dielectric contrast of the layers from 1 to 5 was plotted and is shown in figure 5.5. Figure 5.6 shows the variation of the width of the bandgap and the position of the bandgap with different dielectric contrast. It was found that as the dielectric contrast of the layers increased, the band gap also increased. Figure 5.7

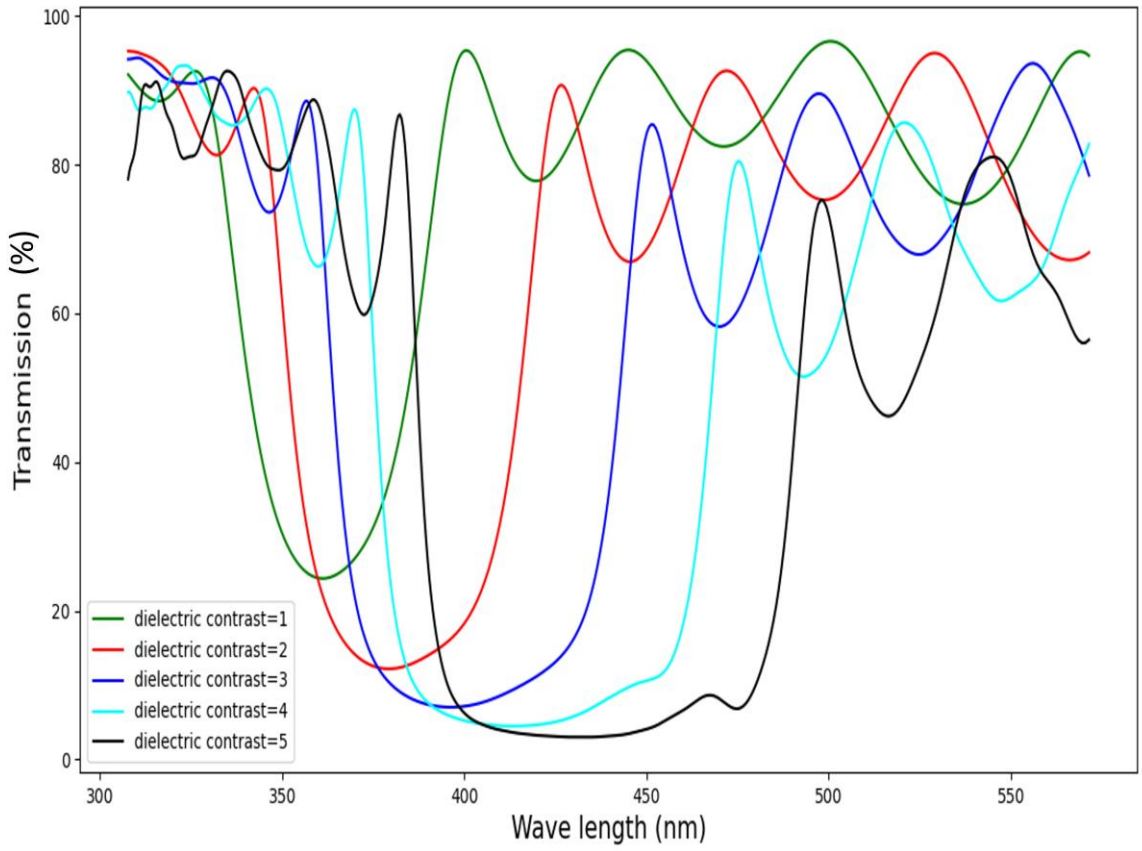

Figure 5.5 Transmission spectra with dielectric contrast varying from 1 to 5.

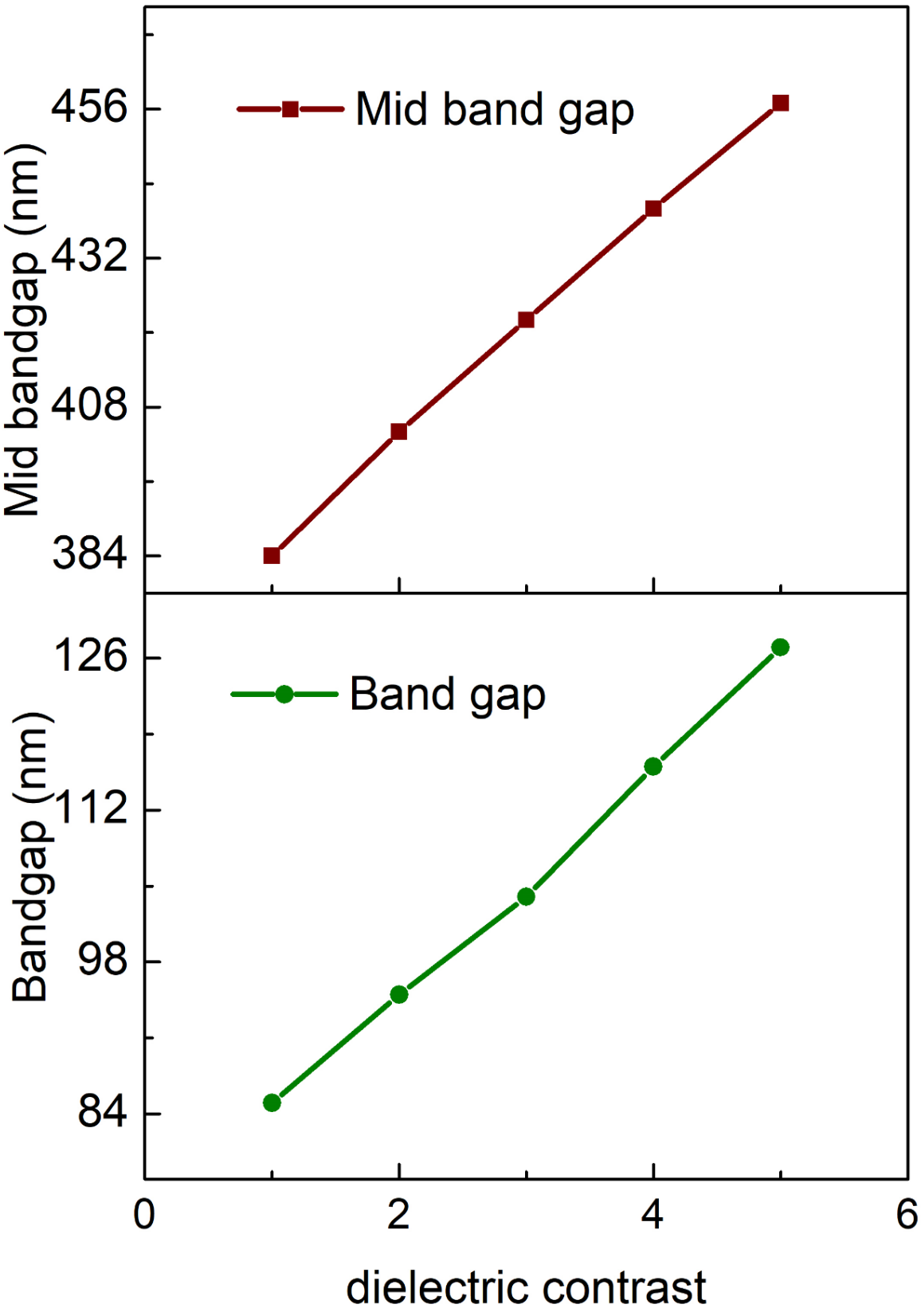

Figure 5.6 Variation of width of bandgap and the midgap with dielectric contrast.

depicts the variation of the transmission percentage with dielectric contrast. Transmission

decreases with increasing dielectric contrast.

The gap develops as a result of the bands' fields being concentrated in various ways, as explained by electromagnetic variational principle. For the first band, the energy is more concentrated in the high dielectric region than in the second. This concentration of energy increases as the dielectric contrast increases, and so, the width of the band gap increases. A shift was also found in the position of the bandgap. It was investigated by plotting the mid-bandgap with dielectric contrast. A red shift in the bandgap position was observed as the dielectric contrast increased. The dielectric contrast may be varied to get the required bandgap, which may be different for different applications [134].

Here, the computational cell produces the bandgap in the visible region. These PC can be utilized as light trapping in solar cells.

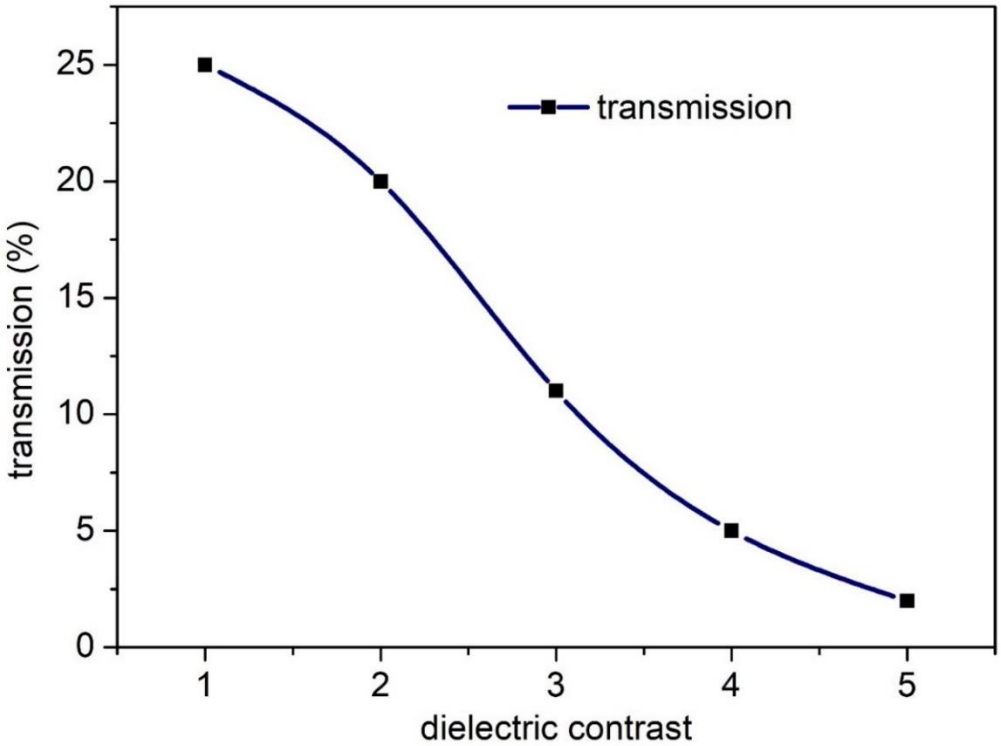

Figure 5.7 Variation of transmission with dielectric contrast

Varying the number of layers: The simulation with of the 1D PC with different number of layers were done. The figure 5.8 shows the computational cell simulated for this study. Figure 5.9 shows the transmission spectra of the multilayers with a varying number of layers and a dielectric contrast of 2

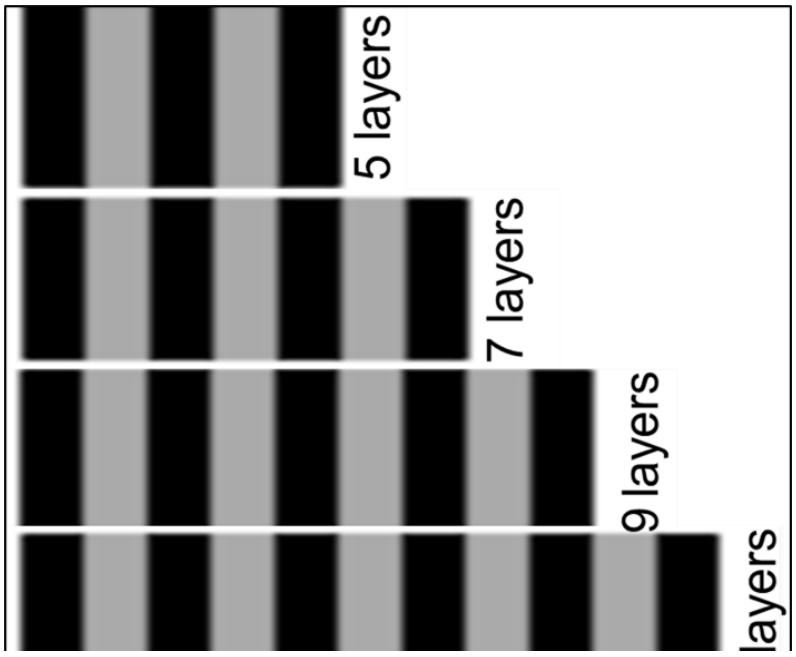

Figure 5.8 Computational cell simulated with different number of layers

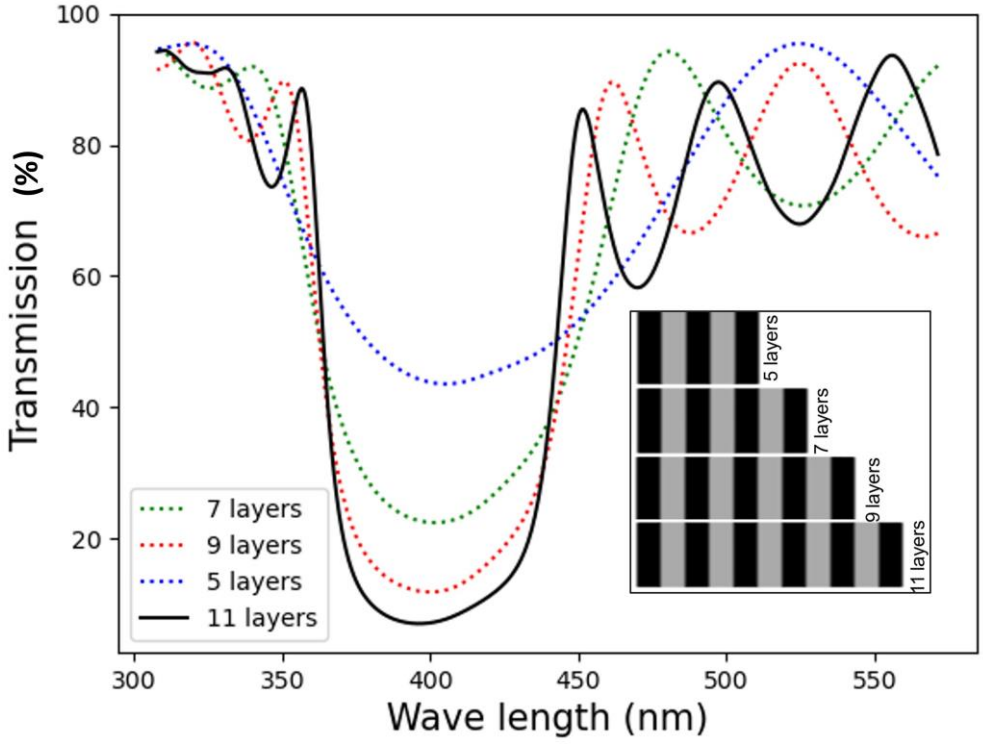

Figure 5.9 Transmission spectra with different number of layers

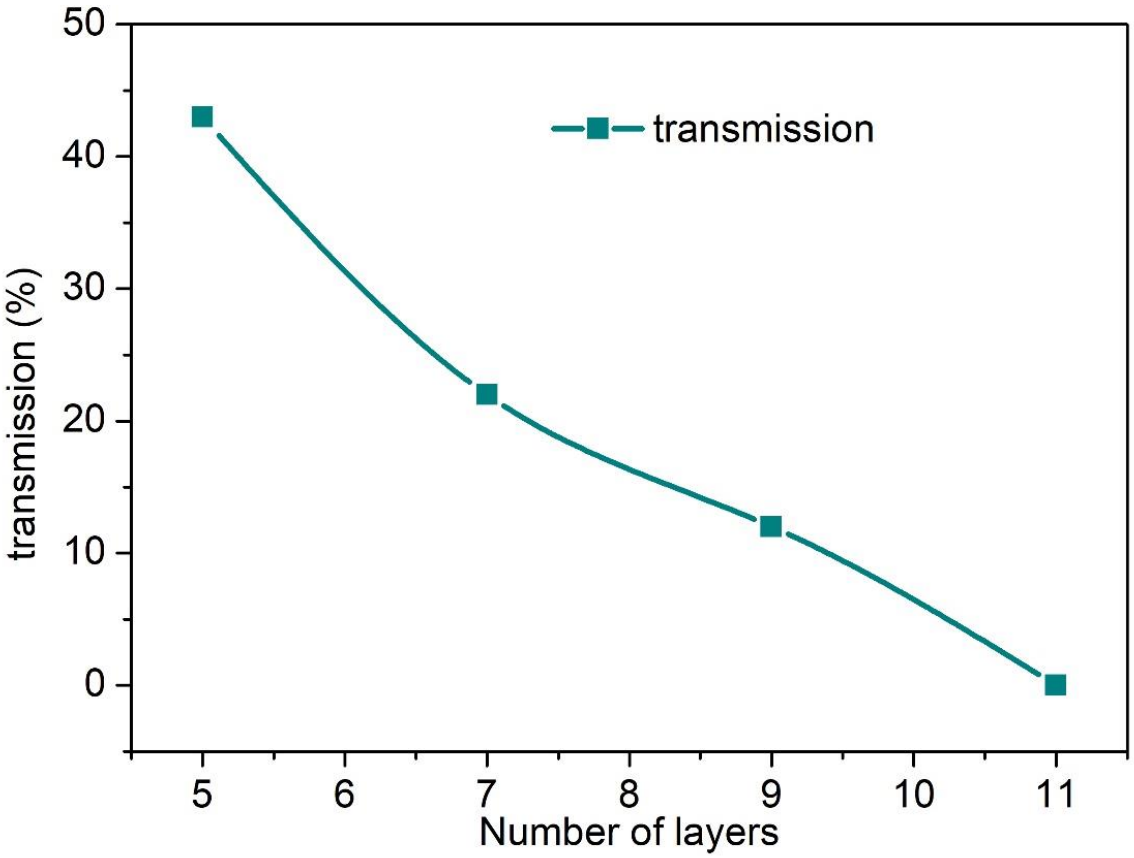

Figure 5.10 Variation of transmission with number of layers

It was found that the position and the width of the bandgap was the same, but the transmission percentage reduced to 43%, 22%, 12%, and nearly 0% as the layers increased from 5 to 11. This shows that 11 layers will produce a sufficient gap in the transmission.

5.5 Conclusion

The 1D photonic crystals with different layers were simulated, and the transmission spectra were plotted using MEEP software. The effect of the dielectric contrast on the width and position of the photonic bandgap was investigated using the simulated transmission spectra. Transmission spectra with different numbers of layers were plotted, and it was found that eleven layers are enough for creating a stop band. We simulated the partial photonic band gap of the photonic crystal. In our work we found that the photonic band gap which can be utilized in a variety of ways in different areas like communication, energy harvesting,

antireflective coatings, light trapping, gas and liquid optical sensing [138] etc. can be varied in a wide way by changing the dielectric contrast of the 1D PC. So before experimentally making the photonic crystals these parameters can be fixed and this will help to get the structure that satisfy the need. This will help to choose a cost-effective material and also saves our time.

Chapter 6

Fabrication of ZnO/SiO_2 1D Photonic crystals

6.1 Introduction

There are different methods to fabricate PC, which include electron beam lithography [139], nanoimprint lithography [75], molecular beam epitaxy [140], chemical vapor deposition (CVD) technology [79], sputtering [141], and holographic exposure of ultraviolet (UV) beams to photosensitive materials [142]. Reactive sputtering has been thought of as a useful technique to deposit high-quality dielectric films of ZnO and SiO_2. Despite its low deposition rate, the sputtering process is simple to control, and the deposited layers exhibit good adhesion and coating uniformity [143]–[146]. The ZnO and SiO_2 films with acceptable optical and structural properties were coated using the RF magnetron sputtering technique. By contrasting these coatings' performances with simulation findings, their effectiveness was assessed. Additionally, reflective coatings made of SiO_2/TiO_2 multi-layers were utilized to enhance the photovoltaic performance of SnS/CdS solar cell.

6.2 ZnO/ SiO_2 multilayers for light trapping in photovoltaic cell

To enhance optical (or surface) performance, a variety of oxide combinations, such as TiO_2/SiO_2, Al_2O_3/SiO_2, ZnO/SiO_2, and ZnO/ZrO_2, are extremely helpful. In solar cells, the highest quantity of light absorption convert is possible by selecting a good combination of anti-reflection coatings materials and synthesis methods. With a gap energy of 3.37 eV, ZnO is a semiconductor metal oxide material that belongs to groups II–VI. It is a cost-effective and sustainable material [147]–[150]. SiO_2 is amorphous, low indexed and has excellent mechanical qualities and high thermal properties. The widespread use of SiO2 is a result of its human and environmental friendliness. Due to their refractive index contrast and easy fabrication process one-dimensional photonic crystals consisting of several layers of zinc oxide and silicon dioxide was done [144], [151]–[153].

6.3 Methods and materials

6.3.1 Quarter wave stack

Several analytical studies for arbitrary dielectric contrast show that the normal incidence gap is maximized when $t_1n_1=t_2n_2$ for two materials with refractive indices ($\sqrt{\varepsilon}$) n_1 and n_2 and thickness t_1 and $t_2=a-t_1$, thickness of the layers respectively. The midgap frequency ω_m in this particular instance may be established to be

$$\omega_m = \frac{n_1+n_2}{4n_1n_2} \cdot \frac{2\pi c}{a} \tag{6.1}$$

Since the matching wavelength $\lambda_m = 2\pi c/\omega_m$ fulfils the relation $\lambda_m,/ n_1=4d_1$ and $\lambda_m,/ n_1=4d_1$ that means each layer is precisely one quarter wavelength thick. This type of layer is referred to as a quarter wave stack for this reason. The waves reflected from each layer are in phase at mid gap frequency of the photonic bandgap, which is why the bandgap is maximized for the quarter wave stack [132], [154].

6.3.2 Simulation of ZnO/SiO_2 1D photonic crystals

As discussed in chapter 5 the simulations of 1D photonic crystals can be done using MEEP software. The simulation work was done with a lattice constant of 200nm. The thickness of the layers was fixed as 100 nm for each layer. As discussed in the above section maximum wavelength will be obtained if the thickness is in the order of one quarter wavelength. In the simulated cell the thickness was chosen as $t_1=t_2=0.5a$. In order to get maximum bandgap, the thickness of one layer should be $t_1=0.2a$ which is equal to 40nm and the other layer as 160 nm. Since we have chosen ZnO and SiO_2 whose dielectric contrast is found to be 4 we have chosen the same for the simulation.

6.3.3 Fabrication of ZnO/ SiO_2 multilayers by sputtering.

Radio frequency (RF) magnetron sputtering was used to coat ZnO and SiO_2 layers from the respective targets with 99.99% purity (procured from Kurt J Lesker, UK). The Hind High Vacuum Model BC-300 RF sputtering device that was used for this project included a mass flow controller (MFC) for the controlled supply of gas. 99.999% pure targets were bought

from Kurt J. Lesker in the UK. An ultrasonically cleaned glass slide was used as a substrate. The sputtering chamber was evacuated to a pressure below 6×10^{-6} mbar before the coating process. Argon was used for sputtering, and the flow rate was maintained at 20 sccm. Argon gas is injected into the chamber using a needle valve to create the plasma. Oxygen (flow rate of 2 sccm) was used to compensate for the loss of oxygen from the targets during the process. The sputtering was done under a constant working pressure of 5×10^{-3} mbars and a high power of 80 W. The ZnO layer was coated first, then SiO_2. The optimal separation between the substrate and the target was 7 cm. With a deposition time of 15 minutes, a 100 nm thick ZnO layer and a 50 nm thick SiO_2 layer were deposited. Eleven alternative layers were coated, and the transmission spectra using UV-visible spectroscopy were analyzed.

6.3.4 Fabrication of SnS/CdS solar cell with 1D photonic crystals

The heterojunction was formed on a thoroughly cleaned ITO substrate. Firstly, the SnS thin film was coated and annealed at 200°C as mentioned in chapter 2, followed by the deposition of CdS. A thin silver contact was drawn above the heterojunction using silver paste. The configuration with (PC/ITO/SnS/CdS/Ag) and without PC (ITO/SnS/CdS/Ag) were analyzed using Keithley source meter.

6.4 Results and discussions

The transmission spectra of the simulated cell is drawn. The films were optically characterized using an Intek UV-vis spectrophotometer. The wavelength used for the characterization was in the range of 190 nm to 1190 nm. Deuterium was used as the source for UV and tungsten for visible radiation. The cross-sectional view of the films was obtained using a FESEM (Field Emission Scanning Electron Microscope) (SUPRA 55 VP-4132 Carl Zeiss).

6.4.1 Transmission spectra of simulated ZnO/SiO_2 photonic crystals

Figure 6.2 depicts the transmission spectra and the inset of the figure shows the corresponding computational cell. From the spectra it was found that the width of the bandgap increased and the transmission percentage decreased when compared with those with thickness $t_1=t_2=0.5a$. The mid band gap position was again in the violet blue region.

The values of mid band gap region, width of the band gap and the transmission percentage is tabulated in table 6.1.

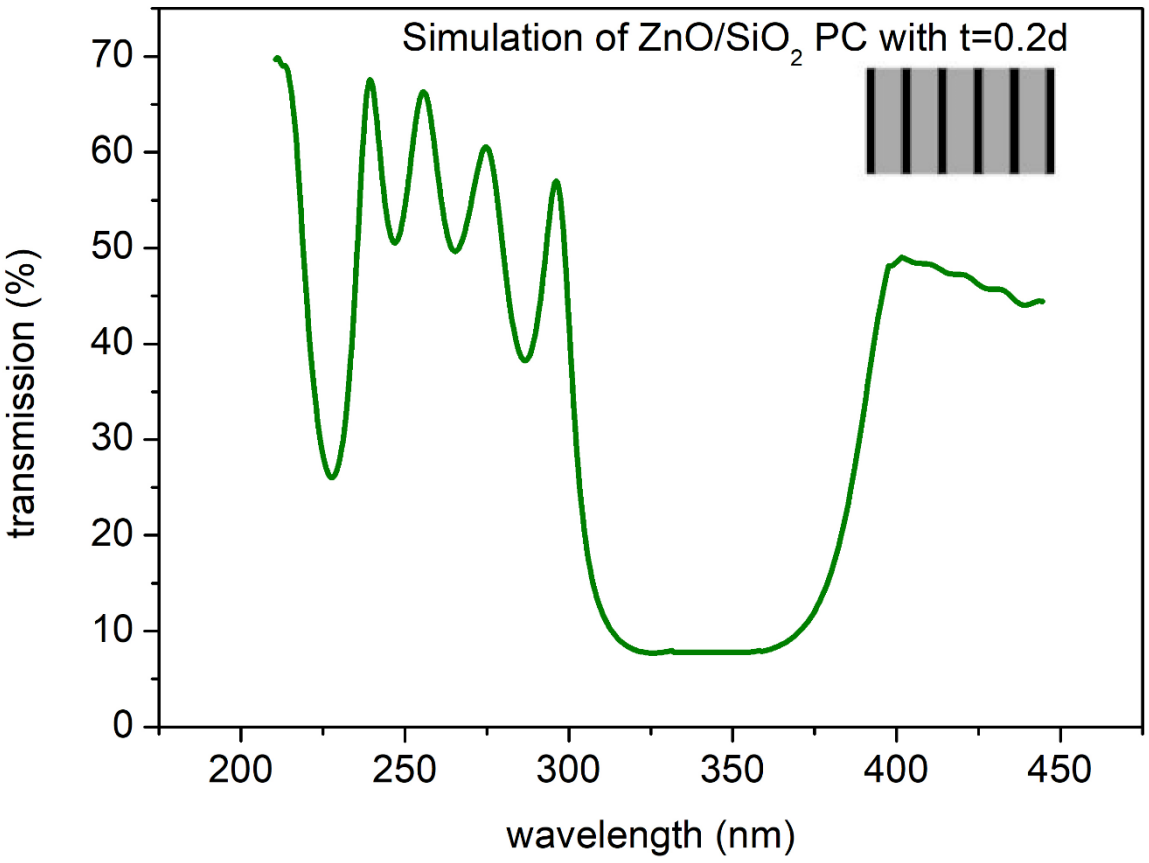

Figure 6.1 Transmission spectra of simulated ZnO/SiO2 1D photonic crystals

6.4.2 Optical properties using UV visible spectroscopy

ZnO and SiO_2 thin films prepared by the sputtering method were optically characterized by UV-visible spectroscopy. The absorption spectra were drawn, and the optical bandgap and refractive index were calculated using the tauc relation and Fresnel's equation, respectively.

Absorption spectra tauc plot: Figures 3 and 4 show the absorption spectra (inset) and tau plot of ZnO and SiO_2 thin films prepared by sputtering. The region with a lower wavelength, less than 400 nm, shows the maximum absorption, and the spectra region that lies in a longer wavelength, i.e., in the visible region, shows high transparency for both ZnO and SiO_2. The absorption edge of SiO_2 rises at a lower wavelength compared to ZnO.

.

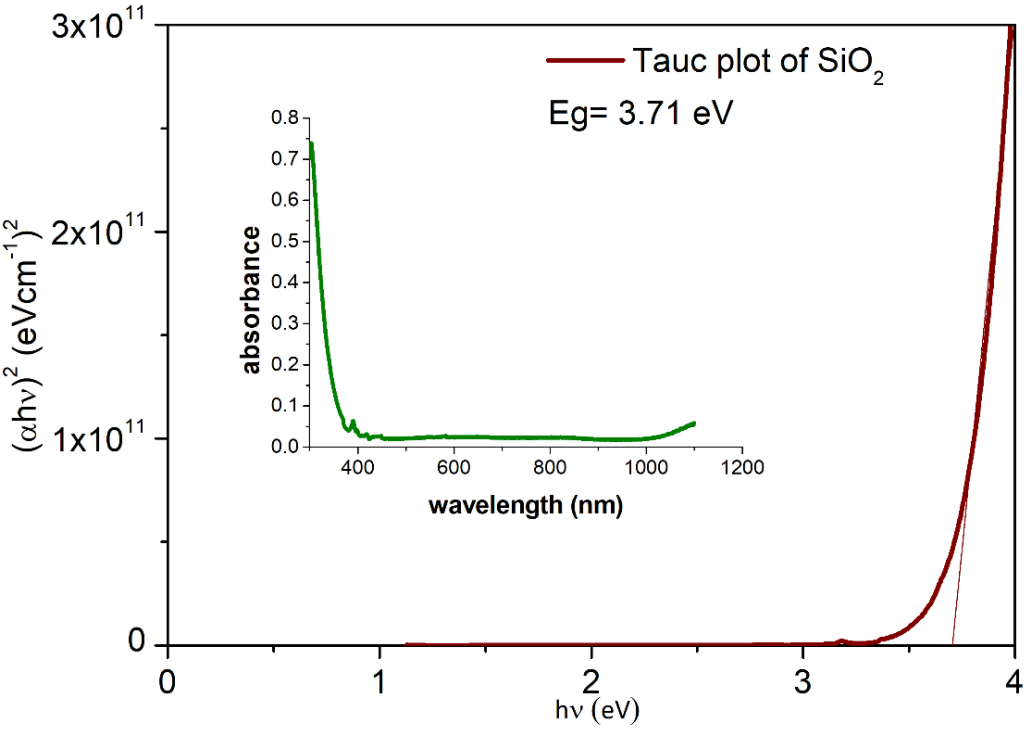

Figure 6.2 Absorption spectra (inset) and Tauc plots of SiO_2 films

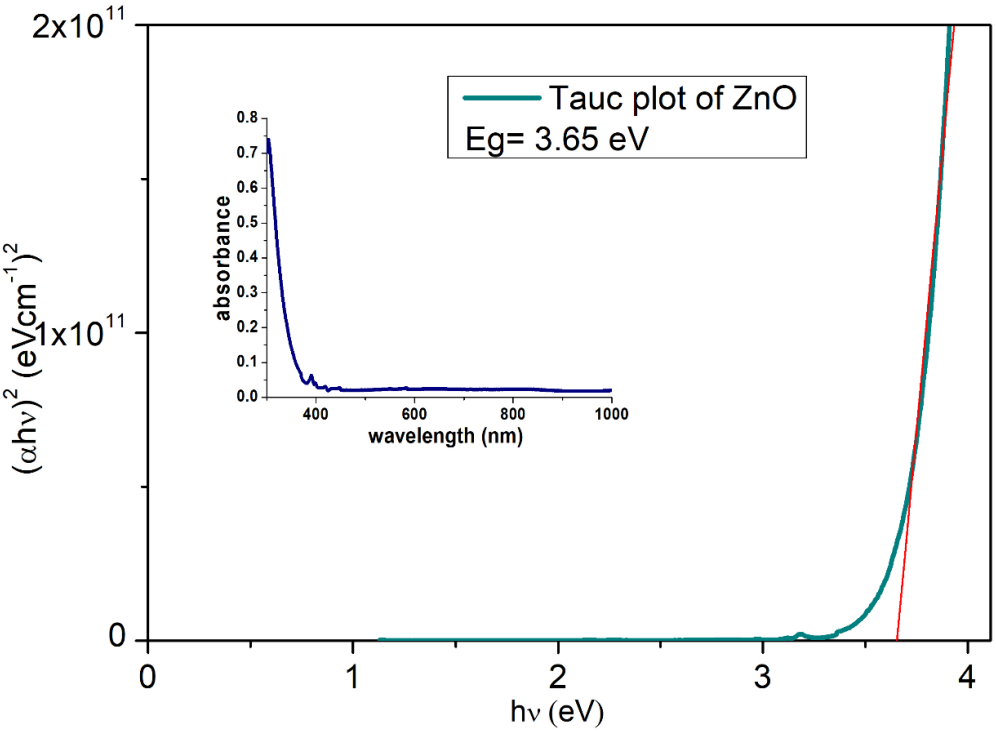

Figure 6.3 Absorption spectra (inset) and Tauc plots of ZnO film

Tauc plot: The optical band gaps of ZnO and SiO_2 were determined using the tauc relation. The Tauc plot is drawn with hυ on the x axis and $(\alpha h\upsilon)^2$ on the y axis. The linear part of the curve's shape suggests that the material has a direct optical transition. By extending the straight line of the image to the energy axis, it is possible to calculate the energy band gap. The energy gap of the ZnO film was found to be 3.61 eV and that of SiO_2 at 3.75 eV. These results show that prepared SiO_2 thin film is much more transparent with a larger optical band gap when compared to ZnO. Both the films were transparent to the visible region

Determination of refractive index: The refractive indices have been discovered to significantly affect both the electrical and optical characteristics of the materials.

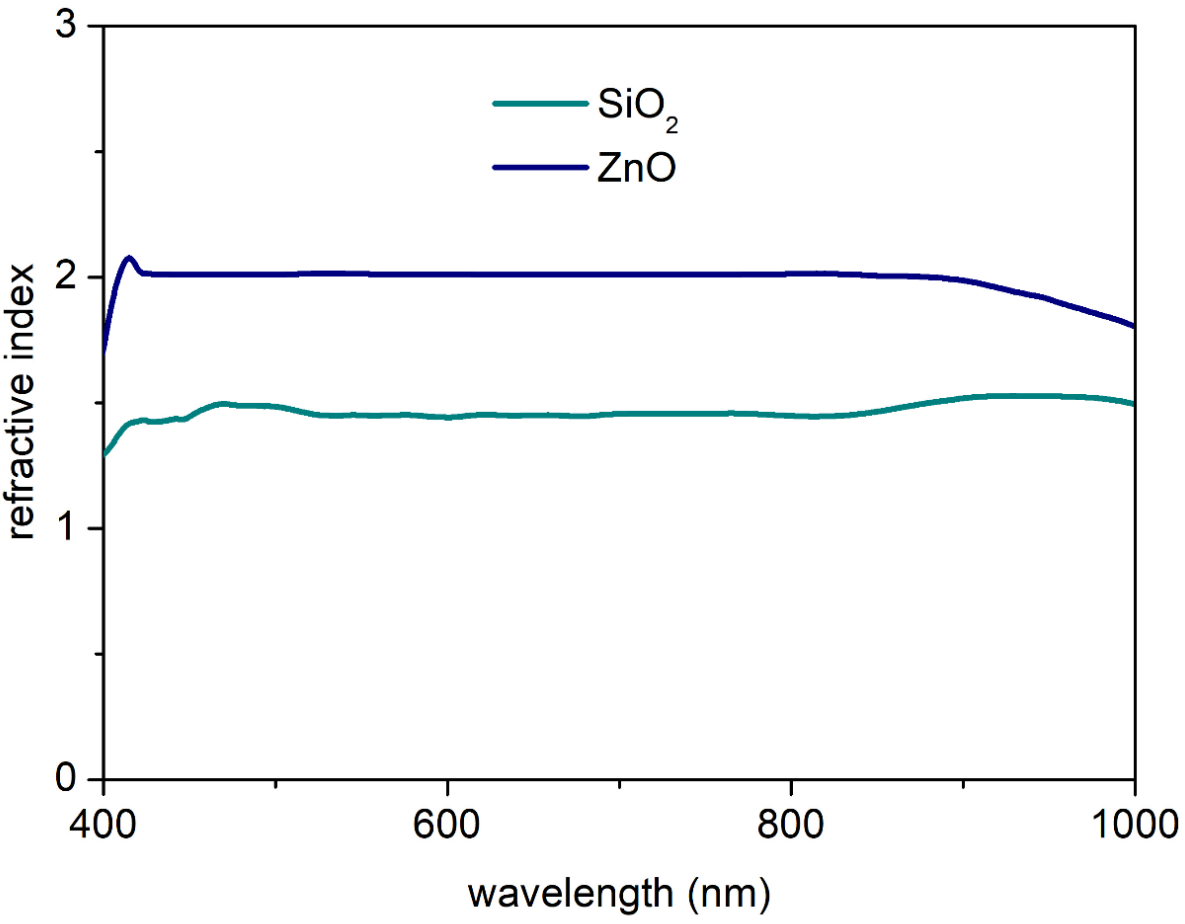

Figure 6.4 Refractive index of SiO_2 and ZnO in the visible region.

Equation 5.1 has been used to compute the refractive index, and equation 6 has been used to calculate the reflectance as a function of wavelength using the transmittance data.

$$n = \frac{1+\sqrt{R}}{1-\sqrt{R}} \quad 6.2$$

$$R = (1 - \sqrt{(Texp(A))} \quad 6.3$$

In Figure 6.4, the change in refractive index as a function of photon wavelength has been calculated and plotted [147].

The refractive indices for ZnO and SiO_2 are 2 and 1.47 at high wavelengths (>400 nm, respectively) which matched with reported values. In the visible region, the dielectric constant is equal to the square of the refractive index. So, it is approximately equal to 4 and 2 for ZnO and SiO_2. The 1D PC fabricated has a dielectric contrast of 2.

The transmission spectra of 1D PC: Figure 5 shows the transmission spectra of the fabricated PC with 11 alternate layers of ZnO and SiO_2

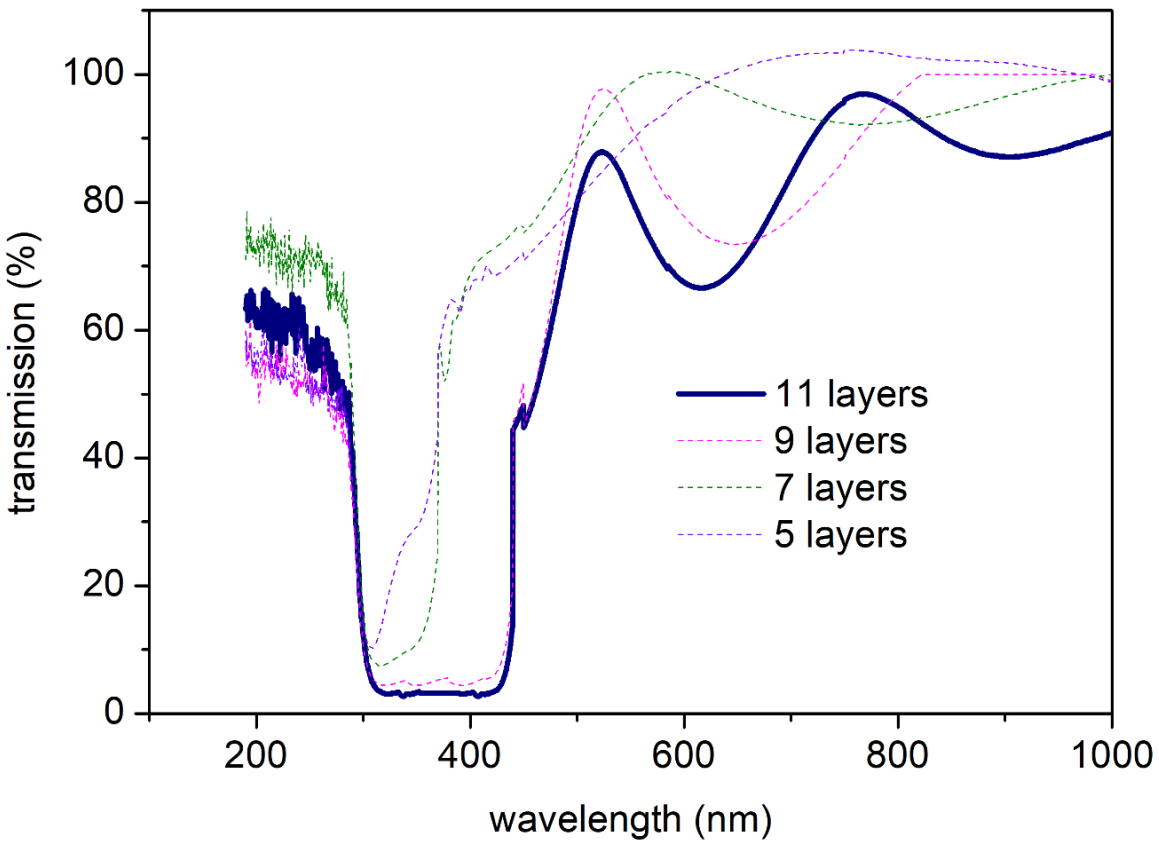

Figure 6.5 Transmission spectra of ZnO/SiO_2 1 D photonic crystals

The range of the band gap was as predicted by the simulation for the dielectric contrast of 2 and 11 layers. It was in the violet range with a band gap of 130 nm. The simulation helped as a pre-laboratory for choosing the material and the number of layers.

Table 6.1 Comparison of photonic band gap

	Transmission (%)	Mid bandgap (nm)	Bandgap (nm)
Simulated 1D PC $t_1=t_2=100$ nm	20	404	86
Simulated 1D PC $t_1=40$ nm $t_2=160$ nm	6	344	103
Fabricated ZnO/SiO_2 1D PC	2	368	130

6.4.3 FESEM analysis

The cross- sectional view of the 11 alternate layers of ZnO/SiO_2 was taken using FESEM and is displayed in figure 6.6. The micrograph is displayed in figure 6.6. The thickness of ZnO layer was found to be nearly 40 nm and SiO_2 as 160 nm. The lattice constant measured was 200 nm

6.5 I-V characterization

The final step was creating a SnS-based solar cell using commercial ITO (Indium Tin Oxide) as the front contact, CdS as an n-type semiconductor, SnS as a p-type semiconductor, and silver as the back contact (ITO/PC/SnS/CdS/Ag). Figure 6.7 displays I-V characterization of the heterojunction. The cell parameters with PC and without PC that was discussed in chapter 4 are tabulated in table 6.2. From the table it is cleared that the cell parameters improved a lot by incorporating the PC structures. So, in solar cell systems, light trapping is

essential to improve light confinement and absorption. Reducing optical losses, light trapping had great success in enhancing the efficiency of the solar cell.

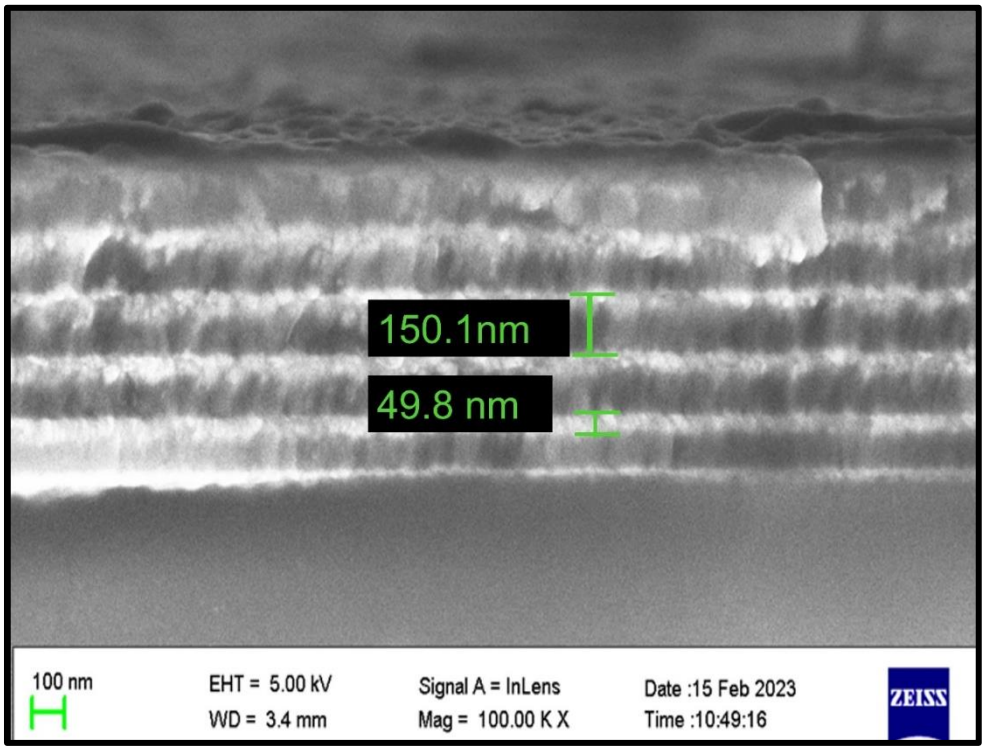

Figure 6.7 Cross sectional view of 11 layers of 1D PC

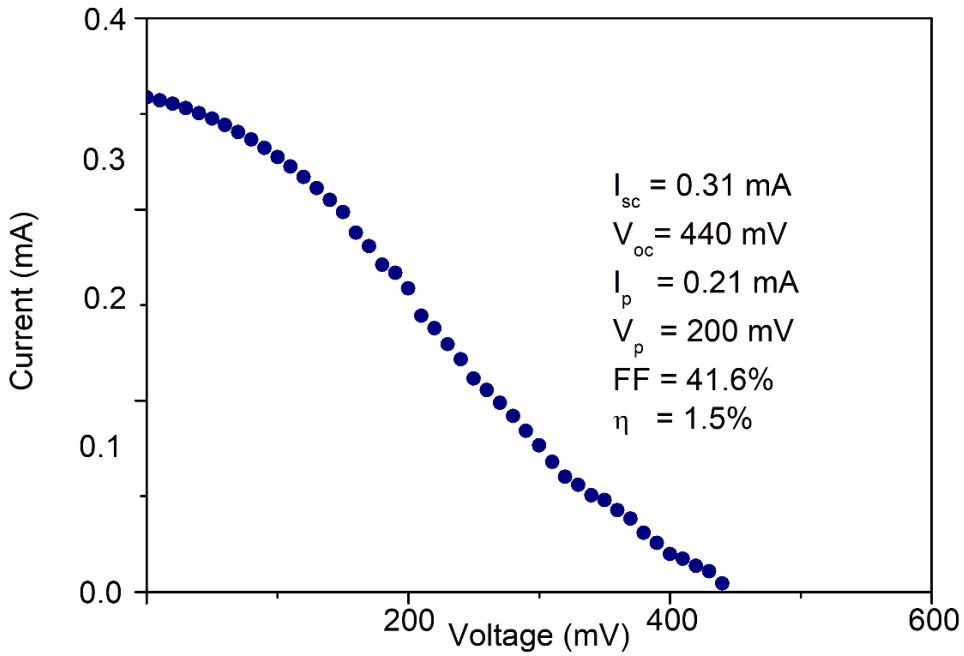

Figure 6.6 IV characteristics of (ITO/PC/SnS/CdS/Ag) solar cell

Table 6.2 Cell parameters of SnS based solar cell with and without PC

	V_p (mV)	I_p (mA)	V_{oc} (mV)	I_{sc} (mA)	FF (%)	Efficiency (%)
Without PC	190	0.0013	435	0.0024	28.5	0.01
With PC	200	0.21	440	0.31	41.6	1.5

6.6 Conclusion

After the simulation work, ZnO/ SiO_2 PC with 11 layers was fabricated, and the transmission spectra was investigated. The results were comparable with the simulations. Photonic bandgap has numerous applications in fields like communication, energy harvesting, antireflective coatings, light trapping, gas and liquid optical detection, and more. The position and the width of these gaps can be tuned to fit the application by changing the dielectric contrast. The simulation helped as a pre laboratory for choosing the material and the number of layers, and this will save time and money. The (ITO/PC/SnS/CdS/Ag) heterojunction was fabricated and the cell parameters with and without PC were compared. It was observed that the performance of the solar cell improved by using 1D PC as back reflectors

Chapter 7

Overall Summary and Recommendations

7.1 Overall summary

One of the most promising and environmentally friendly energy sources, solar energy, is the subject of extensive research. Due to their low manufacturing costs, high-throughput processing techniques, and ease of junction formation, thin film-based solar cells offer a wide range of applications. As a potential absorber material for solar cells, orthorhombic tin monosulfide (SnS), which is abundant on Earth and nontoxic has ideal electronic properties such as an ideal bandgap (~1.3 eV), a high optical absorption coefficient of 10^4 cm^{-1}, and intrinsic p-type conductivity, has attracted a lot of interest. Even though theoretical studies and simulations shows a conversion efficiency of more than 20% for SnS based solar cell, power conversion efficiency (η) of SnS-based solar cells remained below 4%. There have been numerous attempts to increase the effectiveness of SnS solar cells. The main challenges to improving the efficiency of SnS-based solar cells are the production of high-quality SnS thin films and selecting the appropriate n-type semiconductor. This was tried in this work. CdS, a semiconductor with a bulk bandgap of 2.42 eV, is a promising window layer material used in both commercial modules and lab research.

The creation of photon management techniques to maximize light absorption for applications like solar cells, photo electrochemistry, and sensing has received a lot of attention in recent years. Photonic crystals, which are considered the optical analogue of crystals, are capable of controlling the flow of light. In this work, 1D photonic crystals were simulated using MEEP software, which is free and open software. The effect of dielectric contrast and the number of layers on the photonic band gap was investigated. ZnO/SiO_2 1D photonic crystals were fabricated by sputtering. The experimental results matched the simulations. It is always better to have simulation as a pre-laboratory, as it saves time and money.

This thesis reports on possibility of modification of the properties and photovoltaic performance of chemically prepared SnS thin film by changing the pH of the bath solution and annealing temperature. A further enhancement of efficiency was obtained using the SiO_2/ZnO 1D Photonic crystals for light trapping. Simulation work was done as the pre laboratory.

SnS and CdS thin films were synthesized chemically for different pH values of bath solutions. The optimal pH values for SnS film formation were 9.8, 9.9, and 10, while the pH values for CdS were 11.3, 11.4, and 11.5. Film formation did not take place outside this pH range at ambient conditions. The structural, morphological, optical, and chemical characterization revealed changes in the thin film properties with the pH variation. Structural analysis showed an increase in crystallite size for SnS and CdS as the pH of the solution increased. The optical band gap was found to decrease as the pH of the solution increased for both materials. Morphological studies showed that the film became more continuous and uniform as the pH of the bath solution increased. The atomic weight percentage of metal increased as the pH increased, according to the EDS spectra of both films. Photovoltaic cells were fabricated with an ITO/SnS/CdS/Ag configuration, where the SnS thin film deposited at pH = 10 and the CdS film deposited at pH = 11.3 showed better performance. It was observed that the pH of the bath solution has an effect on the efficiency of the photovoltaic cell. Even though, the cell performance of the fabricated heterojunction was poor, the successful formation of the p-n junction was confirmed. However, SnS thin films are potential candidates for solar cells, and trials can be made to improve the solar cell's performance by optimizing the cell configuration.

The chemically created SnS thin films were subjected to various annealing temperatures. The ideal annealing temperature for SnS was determined to be 200°C. No peaks were visible in the films' annealed at 250°C XRD or Raman spectra. The structural, morphological, optical, and chemical characterization demonstrated that variations in the annealing temperature led to modifications in the thin film properties. The films' crystallite size grew as the annealing temperature rose, according to structural analyses. It was discovered that when the annealing solution's temperature rose, the optical band gap shrank. With annealing, morphological tests revealed that the film became denser and the needle-shaped morphology changed to a plate-shaped one, increasing the grain size. The atomic weight percentage of

sulphur dropped as the annealing temperature rose, according to EDS spectra. ITO/SnS/CdS/Ag configuration were employed in the construction of photovoltaic cells, and a thin SnS film that had been annealed at 200°C served as the absorber layer. The efficiency of the solar cell was found to be impacted by the annealing of the film. An increase in efficiency was seen by annealing the SnS thin film. This technique is an inexpensive way to produce SnS thin films for the absorber layer of solar cells.

Modern advanced electronic, optoelectronic, and photonic devices are in demand for multilayer thin film structures, which are also considered as 1D photonic crystals. Photonic crystals are considered the optical analogue of crystals, in which atoms are replaced by macroscopic periodic dielectric structures. It is preferable to optimize the PC's design on the computer before building it. They are favorable for computation because the length scales are not too small, and the Maxwell equations that govern the propagation of electromagnetic radiation through the PC are practically exact. The software called MEEP were used for computing transmission spectra. Meep implements FDTD method. This is a widely used technique in which space and time are divided into a discrete grid and the derivatives of the Maxwell equation are approximated using discrete time steps. This approach can imitate many real-world issues almost identically since it gets closer and closer to the true continuous equations as the grid and time increments are made finer and finer. The 1D photonic crystals with different layers were simulated, and the transmission spectra were plotted using MEEP software. The effect of the dielectric contrast on the width and position of the photonic bandgap was investigated using the simulated transmission spectra. Transmission spectra with different numbers of layers were plotted, and it was found that eleven layers are enough for creating a stop band.

Reactive sputtering has been thought of as a useful technique to deposit high-quality dielectric films of ZnO and SiO_2. Despite its low deposition rate, the sputtering process is simple to control, and the deposited layers exhibit good adhesion and coating uniformity [143]–[146]. The ZnO and SiO_2 films with acceptable optical and structural properties were coated using the RF magnetron sputtering technique. After the simulation work, ZnO/ SiO_2 PC with 11 layers was fabricated, and the transmission spectra was investigated. The results were comparable with the simulations. Photonic bandgap has numerous applications in fields like communication, energy harvesting, antireflective coatings, light trapping, gas and liquid

optical detection, and more. The position and the width of these gaps can be tuned to fit the application by changing the dielectric contrast. The simulation helped as a pre laboratory for choosing the material and the number of layers, and this will save time and money.

The SnS based solar cell were fabricated with the ZnO/$SiO_2$1D PC as anti-reflective coating. It was found that the efficiency of the solar cell improved a lot when compared to those without the PC. Even though the efficiency reported in this work is below the maximum reported efficiency of SnS based solar cell, this work gives a simple and cost-effective method of fabricating the cell. It also shows that the efficiency of the solar cell can be improved by using 1D PC.

7.2 Recommendations

Further improvement of the efficiency is required to make the fabricated cell to put into the industry. The efficiency can be improved by decreasing the resistance of the layers. For that doping the layers with metals especially silver can be tried. Also, different possible applications of SnS thin films can be exploited such as photosensors. Combinations with different n-type materials like ZnO, ZnS, etc. can be tried in a way to enhance the efficiency of the solar cell. Different wave guiding strategies can be utilized as anti-reflective coatings in front of the cell.

Over the past decade, a tremendous development has taken place within the area of optical components having a full or partly periodic structure incorporated. A small amount of disorder will not destroy the PBG but will allow localized modes to exist within the gap, which can be utilised for wave guiding. Such PC can be utilized as anti-reflective coatings that guide the solar radiation into the junction without any loss. This disorder can be incorporated either by changing the thickness or dielectric contrast of a single layer. The disorder can be incorporated into ZnO/SiO_2 1D photonic crystals either by replacing a layer with a different material like TiO_2 or by changing the thickness of a layer.

Two-dimensional photonic crystals called photonic-crystal fibers are used for fiber-optic communication, among other applications. Three-dimensional crystals may one day be used in optical computers, and could lead to more efficient photovoltaic cells. This new class of optical waveguides is characterized by a carefully engineered cross-section of glass (or

polymer) riddled with a pattern of miniature holes. The future work and recommendations provide work plan to support and sustain the research work with a sole aim to develop innovative and potentially efficient SnS based devices along with the fabrication of photonic crystals for light harvesting and optical communication application.

Chapter 7

References

[1] Y. Song, “Introduction: Progress of Thin Films and Coatings,” *Inorg. Org. Thin Film.*, pp. 1–58, 2021, doi: 10.1002/9783527344987.ch1.

[2] J. T. Gudmundsson, “Physics and technology of magnetron sputtering discharges,” *Plasma Sources Sci. Technol.*, vol. 29, no. 11, 2020, doi: 10.1088/1361-6595/abb7bd.

[3] G. H. Yue *et al.*, “The effect of anneal temperature on physical properties of SnS films,” *J. Alloys Compd.*, vol. 474, no. 1–2, pp. 445–449, 2009, doi: 10.1016/j.jallcom.2008.06.105.

[4] D. Sun *et al.*, “Thin Film Deposition Techniques in Surface Engineering Strategies for Advanced Lithium-Ion Batteries,” *Coatings*, vol. 13, no. 3, p. 505, 2023, doi: 10.3390/coatings13030505.

[5] T. Osaka and T. Homma, “Thin films,” *Electrochem. Soc. Interface*, vol. 4, no. 2, pp. 42–46, 1995, doi: 10.1364/oam.1993.wf.1.

[6] D. R. Eman and A. Gaml, “Introduction To Thin Films Laboratory Lecturer of Experimental Physics,” pp. 1–22.

[7] K. Navrátil, J. Šik, J. Humlíček, and S. Nešpůrek, “Optical properties of thin films of poly(methyl-phenylsilylene),” *Opt. Mater. (Amst).*, vol. 12, no. 1, pp. 105–113, 1999, doi: 10.1016/S0925-3467(98)00055-X.

[8] M. C. RAO and M. S. SHEKHAWAT, “a Brief Survey on Basic Properties of Thin Films for Device Application,” *Int. J. Mod. Phys. Conf. Ser.*, vol. 22, pp. 576–582, 2013, doi: 10.1142/s2010194513010696.

[9] R. Messier, “Thin Film Deposition Processes,” *MRS Bull.*, vol. 13, no. 11, pp. 18–21, 1988, doi: 10.1557/S0883769400063879.

[10] F. Thickness, “4 . Properties and Characterization of Thin Films,” pp. 75–143.

References

[11] K. Vijayan, S. P. Vijayachamundeeswari, K. Sivaperuman, N. Ahsan, T. Logu, and Y. Okada, “A review on advancements, challenges, and prospective of copper and non-copper based thin-film solar cells using facile spray pyrolysis technique,” *Sol. Energy*, vol. 234, no. March, pp. 81–102, 2022, doi: 10.1016/j.solener.2022.01.070.

[12] N. Singh and A. Goswami, “Study of PV and IV characteristics of solar cell in MATLAB/Simulink,” *Int. J. Pure Appl. Math*, vol. 118, no. 24, p. 24, 2018.

[13] J. A. Andrade-Arvizu, M. Courel-Piedrahita, and O. Vigil-Galán, “SnS-based thin film solar cells: perspectives over the last 25 years,” *J. Mater. Sci. Mater. Electron.*, vol. 26, no. 7, pp. 4541–4556, 2015, doi: 10.1007/s10854-015-3050-z.

[14] Vinod, R. Kumar, and S. K. Singh, “Solar photovoltaic modeling and simulation: As a renewable energy solution,” *Energy Reports*, vol. 4, pp. 701–712, 2018, doi: 10.1016/j.egyr.2018.09.008.

[15] I. Purohit, P. Purohit, and S. Shekhar, “Evaluating the potential of concentrating solar power generation in Northwestern India,” *Energy Policy*, vol. 62, no. April 2019, pp. 157–175, 2013, doi: 10.1016/j.enpol.2013.06.069.

[16] Ajibade FO *et al.*, “Status, Trend and Potential Generation of Renewable Energy From Waste for Sustainable Development in Africa: an Overview,” no. July, pp. 11–13, 2017.

[17] M. Victoria *et al.*, “Solar photovoltaics is ready to power a sustainable future,” *Joule*, vol. 5, no. 5, pp. 1041–1056, 2021, doi: 10.1016/j.joule.2021.03.005.

[18] T. W. Principle and S. Cell, “The Working Principle of a Solar Cell,” *Sol. Energy*, vol. 1, pp. 21–24, 1921.

[19] N. Guerra, M. Guevara, C. Palacios, and F. Crupi, “Operation and physics of photovoltaic solar cells: an overview,” *I+D Tecnológico*, vol. 14, no. 2, pp. 84–95, 2018, doi: 10.33412/idt.v14.2.2077.

[20] S. L. Tripathi, S. Saxena, and S. Kumari, “A Review on Design and Performance Evaluation of Solar Cells and Panels,” *Think India J.*, vol. 22, no. May, pp. 2786–

2796, 2019.

[21] L. M. Torres-Martínez, O. V. Kharissova, and B. I. Kharisov, “Handbook of ecomaterials,” *Handb. Ecomater.*, vol. 1, no. June, pp. 1–3773, 2019, doi: 10.1007/978-3-319-68255-6.

[22] J. Pastuszak and P. Węgierek, “Photovoltaic Cell Generations and Current Research Directions for Their Development,” *Materials (Basel).*, vol. 15, no. 16, 2022, doi: 10.3390/ma15165542.

[23] A. S. Al-Ezzi and M. N. M. Ansari, “Photovoltaic Solar Cells: A Review,” *Appl. Syst. Innov.*, vol. 5, no. 4, pp. 1–17, 2022, doi: 10.3390/asi5040067.

[24] A. H. M. Smets, K. Jäger, O. Isabella, R. A. van Swaaij, and M. Zeman, “Solar Cell Parameters and Equivalent Circuit,” *Sol. energy Phys. Eng. Photovolt. conversion, Technol. Syst.*, pp. 113–121, 2016, [Online]. Available: https://ocw.tudelft.nl/wp-content/uploads/solar_energy_section_9_1_9_3.pdf

[25] M. H. El-Ahmar, A. H. M. El-Sayed, and A. M. Hemeida, “Mathematical modeling of Photovoltaic module and evalute the effect of varoius paramenters on its performance,” *2016 18th Int. Middle-East Power Syst. Conf. MEPCON 2016 - Proc.*, no. January 2018, pp. 741–746, 2017, doi: 10.1109/MEPCON.2016.7836976.

[26] W. Charfi, M. Chaabane, H. Mhiri, and P. Bournot, “Performance evaluation of a solar photovoltaic system,” *Energy Reports*, vol. 4, pp. 400–406, 2018, doi: 10.1016/j.egyr.2018.06.004.

[27] T. Dittrich, “Basic Characteristics and Characterization of Solar Cells,” *Mater. Concepts Sol. Cells*, pp. 3–43, 2018, doi: 10.1142/9781786344496_0001.

[28] D. J. Lewis, P. Kevin, O. Bakr, C. A. Muryn, M. A. Malik, and P. O’Brien, “Routes to tin chalcogenide materials as thin films or nanoparticles: a potentially important class of semiconductor for sustainable solar energy conversion,” *Inorg. Chem. Front.*, vol. 1, no. 8, pp. 577–598, 2014, doi: 10.1039/c4qi00059e.

[29] A. Dewandre, M. J. Verstraete, N. Grobert, and Z. Zanolli, “Spectroscopic properties

of few-layer tin chalcogenides," *JPhys Mater.*, vol. 2, no. 4, 2019, doi: 10.1088/2515-7639/ab3513.

[30] X. Li and D. Gu, *Tin chalcogenides and nanocomposites*. Elsevier Inc., 2020. doi: 10.1016/b978-0-12-815924-8.00010-4.

[31] T. Jiang and G. A. Ozin, "New directions in SnS materials chemistry," *J. Mater. Chem.*, vol. 8, no. 5, pp. 1099–1108, 1998.

[32] K. J. Norton, F. Alam, and D. J. Lewis, "A Review of the Synthesis, Properties, and Applications of Bulk and Two-Dimensional Tin (II) Sulfide (SnS)," *Appl. Sci.*, vol. 11, no. 5, p. 2062, 2021, doi: 10.3390/app11052062.

[33] M. Leach, K. T. R. Reddy, M. V. Reddy, J. K. Tan, D. Y. Jang, and R. W. Miles, "Tin sulphide thin films synthesised using a two step process," *Energy Procedia*, vol. 15, no. 2011, pp. 371–378, 2012, doi: 10.1016/j.egypro.2012.02.045.

[34] U. Chalapathi, B. Poornaprakash, W. J. Choi, and S. H. Park, "Ammonia(aq)-enhanced growth of cubic SnS thin films by chemical bath deposition for solar cell applications," *Appl. Phys. A Mater. Sci. Process.*, vol. 126, no. 8, pp. 1–9, 2020, doi: 10.1007/s00339-020-03763-4.

[35] A. Boubakri, A. Jouidri, Y. Koumya, A. Rajira, A. Almaggoussi, and A. Abounadi, "An output characteristics simulation of SnS based solar cells," *Mater. Today Proc.*, vol. 51, no. August, pp. 2047–2052, 2021, doi: 10.1016/j.matpr.2021.07.428.

[36] D. Avellaneda, M. T. S. Nair, and P. K. Nair, "Photovoltaic structures using chemically deposited tin sulfide thin films," *Thin Solid Films*, vol. 517, no. 7, pp. 2500–2502, 2009, doi: 10.1016/j.tsf.2008.11.043.

[37] M. Sharon and K. Basavaswaran, "Photoelectrochemical behaviour of tin monosulphide," *Sol. Cells*, vol. 25, no. 2, pp. 97–107, 1988, doi: 10.1016/0379-6787(88)90015-4.

[38] I. Suzuki *et al.*, "N -type electrical conduction in SnS thin films," *Phys. Rev. Mater.*, vol. 5, no. 12, 2021, doi: 10.1103/PhysRevMaterials.5.125405.

References

[39] P. Sinsermsuksakul *et al.*, "Overcoming Efficiency Limitations of SnS-Based Solar Cells," *Adv. Energy Mater.*, vol. 4, no. 15, pp. 1–7, 2014, doi: 10.1002/aenm.201400496.

[40] E. Guneri, F. Gode, C. Ulutas, F. Kirmizigul, G. Altindemir, and C. Gumus, "Properties of p-type sns thin films prepared by chemical bath deposition," *Chalcogenide Lett.*, vol. 7, no. 12, pp. 685–694, 2010.

[41] N. Revathi *et al.*, "Annealing effect for SnS thin films prepared by high-vacuum evaporation," *J. Vac. Sci. Technol. A Vacuum, Surfaces, Film.*, vol. 32, no. 6, p. 061506, 2014, doi: 10.1116/1.4896334.

[42] R. Ghosh, K. K. Ghosh, and R. Chakraborty, "Narrow band filter using 1D periodic structure with defects for DWDM systems," *Opt. Commun.*, vol. 289, pp. 75–80, 2013, doi: 10.1016/j.optcom.2012.10.001.

[43] P. Jain and P. Arun, "In fl uence of grain size on the band-gap of annealed SnS thin fi lms 373 K," *Thin Solid Films*, vol. 548, pp. 241–246, 2013, doi: 10.1016/j.tsf.2013.09.089.

[44] K. Hartman *et al.*, "SnS thin-films by RF sputtering at room temperature," *Thin Solid Films*, vol. 519, no. 21, pp. 7421–7424, 2011, doi: 10.1016/j.tsf.2010.12.186.

[45] V. K. Arepalli, Y. Shin, and J. Kim, "Influence of working pressure on the structural, optical, and electrical properties of RF-sputtered SnS thin films," *Superlattices Microstruct.*, vol. 122, pp. 253–261, 2018, doi: 10.1016/j.spmi.2018.08.001.

[46] S. A. Bashkirov, V. F. Gremenok, V. A. Ivanov, V. V. Lazenka, and K. Bente, "Tin sulfide thin films and Mo/p-SnS/n-CdS/ZnO heterojunctions for photovoltaic applications," *Thin Solid Films*, vol. 520, no. 17, pp. 5807–5810, 2012, doi: 10.1016/j.tsf.2012.04.030.

[47] I. Y. Ahmet, M. S. Hill, A. L. Johnson, and L. M. Peter, "Polymorph-Selective Deposition of High Purity SnS Thin Films from a Single Source Precursor," *Chem. Mater.*, vol. 27, no. 22, pp. 7680–7688, 2015, doi: 10.1021/acs.chemmater.5b03220.

References

[48] M. Ganchev, P. Vitanov, M. Sendova-Vassileva, G. Popkirov, and H. Dikov, "Properties of SnS thin films grown by physical vapour deposition," *J. Phys. Conf. Ser.*, vol. 682, no. 1, 2016, doi: 10.1088/1742-6596/682/1/012019.

[49] R. Mariappan, T. Mahalingam, and V. Ponnuswamy, "Preparation and characterization of electrodeposited SnS thin films," *Optik (Stuttg).*, vol. 122, no. 24, pp. 2216–2219, 2011, doi: 10.1016/j.ijleo.2011.01.015.

[50] J. Johny, S. Sepulveda-Guzman, B. Krishnan, D. A. Avellaneda, J. A. Aguilar Martinez, and S. Shaji, "Synthesis and Properties of Tin Sulfide Thin Films from Nanocolloids Prepared by Pulsed Laser Ablation in Liquid," *ChemPhysChem*, vol. 18, no. 9, pp. 1061–1068, 2017, doi: 10.1002/cphc.201601186.

[51] V. R. Minnam Reddy, S. Gedi, C. Park, M. R.w, and R. R. Ramakrishna, "Development of sulphurized SnS thin film solar cells," *Curr. Appl. Phys.*, vol. 15, no. 5, pp. 588–598, 2015, doi: 10.1016/j.cap.2015.01.022.

[52] A. S. Hassanien and A. A. Akl, "Crystal imperfections and Mott parameters of sprayed nanostructure IrO2 thin films," *Phys. B Condens. Matter*, vol. 473, pp. 11–19, Jun. 2015, doi: 10.1016/j.physb.2015.05.023.

[53] K. Santhosh Kumar, C. Manoharan, S. Dhanapandian, and A. Gowri Manohari, "Effect of Sb dopant on the structural, optical and electrical properties of SnS thin films by spray pyrolysis technique," *Spectrochim. Acta - Part A Mol. Biomol. Spectrosc.*, vol. 115, pp. 840–844, 2013, doi: 10.1016/j.saa.2013.06.112.

[54] B. Ghosh, M. Das, P. Banerjee, and S. Das, "Fabrication and optical properties of SnS thin films by SILAR method," *Appl. Surf. Sci.*, vol. 254, no. 20, pp. 6436–6440, 2008, doi: 10.1016/j.apsusc.2008.04.008.

[55] D. J. Desale *et al.*, "Effect of annealing on structural and optoelectronic properties of CdS thin film by SILAR method," *Adv. Appl. Sci. Res.*, vol. 2, no. 4, pp. 417–425, 2011.

[56] M. Maghouli and H. Eshghi, "Effect of deposition time on physical properties of nanostructured CdS thin films grown by chemical bath deposition technique,"

Superlattices Microstruct., vol. 128, pp. 327–333, 2019, doi: 10.1016/j.spmi.2019.02.006.

[57] A. Higareda-Sánchez, R. Mis-Fernández, I. Rimmaudo, E. Camacho-Espinosa, and J. L. Peña, "Evaluation of pH and deposition mechanisms effect on tin sulfide thin films deposited by chemical bath deposition," *Superlattices Microstruct.*, vol. 151, no. August 2020, 2021, doi: 10.1016/j.spmi.2021.106831.

[58] "Generations of solar cell First Generation Solar Cells," pp. 1–10, 1954.

[59] J. Jing *et al.*, "Chemical bath deposition of SnS nanosheet thin films for FTO/SnS/CdS/Pt photocathode," *J. Alloys Compd.*, vol. 726, pp. 720–728, 2017, doi: 10.1016/j.jallcom.2017.07.303.

[60] J. Y. Cho *et al.*, "Achieving over 4% efficiency for SnS/CdS thin-film solar cells by improving the heterojunction interface quality," *J. Mater. Chem. A*, vol. 8, no. 39, pp. 20658–20665, 2020, doi: 10.1039/d0ta06937j.

[61] P. K. Nair, A. R. Garcia-Angelmo, and M. T. S. Nair, "Cubic and orthorhombic SnS thin-film absorbers for tin sulfide solar cells," *Phys. Status Solidi Appl. Mater. Sci.*, vol. 213, no. 1, pp. 170–177, 2016, doi: 10.1002/pssa.201532426.

[62] H. Noguchi, A. Setiyadi, H. Tanamura, T. Nagatomo, and O. Omoto, "Characterization of vacuum-evaporated tin sulfide film for solar cell materials," *Sol. Energy Mater. Sol. Cells*, vol. 35, no. C, pp. 325–331, 1994, doi: 10.1016/0927-0248(94)90158-9.

[63] S. P. Sreenilayam *et al.*, "Photonic crystals-based light-trapping approach in solar cells," *Nano-Optics*, pp. 337–345, 2020, doi: 10.1016/b978-0-12-818392-2.00014-7.

[64] P. C. Back-reflectors *et al.*, "Silicon Photovoltaics Using Conducting," pp. 1577–1582, 2008, doi: 10.1002/adma.200702219.

[65] H. Tan, R. Santbergen, A. H. M. Smets, and M. Zeman, "Plasmonic Light Trapping in Thin- fi lm Silicon Solar Cells with Improved Self-Assembled Silver Nanoparticles," 2012.

References

[66] X. Niquille, C. Ballif, and T. So, “TCOs for Nip Thin Film Silicon Solar Cells,” no. November 2008, pp. 165–176, 2009, doi: 10.1002/pip.

[67] B. Yan, G. Yue, L. Sivec, J. Owens-mawson, J. Yang, and S. Guha, “Solar Energy Materials & Solar Cells Correlation of texture of Ag / ZnO back reflector and photocurrent in hydrogenated nanocrystalline silicon solar cells,” *Sol. Energy Mater. Sol. Cells*, vol. 104, pp. 13–17, 2012, doi: 10.1016/j.solmat.2012.04.036.

[68] M. Zeman, O. Isabella, F. Moll, and J. Krc, “pss,” vol. 646, no. 3, pp. 642–646, 2010, doi: 10.1002/pssa.200982828.

[69] H. Tan *et al.*, “Highly transparent modulated surface textured front electrodes for high-ef fi ciency multijunction thin- fi lm silicon solar cells,” no. June, pp. 949–963, 2015, doi: 10.1002/pip.

[70] K. X. Wang, Z. Yu, V. Liu, A. Raman, Y. Cui, and S. Fan, “Light trapping in photonic crystals,” *Energy Environ. Sci.*, vol. 7, no. 8, pp. 2725–2738, 2014, doi: 10.1039/c4ee00839a.

[71] “Joannopoulos_nature_386_143_97.pdf.”

[72] M. Johri, Y. A. Ahmed, and T. Bezboruah, “Photonic band gap materials: Technology, applications and challenges,” *Curr. Sci.*, vol. 92, no. 10, pp. 1361–1365, 2007.

[73] E. Yablonovitch, “Photonic band-gap structures,” *J. Opt. Soc. Am. B*, vol. 10, no. 2, p. 283, 1993, doi: 10.1364/josab.10.000283.

[74] J. Stodolka, “Fabrication of two-dimensional hybrid photonic crystals utilizing electron beam lithography,” vol. 79, pp. 442–447, 2005, doi: 10.1016/j.mee.2004.12.056.

[75] S. H. Kim, K. D. Lee, J. Y. Kim, M. K. Kwon, and S. J. Park, “Fabrication of photonic crystal structures on light emitting diodes by nanoimprint lithography,” *Nanotechnology*, vol. 18, no. 5, 2007, doi: 10.1088/0957-4484/18/5/055306.

[76] F. Beyer and B. Daszuta, “Numerical evolutions of fields on the 2-sphere using a

spectral method based on spin-weighted spherical harmonics," vol. 075019, doi: 10.1088/0264-9381/31/7/075019.

[77] B. H. Míguez *et al.*, "Photonic Bandgap Engineering in Germanium," no. 21, pp. 1634–1637, 2001.

[78] M. Campbell, D. N. Sharp, M. T. Harrison, and R. G. Denning, "Fabrication of photonic crystals for the visible spectrum by holographic lithography," vol. 404, no. March, pp. 53–56, 2000.

[79] M. Duneau, F. Delyon, and M. Audier, "Holographic method for a direct growth of three-dimensional photonic crystals by chemical vapor deposition," *J. Appl. Phys.*, vol. 96, no. 5, pp. 2428–2436, 2004, doi: 10.1063/1.1776322.

[80] H. A. Youssef, H. A. El-Hofy, and M. H. Ahmed, *Engineering Materials and Their Applications*. 2020. doi: 10.1201/b11792-8.

[81] T. Section, D. Technology, M. F. Processes, and T. F. Deposition, "Thin film deposition technology," *Microelectron. Reliab.*, vol. 10, no. 2, p. 130, 1971, doi: 10.1016/0026-2714(71)90565-8.

[82] A. A. Aboud, A. Mukherjee, N. Revaprasadu, and A. N. Mohamed, "The effect of Cu-doping on CdS thin films deposited by the spray pyrolysis technique," *J. Mater. Res. Technol.*, vol. 8, no. 2, pp. 2021–2030, 2019, doi: 10.1016/j.jmrt.2018.10.017.

[83] D. D. O. Eya, "Chemical bath deposition and characterization of Cu2O-Cu xS thin films," *Turkish J. Phys.*, vol. 34, no. 1, pp. 51–57, 2010, doi: 10.3906/fiz-0905-18.

[84] P. K. Nair *et al.*, "Semiconductor thin films by chemical bath deposition for solar energy related applications," *Sol. Energy Mater. Sol. Cells*, vol. 52, no. 3–4, pp. 313–344, 1998, doi: 10.1016/S0927-0248(97)00237-7.

[85] D. Depla, S. Mahieu, and J. E. Greene, *Chapter 5 - Sputter Deposition Processes*, Third Edit. Elsevier Ltd., 2010. doi: 10.1016/B978-0-8155-2031-3.00005-3.

[86] T. V Tsankov, "Plasma parameters and tungsten sputter rates in a high-frequency CCP Plasma parameters and tungsten sputter rates in a high-frequency CCP," vol. 043511,

no. March, 2022, doi: 10.1063/5.0083613.

[87] S. Swann, “Magnetron sputtering,” *Phys. Technol.*, vol. 19, no. 2, pp. 67–75, 1988, doi: 10.1088/0305-4624/19/2/304.

[88] D. Depla, S. Mahieu, and J. E. Greene, “Sputter deposition processes,” J. Vac. Sci. Technol. A: Vac. Surf. Films, vol. 281, pp. 1–36, 2017 doi:10.1116/1.4998940

[89] J. F. Smith and D. C. Hinson, “Thin Film Characterization.,” *Solid State Technol.*, vol. 29, no. 11, pp. 135–140, 1986, doi: 10.1007/978-3-658-35926-3_5.

[90] A. A. Bunaciu, E. gabriela Udriştioiu, and H. Y. Aboul-Enein, “X-Ray Diffraction: Instrumentation and Applications,” *Crit. Rev. Anal. Chem.*, vol. 45, no. 4, pp. 289–299, 2015, doi: 10.1080/10408347.2014.949616.

[91] G. Singh, B. Umbrah, R. M. Sharma, "Raman spectroscopy – Basic principle, instrumentation and selected applications for the characterization of drugs of abuse,"*Egyptian Journal of Forensic Sciences*, vol. 6, no. 3, pp. 209-215, 2016. doi: 10.1016/j.ejfs.2015.06.001.

[92] S. Nand, “Raman Spectroscopy),” vol. 14, no. September, pp. 3–4, 1988, doi: 10.13140/RG.2.2.24191.33445.

[93] T. Jawhari, “Raman spectroscopy as a powerful analytical tool: probing the structure of matter,” 2012, [Online]. Available: http://diposit.ub.edu/dspace/handle/2445/32135

[94] K. Eberhardt, C. Stiebing, C. Matthaüs, M. Schmitt, and J. Popp, “Advantages and limitations of Raman spectroscopy for molecular diagnostics: An update,” *Expert Rev. Mol. Diagn.*, vol. 15, no. 6, pp. 773–787, 2015, doi: 10.1586/14737159.2015.1036744.

[95] A. Mayeen, L. K. Shaji, A. K. Nair, and N. Kalarikkal, *Morphological characterization of nanomaterials*. Elsevier Ltd., 2018. doi: 10.1016/B978-0-08-101973-3.00012-2.

[96] R. S. Prabhu, R. Priyanka, M. Vijay, and G. R. K. Vikashini, “Field Emission

Scanning Electron Microscopy (Fesem) with A Very Big Future in Pharmaceutical Research," vol. 11, pp. 183–187, 2021.

[97] C. R. Che Hak *et al.*, "Field Emission Scanning Electron Microscope (FE-SEM) Facility in BTI," *Nucl. Tech. Conv.*, p. 6, 2015, [Online]. Available: http://www.iaea.org/inis/collection/NCLCollectionStore/_Public/47/111/47111897.pdf

[98] Gossman Forensics, "How Does Scanning Electron Microscope / Energy Dispersive X-ray (SEM / EDX) Work ?," *Gossman Forensics*, p. 1, 2012, [Online]. Available: https://www.gossmanforensics.com/pdf-library/pdf-analytical-methods/sem-edx.pdf

[99] H. S. Min, "Chapter 2 Thin Film Studies by Energy Dispersive X-Ray Analysis Technique : Review Thin Film Studies by Energy Dispersive X-Ray Analysis Technique : Review," no. December, 2022, doi: 10.9734/bpi/nfpsr/v5/4425E.

[100] "Energy Dispersive X-ray (EDX) microanalysis: A powerful tool in biomedical research and diagnosis," Eur J Histochem vol. 62, no:1, pp. 28412018. doi: 10.4081/ejh.2018.2841

[101] C. Analysis and M. Characterization, *6.1.1 Introduction 6*. 2020. doi: 10.1016/B978-0-12-814866-2.00006-3.

[102] F. Padera, "Measuring Absorptance (k) and Refractive Index (n) of Thin Films" PerkinElmer, Inc. Shelton, CT USA.

[103] P. R. Jubu, O. S. Obaseki, A. Nathan-Abutu, F. K. Yam, Y. Yusof, and M. B. Ochang, "Dispensability of the conventional Tauc's plot for accurate bandgap determination from UV–vis optical diffuse reflectance data," *Results Opt.*, vol. 9, no. July, p. 100273, 2022, doi: 10.1016/j.rio.2022.100273.

[104] K. Instruments, "Series 2400 SourceMeter ® User ' s Manual User ' s Manual," no. September, 2011.

[105] M. S. Su, C. Y. Kuo, M. C. Yuan, U. S. Jeng, C. J. Su, and K. H. Wei, "Improving device efficiency of polymer/fullerene bulk heterojunction solar cells through

enhanced crystallinity and reduced grain boundaries induced by solvent additives," *Adv. Mater.*, vol. 23, no. 29, pp. 3315–3319, 2011, doi: 10.1002/adma.201101274.

[106] N. Kabiri Samani, Z. Dehghani Tafti, H. A. Bioki, M. B. Zarandi, and S. Shayegh, "Annealing effect on structural and optical constants of SnS thin films for solar cells application," *Optik (Stuttg).*, vol. 131, pp. 231–241, 2017, doi: 10.1016/j.ijleo.2016.08.129.

[107] S. Mishra, A. Ingale, U. N. Roy, and A. Gupta, "Study of annealing-induced changes in CdS thin films using X-ray diffraction and Raman spectroscopy," vol. 516, pp. 91–98, 2007, doi: 10.1016/j.tsf.2007.04.160.

[108] U. Chalapathi, B. Poornaprakash, and S. H. Park, "Chemically deposited cubic SnS thin films for solar cell applications," *Sol. Energy*, vol. 139, pp. 238–248, 2016, doi: 10.1016/j.solener.2016.09.046.

[109] S. B. Patil and A. K. Singh, "Effect of complexing agent on the photoelectrochemical properties of bath deposited CdS thin films," *Appl. Surf. Sci.*, vol. 256, no. 9, pp. 2884–2889, Feb. 2010, doi: 10.1016/j.apsusc.2009.11.043.

[110] J. Y. Cho, S. Sinha, M. G. Gang, and J. Heo, "Controlled thickness of a chemical-bath-deposited CdS buffer layer for a SnS thin film solar cell with more than 3% efficiency," *J. Alloys Compd.*, vol. 796, pp. 160–166, 2019, doi: 10.1016/j.jallcom.2019.05.035.

[111] B. Altiokka and A. K. Yildirim, "Electrodeposition of CdS Thin Films at Various pH Values," *J. Korean Phys. Soc.*, vol. 72, no. 6, pp. 687–691, 2018, doi: 10.3938/jkps.72.687.

[112] V. S. Raut, C. D. Lokhande, and V. V Killedar, "Studies on effect of pH on structural, optical and morphological properties of chemisynthesizedCdSe grains," *Int. J. Eng. Res. Technol.*, vol. 10, no. 1, pp. 568–572, 2017, [Online]. Available: http://www.irphouse.com

[113] T. Ben Nasr, N. Kamoun, M. Kanzari, and R. Bennaceur, "Effect of pH on the properties of ZnS thin films grown by chemical bath deposition," *Thin Solid Films*,

vol. 500, no. 1–2, pp. 4–8, 2006, doi: 10.1016/j.tsf.2005.11.030.

[114] S. K. Mishra, H. Roy, A. K. Lohar, S. K. Samanta, S. Tiwari, and K. Dutta, "A comparative assessment of crystallite size and lattice strain in differently cast A356 aluminium alloy," in *IOP Conference Series: Materials Science and Engineering*, 2015, vol. 75, no. 1. doi: 10.1088/1757-899X/75/1/012001.

[115] E. R. Shaaban, N. Afify, and A. El-Taher, "Effect of film thickness on microstructure parameters and optical constants of CdTe thin films," *J. Alloys Compd.*, vol. 482, no. 1–2, pp. 400–404, Aug. 2009, doi: 10.1016/j.jallcom.2009.04.033.

[116] J. S. Kanger and C. Otto, "Orientation effects in waveguide resonance Raman spectroscopy of monolayers," *Appl. Spectrosc.*, vol. 57, no. 12, pp. 1487–1493, 2003, doi: 10.1366/000370203322640125.

[117] V. I. Korepanov, S. Y. Chan, H. C. Hsu, and H. o. Hamaguchi, "Phonon confinement and size effect in Raman spectra of ZnO nanoparticles," *Heliyon*, vol. 5, no. 2, pp. 1–14, 2019, doi: 10.1016/j.heliyon.2019.e01222.

[118] M. Gilic *et al.*, "Optical properties of CdS thin films," *Opt. Mater. (Amst).*, vol. 35, no. 5, pp. 1112–1117, 2013, doi: 10.1016/j.optmat.2012.12.028.

[119] K. Ag. Eg. Fg. C, "Effect of pH on the physical properties of CdS thin films deposited by CBD EFFECT OF PH ON THE PHYSICAL PROPERTIES OF CdS THIN FILMS," *Chalcogenide Lett.*, vol. 9, no. June 2014, pp. 27–40, 2012.

[120] K. Zhong *et al.*, "Facile synthesis of CuO nanorods with abundant adsorbed oxygen concomitant with high surface oxidation states for CO oxidation," *RSC Adv.*, vol. 2, no. 30, pp. 11520–11528, 2012, doi: 10.1039/c2ra21149a.

[121] F. A. Akgul, G. Akgul, N. Yildirim, H. E. Unalan, and R. Turan, "Influence of thermal annealing on microstructural, morphological, optical properties and surface electronic structure of copper oxide thin films," *Mater. Chem. Phys.*, vol. 147, no. 3, pp. 987–995, 2014, doi: 10.1016/j.matchemphys.2014.06.047.

[122] M. Minbashi, A. Ghobadi, M. H. Ehsani, H. Rezagholipour Dizaji, and N. Memarian,

"Simulation of high efficiency SnS-based solar cells with SCAPS," *Sol. Energy*, vol. 176, no. October, pp. 520–525, 2018, doi: 10.1016/j.solener.2018.10.058.

[123] A. Kuddus, S. K. Mostaque, and J. Hossain, "Simulating the performance of a high-efficiency SnS-based dual-heterojunction thin film solar cell," *Opt. Mater. Express*, vol. 11, no. 11, p. 3812, 2021, doi: 10.1364/ome.439629.

[124] E. Mellikov, V. Mikli, N. Revathi, and O. Volobujeva, "Chemical Bath Deposition of SnS Thin Films from the Solutions with Different Concentrations of Tin and Sulphur Chemical bath deposition of SnS thin films from the solutions with different concentrations of tin and sulphur," *Advanced Materials Research* , vol. 1117, pp. 183-186, 2015. doi: 10.4028/www.scientific.net/AMR.1117.183

[125] F. Scotognella *et al.*, "Metal oxide one dimensional photonic crystals made by RF sputtering and spin coating," *Ceram. Int.*, vol. 41, no. 7, pp. 8655–8659, 2015, doi: 10.1016/j.ceramint.2015.03.077.

[126] T. Senn, J. Bischoff, N. Nüsse, M. Schoengen, and B. Löchel, "Fabrication of photonic crystals for applications in the visible range by Nanoimprint Lithography," *Photonics Nanostructures - Fundam. Appl.*, vol. 9, no. 3, pp. 248–254, 2011, doi: 10.1016/j.photonics.2011.04.007.

[127] P. Bermel, C. Luo, L. Zeng, L. C. Kimerling, and J. D. Joannopoulos, "Improving thin-film crystalline silicon solar cell efficiencies with photonic crystals," *Opt. Express*, vol. 15, no. 25, p. 16986, 2007, doi: 10.1364/oe.15.016986.

[128] H. S. Dutta, A. K. Goyal, V. Srivastava, and S. Pal, "Coupling light in photonic crystal waveguides: A review," *Photonics Nanostructures - Fundam. Appl.*, vol. 20, pp. 41–58, 2016, doi: 10.1016/j.photonics.2016.04.001.

[129] P. Bienstman and R. Baets, "Optical modelling of photonic crystals and VCSELs using eigenmode expansion and perfectly matched layers," *Opt. Quantum Electron.*, vol. 33, no. 4–5, pp. 327–341, 2001, doi: 10.1023/A:1010882531238.

[130] A. F. Oskooi, D. Roundy, M. Ibanescu, P. Bermel, J. D. Joannopoulos, and S. G. Johnson, "Meep: A flexible free-software package for electromagnetic simulations by

the FDTD method," *Comput. Phys. Commun.*, vol. 181, no. 3, pp. 687–702, 2010, doi: 10.1016/j.cpc.2009.11.008.

[131] F. Seydou and T. Seppänen, "Photonic Crystals: from Theory to Practice," *Msas.Maliwatch.Org*, p. 165, 2001, [Online]. Available: http://msas.maliwatch.org/msas2004/proceedings/msas2004_pp074-083.pdf

[132] R. D. M. John D Joannopoulos, Steven G Johnson, Joshua N Winn, "*Molding the flow of light"*, Princeton University Press, 2008.

[133] M Halla, "On the approximation of dispersive electromagnetic eigenvalue problems in two dimensions," *IMA Journal of Numerical Analysis*, vol. 43, no. 1, pp. 535–559, 2023. doi: 10.1093/imanum/drab100.

[134] N. A. Mortensen, "Photonic crystal fibres: Mapping Maxwell's equations onto a Schrödinger equation eigenvalue problem," *J. Eur. Opt. Soc.*, vol. 1, pp. 1–7, 2006, doi: 10.2971/jeos.2006.06009.

[135] S. G. Johnson and J. D. Joannopoulos, "Introduction to Photonic Crystals : Bloch ' s Theorem , Band Diagrams , and Gaps (But No Defects) Maxwell ' s Equations in Periodic Media," no. February, pp. 1–16, 2003.

[136] A. Taflove, A. Oskooi, and S.G. Johnson, "*Advances in FDTD Computational Electrodynamics: Photonics and Nanotechnology*," Artech: Norwood, MA, 2013

[137] A. L. E. C. M. H. Ammond, A. R. O. Skooi, M. O. C. Hen, Z. I. N. L. In, S. T. G. J. Ohnson, and S. T. E. R. Alph, "High-performance hybrid time / frequency-domain topology optimization for large-scale photonics inverse design," vol. 30, no. 3, pp. 4467–4491, 2022.

[138] A. Manuscript, "Efficient Light Management by Textured Nanoimprinted Layers for Perovskite Solar Cells," *ACS Photonics*, vol. 4, no. 5, pp. 1232–1239 2017, doi: 10.1021/acsphotonics.7b00138.

[139] G. Rosolen and A. Cola, "Fabrication of photonic crystal structures by electron beam lithography," *Conf. Optoelectron. Microelectron. Mater. Devices, Proceedings*,

COMMAD, pp. 66–69, 2006, doi: 10.1109/COMMAD.2006.4429881.

[140] M. Nishimoto, K. Ishizaki, K. Maekawa, Y. Liang, K. Kitamura, and S. Noda, "Fabrication of photonic crystal lasers by MBE air-hole retained growth," *Appl. Phys. Express*, vol. 7, no. 9, 2014, doi: 10.7567/APEX.7.092703.

[141] T. Kawashima, "Autocloning technology: Fabrication method for photonic crystals based on sputtering process," pp. 115–122, 2003, doi: 10.1063/1.1372721.

[142] X. Meng *et al.*, "Design and fabrication of photonic crystals in epitaxy-free silicon for ultrathin solar cells" *Asia Commu- nications and Photonics Conference and Exhibition*, pp. 831207-831207-7, 2022, doi: 10.1117/12.9043832012.

[143] M. H. Suhail, G. M. Rao, and S. Mohan, "Dc reactive magnetron sputtering of titanium-structural and optical characterization of TiO2 films," *J. Appl. Phys.*, vol. 71, no. 3, pp. 1421–1427, 1992, doi: 10.1063/1.351264.

[144] G. Holmén and H. Jacobsson, "The influence of oxygen on SiO2 sputtering," *J. Appl. Phys.*, vol. 68, no. 6, pp. 2962–2965, 1990, doi: 10.1063/1.346431.

[145] P. Pansila, N. Witit-Anun, and S. Chaiyakun, "Influence of sputtering power on structure and photocatalyst properties of DC magnetron sputtered TiO2 thin film," *Procedia Eng.*, vol. 32, pp. 862–867, 2012, doi: 10.1016/j.proeng.2012.02.024.

[146] K. Takamura, Y. Abe, and K. Sasaki, "Influence of oxygen flow ratio on the oxidation of Ti target and the formation process of TiO2 films by reactive sputtering," *Vacuum*, vol. 74, no. 3-4 SPEC. ISS., pp. 397–401, 2004, doi: 10.1016/j.vacuum.2004.01.006.

[147] H. S. Bolarinwa *et al.*, "Determination of optical parameters of zinc oxide nanofibre deposited by electrospinning technique," *J. Taibah Univ. Sci.*, vol. 11, no. 6, pp. 1245–1258, 2017, doi: 10.1016/j.jtusci.2017.01.004.

[148] M. H. Kabir, M. M. Ali, M. A. Kaiyum, and M. S. Rahman, "Effect of annealing temperature on structural morphological and optical properties of spray pyrolized Al-doped ZnO thin films," *J. Phys. Commun.*, vol. 3, no. 10, Oct. 2019, doi: 10.1088/2399-6528/ab496f.

References

[149] A. M. Alsaad, Q. M. Al-Bataineh, A. A. Ahmad, Z. Albataineh, and A. Telfah, "Optical band gap and refractive index dispersion parameters of boron-doped ZnO thin films: A novel derived mathematical model from the experimental transmission spectra," *Optik (Stuttg).*, vol. 211, no. March, p. 164641, 2020, doi: 10.1016/j.ijleo.2020.164641.

[150] K. S. Kim, H. W. Kim, and N. H. Kim, "Structural characterization of ZnO films grown on SiO2 by the RF magnetron sputtering," *Phys. B Condens. Matter*, vol. 334, no. 3–4, pp. 343–346, 2003, doi: 10.1016/S0921-4526(03)00096-6.

[151] Q. H. Fan, L. Q. Zhou, and D. Stevenson, "High rate sputtering deposition of silicon oxide thin films from new SiO2:Si target composition," *J. Vac. Sci. Technol. A Vacuum, Surfaces, Film.*, vol. 27, no. 4, pp. 979–985, 2009, doi: 10.1116/1.3071962.

[152] H. Sedrati, M. C. Benachour, H. Dehdouh, and R. Bensaha, "Tuning of the stop-band position in the visible range of SiO2/TiO2 Bragg reflectors by doping TiO2 with transition metals," *Optik (Stuttg).*, vol. 208, no. November 2019, 2020, doi: 10.1016/j.ijleo.2019.164098.

[153] S. H. Jeong, J. K. Kim, B. S. Kim, S. H. Shim, and B. T. Lee, "Characterization of SiO2 and TiO2 films prepared using rf magnetron sputtering and their application to anti-reflection coating," *Vacuum*, vol. 76, no. 4, pp. 507–515, 2004, doi: 10.1016/j.vacuum.2004.06.003.

[154] A. Macleod, "The Quarterwave Stack: 2. Properties," *SVC Fall Bull.*, vol. 16, no. 3, pp. 16–21, 2012, [Online]. Available: https://www.svc.org/Publications/SVC-Bulletin-Contributed-Articles.cfm